Graduate School Form 9
(Revised 7/94)

PURDUE UNIVERSITY
GRADUATE SCHOOL
Thesis Acceptance

This is to certify that the thesis prepared

By Zheng-Min Wang

Entitled

Complete Determination of Atomic Parameters in Two-Photon Ionization and Study of Quantum Interference with Two-Color Laser Fields

Complies with University regulations and meets the standards of the Graduate School for originality and quality

For the degree of Doctor of Philosophy

Signed by the final examining committee:

CO-, chair

Daniel S. Elliott CO-CHAIR

Albert Overhauser

Approved by: Andrew F. Hebard 10/1/01
Department Head Date

This thesis ☐ is ☒ is not to be regarded as confidential. Daniel S. Elliott
Major Professor

Format Approved by:

Chair, Final Examining Committee or Stephen M. Durbin
Thesis Format Adviser

COMPLETE DETERMINATION OF ATOMIC PARAMETERS IN TWO-PHOTON IONIZATION AND STUDY OF QUANTUM INTERFERENCE WITH TWO-COLOR LASER FIELDS

A Thesis

Submitted to the Faculty

of

Purdue University

by

Zheng-Min Wang

In Partial Fulfillment of the

Requirements for the Degree

of

Doctor of Philosophy

December 2001

ProQuest Information and Learning Company
300 North Zeeb Road
P.O. Box 1346
Ann Arbor, MI 48106-1346

This Thesis Is Dedicated
in Memory of My Parents

ACKNOWLEDGEMENTS

I am enormously grateful to my thesis adviser Professor Daniel S. Elliott for his valuable guidance and advice, with which I reached the threshold of receiving my Ph.D. degree. More importantly, I have learned from him how to work at the frontier of science. I would also like to express my deepest gratitude to the chair of my Ph.D. Advisory Committee, Professor David D. Nolte, and the other members, Professors Albert W. Overhauser, Ephraim Fischbach and James G. Mullen (retired) for their very helpful advice, constructive suggestions and the time to serve on my Committee.

I greatly acknowledge the contributions of Michael Crogan and Tim Jackson, who wrote the computer program necessary for data acquisition, helpful discussions with W. Hill and Jie Zhu concerning the construction of the detector and James Colgan concerning relative cross sections for photo-ionization of rubidium.

Many more people gave me help, discussions on various aspects, or made my time at Purdue pleasant: Binh Do, Yi-Yian Yin, Ce Chen, Michael Rifani, Tim Miller, Christopher Tong, Art Mills, Mehmetcan Akbulut, Mevan K. Gunawardena, Rekishu Yamazaki, Dave Azpel, Chuck Harrington and Chuck Barnett.

Finally, I am indebted to my wife and my son for their understanding, encouragement and support.

This material is based upon work supported by the National Science Foundation under Grant No. 9732611-PHY.

TABLE OF CONTENTS

Page

Page

LIST OF FIGURES

Figure **Page**

Figure **Page**

Figure **Page**

ABSTRACT

Wang, Zheng-Min, Ph.D., Purdue University, December, 2001. Complete Determination of Atomic Parameters in Two-Photon Ionization and Study of Quantum Interference with Two-Color Laser Fields. Major Professors: Daniel S. Elliott and David D. Nolte.

We present our study on complete measurements of two-photon ionization in atomic rubidium. In this study we developed an effective technique to measure the angular distributions of photoelectrons. Through the measurements with this technique and using elliptically-polarized light we have successfully determined the atomic parameters---the relative cross sections for various ionization channels as well as the phase difference between *s*- and *d*-continuum waves. The measured phase differences are in excellent agreement with expected values over the entire range of photoelectron kinetic energy from 0 to 0.5 eV. The measured relative cross sections for ionization into *S* and *D* channels are also in good agreement with theoretical data. Both the relative cross sections and phase differences show a slow variation as a function of photoelectron energy. The ratios of cross sections of the two *D* channels are not in agreement with the expected value, suggesting fine structure effects.

We also studied a quantum mechanical interference using two-color laser fields and observed the extremely asymmetric photoelectron angular distribution produced by interfering even- and odd-order photoionization processes in atomic

rubidium as the optical phase was varied. We observed these effects with both perpendicularly and parallel-polarized fields components. It is worthy to note that the quantum interference observed with perpendicularly-polarized two-color fields is unique. Based on the analysis of measured angular distributions we derived the phase difference between even and odd continuum waves for the first time. The measured value of the phase difference is in good agreement with the calculated value from quantum defect theory.

CHAPTER 1
INTRODUCTION

The angular distributions of photo-ejected electrons provide valuable information about the structure of atoms and molecules. Measurement of photoelectron angular distributions (PAD) is a powerful tool for the exploration of atomic and molecular structure as well as for studying the fundamental properties of the interaction of light with matter. The photoelectron angular distributions depend upon the nature of the initial bound state and final continuum states. By studying photoelectron angular distributions, one can further understand the nature and features of the atomic electronic structure and dynamics. The phase difference of the partial waves in the continuum can be extracted from measurements of the differential photo-ionization cross section, that is, the angular distribution. This information is not available from the measurement of the total photo-ionization cross section.

The conventional technique for the measurement of PAD uses a single channel electron detector to detect the photoelectron flux in several directions in a plane perpendicular to a laser beam with linearly-polarized light. Unfortunately, the atomic parameters cannot be uniquely determined from these measurements of PAD. We developed a more effective technique for the measurements of PAD and the determination of atomic parameters. In this technique, the photoelectrons emitted in the interaction region are collected in all directions by a specially designed photoelectron detector and form a two-dimensional image on a phosphor

screen of the detector. And equally important, instead of using linearly-polarized light we use elliptically-polarized light for the experiments.

With this technique, we record the two-dimensional images of PAD for the two-photon ionization process in atomic rubidium and determine the three atomic parameters simultaneously without additional measurements or data from theory. These atomic parameters include the relative photo-ionization cross section between the *S* and *D* channels σ_s/σ_d, the relative cross section between the two fine structure *D* channels $\sigma_{5/2}/\sigma_{3/2}$ and the phase difference between *s*- and *d*-continuum waves $\Delta\xi=\xi_s-\xi_d$.

An attractive extension of this field is the use of a two-color laser field for investigating the interference between odd- and even-order (i.e. the number of photons involved) processes. Two different channels are involved in the transition between the same initial and final continuum states. In this case the photoelectron angular distributions are asymmetric and can be changed by varying the relative phase between the two fields. This is one of the aspects in the studies of coherent control. In these studies, we photo-ionize atomic rubidium from its ground state by using visible light at 560 nm and its double frequency UV light at 280 nm, simultaneously. The one photo-ionization process of the rubidium atom with the UV light leads to a *p*-wave with odd parity, while the two-photon interaction with visible light leads to *s*- and *d*-waves, which are both of even parity. The continuum wave function excited by these two interactions is a linear combination of the odd- and even-wavefunctions. This allows us to control the direction in which the photoelectrons are ejected. We are able to change the angular distribution by varying the relative phase between the two laser fields. We have observed the asymmetric angular distributions of photoelectrons using our technique. For the first time we have determined the phase difference between the even and odd continuum waves (i.e. *p*- and *d*-waves) based on the images produced by the two-color coherent field.

CHAPTER 2
DESCRIPTION OF PHOTOELECTRON ANGULAR DISTRIBUTIONS

This chapter is primarily concerned with the basic concept of multi-photon ionization of atoms, the principle of the measurement of PAD, and the determination of the atomic parameters using the conventional technique with linearly-polarized light. We also present a summary of the theory of PAD in two-photon ionization with arbitrarily-polarized light, which is critical for the determination of atomic parameters on the two-photon ionization with elliptically-polarized light.

2.1 Historical overview

The first measurements of the photoelectron angular distribution can be dated to as early as 1924, performed by Bothe [1] when ionizing molecules, such as $CHCl_3$ and C_2H_5Br, with x rays. At such high energy the linear momentum of the photon is not negligible with respect to the momentum of the bound electron. This results in a distortion of the photoelectron angular distribution due to momentum transfer. Experiments on the angular distribution of photoelectrons ejected by polarized ultraviolet light in potassium vapor were performed in 1931 [2]. At these photon energies, the momentum transfer can be neglected. These experiments showed that the most probable direction of emission of electrons by polarized radiation was in the direction of the electric vector and that the angular distribution varies as the square of the cosine of the angle between the electric vector and the

direction of the ejected electron. This result is consistent with the prediction of quantum mechanics for a spherically symmetric atom.

Early work in the theory of the angular distribution of ejected particles was developed in connection with angular distributions in nuclear processes [3]. With the advent of lasers, interest turned to atomic photoionization processes. Zernik [4] was the first to calculate angular distributions for the special case of two-photon nonresonant ionization of the 2s metastable state in atomic hydrogen. Subsequently, Cooper and Zare calculated the photoelectron angular distribution for several negative ions [5], one-electron and many-electron atomic systems [6], as did Tully et al. [7] with emphasis on molecules. Numerous theoretical analyses of angular distributions of photoelectrons have been worked out for different aspects of this subject [8-15, 31, 36-37].

The experimental study of angular distributions from multi-photon ionization was pioneered by R.S. Berry and his colleagues [16]. In 1974, they measured the angular distribution of electrons from resonant two-photon ionization of titanium atoms. These experiments demonstrated the feasibility of the technique, but the complexities of the structure of titanium made interpretation of the results difficult. Berry's group turned to atomic sodium and obtained much more definitive results using a two-step ionization process [17]. Since then a series of experimental measurements of angular distributions have been presented for two- and three-photon ionization for sodium [18, 19], cesium [20] and strontium [21].

The influence of nuclear spin on angular distributions has been studied by a number of groups [18-19, 23-24]. For example, in 1979, Leuchs *et.al.* [24] performed an experiment on a quantum interference effect in photo-ionization. They observed the quantum beats due to the hyperfine structure state $3^2P_{3/2}$ of sodium in two-photon ionization. The atoms were ionized stepwise with two pulsed lasers. The photoelectron angular distribution, measured as function of the

delay between the two laser pulses, exhibited a periodic variation due to the quantum beat effect.

The angular distribution of photoelectrons is expected to depend only on the angular momentum quantum numbers and not on the principle quantum numbers. This is not the case, however, when atoms with more than one valence electron are studied, where double excited levels exist below the first ionization limit. That is, there exist perturbations of the intermediate levels by configuration mixing, which have been observed [25, 26]; Leuchs *et. al.* [25] studied these effects with resonant multiphoton ionization in barium. The results showed that state mixing dramatically influenced both the total ion yield and the angular distribution of photoelectrons.

The ac Stark effect also influences the angular distribution of photoelectrons. Ohnesorge *et. al.* [35] studied this effect using the two-photon-resonant, three–photon ionization of atomic sodium. Since the Stark effect is linear with intensity, the angular distribution changes with the laser intensity. The measured distribution with mean pulse intensities ranging from 0.6 MW/cm^2 to 530 MW/cm^2 were qualitatively consistent with the predictions of Dixit and Lambropoulos [36-37]. This work implies that the intensity effect has to be considered whenever atomic data are to be extracted from photoelectron angular distributions. A more quantitative theoretical investigation was carried out by Geltman and Leuchs [22]. The comparison of the theoretical results with the experimental data obtained by Ohnesorge *et. al.* clearly shows that the hyperfine splitting of the ground state has to be taken into account at high laser intensities.

Also the energy spectrum and angular distributions of electrons produced in above-threshold ionization (ATI) processes have been measured [27]. Above-threshold ionization (ATI) has opened a new line for measuring the physical characteristics of the outgoing electrons, especially its energy spectrum and its angular distribution. In "normal" multi-photon ionization, only the minimum

number of photons necessary to ionize the atom are involved. For multi-photon ATI, more photons with the same energy can be absorbed in the processes, i.e. continuum-continuum transitions take place in ATI. The first experimental demonstration of ATI was given by Agostini et al. [27]. In the experiment, the fundamental frequency (1.06 μm, $h\nu$=1.17eV) from a Nd:glass laser was passed through xenon gas (IP=12.27eV). They observed the ionization of xenon by absorption of eleven photons and continuum-continuum transitions by absorption of the twelfth photon. This process results mainly in an increase of the emitted electron kinetic energy by $h\nu$. They also showed that the discrete absorption of photons above six-photon ionization using the second harmonic (0.53 μm, $h\nu$=2.34eV) of the fundamental output of this laser. In this case, the six-photon ionization of xenon requires an intensity roughly 5 times lower. Since that time, much experimental and theoretical work on ATI has been reported [15,28-34].

It was pointed out by Lambropoulos [9] that the measurements of the photoelectron angular distributions in multiphoton ionization may yield information about the phase shifts of the continuum wave functions that can not be obtained from total cross section measurements. Information about scattering phases of outgoing electron waves is contained in the angular distribution parameters. Yin and Elliott [50] obtained the continuum-wave-function phase differences of the partial *s*-wave and *d*-wave over several laser wavelengths based on the angular distribution measurements of atomic rubidium in two-photon ionization. This experiment used linearly-polarized laser light to excite the atoms and measured the angular distributions of photoelectrons using a single channel electron detector in a plane perpendicular to the laser beam. The major disadvantage of this technique is that the three atomic parameters cannot be determined by these measurements alone. It must be augmented by results from other experiment or data from theory. The reliability and the accuracy of the results also depend on the other sources. In order to determine the atomic

parameters from the measurements of PAD independently, Elliott [53] developed a theory of PAD in two-photon ionization with arbitrarily-polarized light. We will give a summary of this theory in Sec. 2.5. By using this theory with elliptically-polarized light in two-photon ionization of rubidium, as well as using a special designed photoelectron detection technique we are able to determine the three atomic parameters without using the data from other sources.

2.2 Multi-photon ionization of atoms

Measurement of the angular distribution of photoelectrons is an important probe of the photo-ionization process of atoms. To understand the photoelectron angular distribution and what we can learn from it, it is essential to begin with the basic physics of photo-ionization of atoms. An atom with an ionization potential E_i can be ionized by absorption of one photon with an energy $h\nu > E_i$. It can, however, also occur by absorption of several photons, each of lower energy, as long as the sum of the photon energies is greater than the ionization potential E_i. This process is called multi-photon ionization. The ionization of short-lived intermediate states only yields measurable intensities if there are enough atoms in these states. Such multi-photon ionization processes may occur with excitation of intermediate resonance levels by absorption of the photons subsequently by the atom. This is called a resonant process. However, when the photon frequencies do not match the transition energies to any intermediate states the process can still take place, though with lower cross sections. This is called a non-resonant process. One of the most essential features of a multi-photon non-resonant absorption process is that it occurs through laser-induced virtual states, which are not eigenstates of the atom. The life time of the laser-induced virtual states is of the order of one optical cycle, typically $\sim 10^{-15}$ s. Consequently, the absorption of photons through the virtual states must occur within a time $< 10^{-15}$ s. Therefore, the photon flux has to be strong enough to have a large number of photons within

10^{-15} s. High-order photo-ionization processes may consist of one or more virtual transitions. For a resonant process, the life time of the intermediate states is typically 10^{-8} s, so this process can be performed with lower laser intensity. Thus we understand why nonresonant multi-photon ionization process can only be achieved with a high-intensity laser radiation.

Fig. 2.1 presents several possible excitation schemes of the multi-photon ionization process. Fig. 2.1a) shows a resonant three-photon process, with photon energies $E_1=h\nu_1$, $E_2=h\nu_2$, and $E_3=h\nu_3$. Each photon matches the energy difference between two energy states. Fig. 2.1b) shows a scheme with only one intermediate resonance using one laser source. Fig. 2.1c) shows a non-resonant three-photon ionization process with a single photon energy.

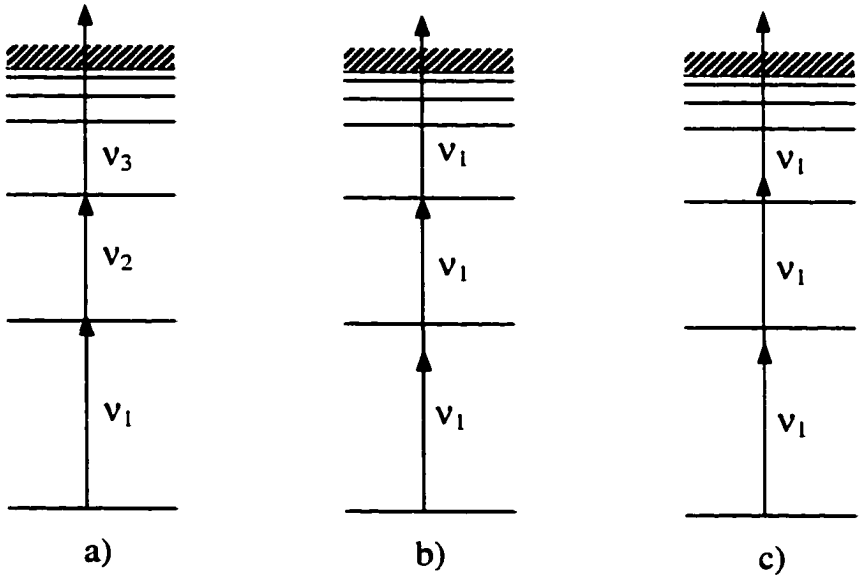

Figure 2.1: Schematic representation of multi-photon ionization:
a) Resonant (sequential) multi-photon ionization (several intermediate resonances, several lasers), b) Resonant multi-photon ionization (one intermediate resonance, one laser), c) Non-resonant multi-photon ionization. (S.J. Smith and G. Leuchs, 1987 [64])

2.3 Ionization channels of rubidium

We consider the non-resonant two-photon ionization of the rubidium atom from the initial ground state. See Fig. 2.2 for an energy level diagram of rubidium. In this case, the atom is ionized through absorption of two photons from the laser radiation. The ionization process is from the ground state $|5^2S_{1/2}\rangle$ via a laser-induced virtual P state to the continuum $|\varepsilon S\rangle$ and $|\varepsilon D\rangle$ states. The single photon energy lies roughly half way between the excitation energies of the $5p\ ^2P_J$ and the $6p\ ^2P_J$ intermediate states (J=1/2 or 3/2). In the most general case, such intermediate states are not eigenstates of the atom, but are virtual states, as mentioned earlier. The ground state is initially unaligned so that the two magnetic sublevels, $m_s=\pm 1/2$ (also $m_j=\pm 1/2$), are equally populated. Each continuum partial wave is taken as a superposition of an incoming spherical and outgoing plane wave, and can be expressed in products of the spherical harmonic functions $Y_{lm}(\Theta,\Phi)$ [6, 9]. According to the angular momentum selection rules for light that is linearly polarized along the z axis, $\Delta l=\pm 1$, $\Delta m_j=0$, and $\Delta j=0, \pm 1$ for each step of the ionization. The allowed ionization channels are shown in Fig. 2.3. $S_1 \sim S_5$ are the two-photon radial transition matrix elements that correspond to the five ionization channels from the ground state to the three continuum states. Obviously, the channels are the same for $m_j = -1/2$, and the associated spherical harmonics are similar except that Y_{21} is replaced by $Y_{2\,-1}$. For circularly-polarized light propagating along z, $\Delta l=\pm 1$, $\Delta m_j=\pm 1$ and $\Delta j=0, \pm 1$; in this case we have the ionization channels as shown in Fig. 2.4. The s-partial wave is not excited in the case of circularly-polarized light.

We can see that in the two-photon ionization process for linearly-polarized light, the final continuum state is a coherent combination of $|\varepsilon S\rangle$ and $|\varepsilon D\rangle$ states which involve Y_{00} for the former and Y_{20}, Y_{21} and Y_{2-1} for the latter; for circularly-

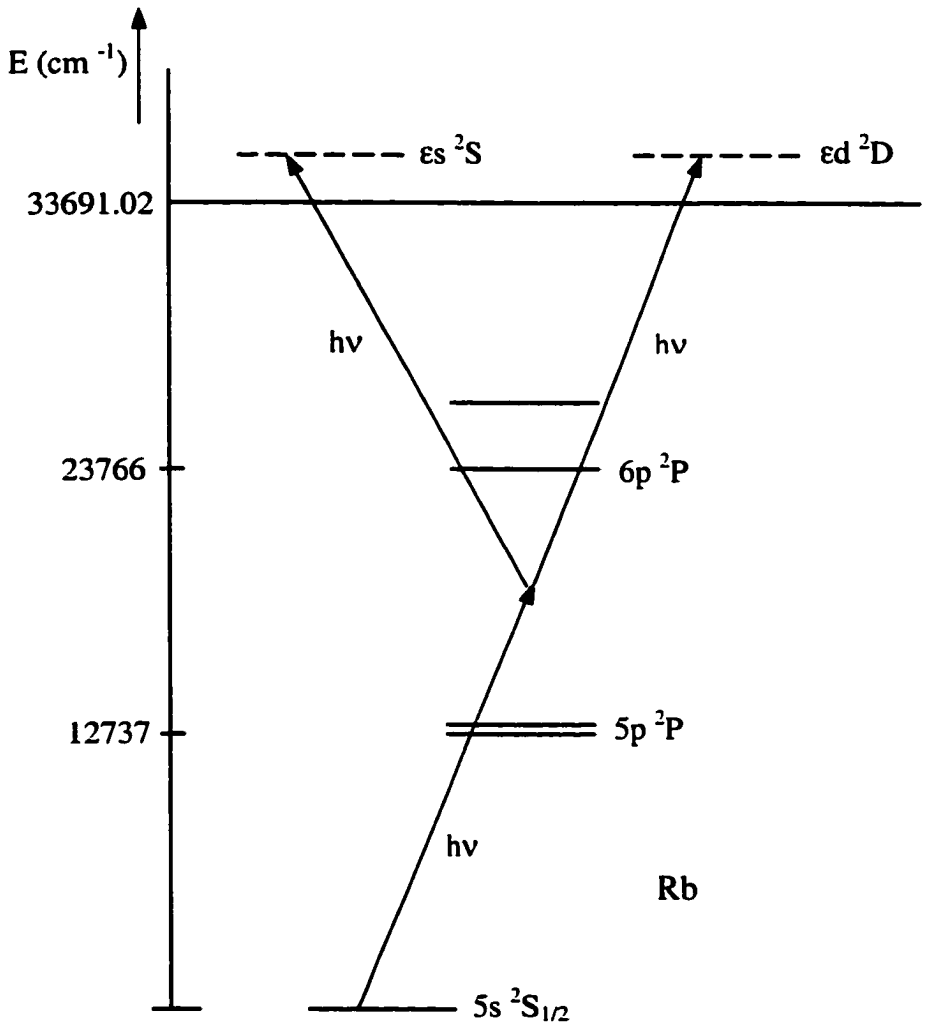

Figure 2.2: Energy level diagram of atomic rubidium.

polarized light, only the $|\varepsilon D\rangle$ state exists in the continuum whose transition amplitudes involve Y_{21}, Y_{2-1}, Y_{22} and Y_{2-2}. In the case of elliptically-polarized light, it is quite complicated to show the ionization channels. The final continuum state is a linear combination of all the six spherical harmonics Y_{00}, Y_{20}, Y_{21}, Y_{2-1}, Y_{22}, and Y_{2-2}. However, the use of the elliptically-polarized light makes the complete measurement of two-photon ionization possible. We will discuss the advantages of using elliptically-polarized light to measure the photoelectron angular distribution and to determine the atomic parameters later.

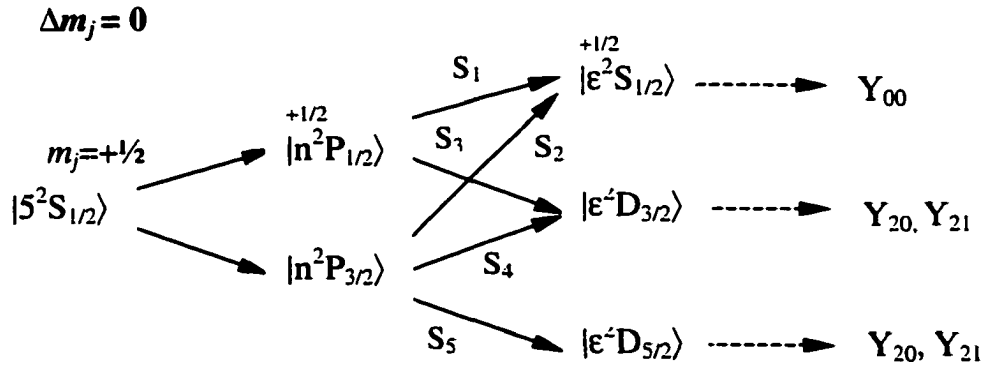

Figure 2.3: The ionization channels of two-photon ionization in rubidium by linearly-polarized light. S_1-S_5: two-photon radial matrix elements.

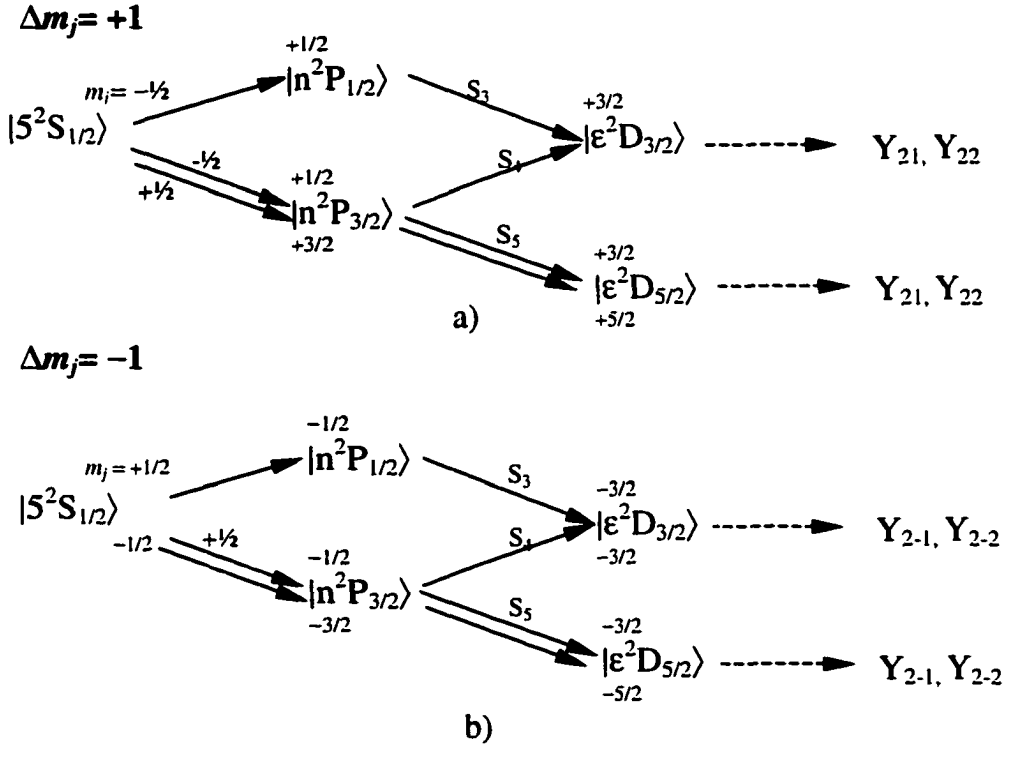

Figure 2.4: The ionization channels of two-photon ionization in rubidium by a) right circularly-polarized light
b) left circularly-polarized light
S_3~S_5 : two-photon radial matrix elements

2.4 The principle of PAD and determination of atomic parameters using linearly-polarized light

In multiphoton ionization, the final state contains more than one partial wave. Each partial wave is represented by a spherical harmonic $Y_{lm}(\vartheta,\varphi)$ since it corresponds to a state of definite orbital angular momentum. The angular distributions of photoelectrons in multi-photon ionization are determined by the initial state, intermediate states and the continuum final states involved in the process, the transition amplitude to the different partial waves of the free electron, the relative phase of the partial waves, and the nature of the radiation field, such as the wavelength and the polarization.

The differential photo-ionization cross section, which defines the angular distribution of photoelectrons, is obtained by evaluating the electric dipole matrix element for the transition from the initial bound state to the continuum. The wave function of the bound state is characterized by principal quantum number n, angular momentum quantum number l and magnetic quantum number m. In a potential with spherical symmetry, it can be written as

$$\psi_{nlm}(\mathbf{r})=R_{nl}(r)Y_{lm}(\vartheta,\varphi) \tag{2.1}$$

where $R_{nl}(\mathbf{r})$ is the radial wave function and $Y_{lm}(\vartheta,\varphi)$ is the spherical harmonic.

The final continuum state is taken as a superposition of an incoming spherical and an outgoing plane wave, which can be expanded in products of spherical harmonics [6]:

$$\Psi_{\mathbf{k}}(\mathbf{r}) = 4\pi\sum_{l'=0}^{\infty} i^{l'} e^{-i\xi_{l'}} G_{kl'}(r) \sum_{m=-l'}^{+l'} Y^{*}_{l'm}(\Theta,\Phi) Y_{l'm}(\vartheta,\varphi) \tag{2.2}$$

with G_{kl} being the radial part of the wavefunction of the l^{th} partial wave, $\xi_{l'}$ the corresponding phase shift, and the Y_{lm} are spherical harmonics, where primes distinguish the final (continuum) state. The spherical coordinates of $\mathbf{k}$ (electron

wave vector) and **r** (electron position vector) are denoted by (k, Θ,Φ) and (r, ϑ, φ), respectively.

Let the interaction Harmiltonian between the atom and a radiation field be H'. The angular distribution of the photoelectrons in single-photon ionization process is then proportional to the square of the absolute value of the matrix element

$$\frac{d\sigma}{d\Omega} \propto \left|\langle \Psi_k | H' | \Psi_{nlm} \rangle\right|^2, \tag{2.3}$$

where ψ_{nlm} is the initial state of the system, and $\psi_{\mathbf{k}}$ is the wave function of the electron in the continuum. In the dipole approximation, we have

$$H' = -e\mathbf{E}\cdot\mathbf{r} = -eE\hat{\varepsilon}\cdot\mathbf{r},$$

where **E** is the electric field of the light and $\hat{\varepsilon}$ is the polarization vector. Eq. (2.3) can be expressed as

$$\frac{d\sigma}{d\Omega} \propto \left|\langle \Psi_{\mathbf{k}} | \hat{\varepsilon}\cdot\mathbf{r} | \Psi_{nlm} \rangle\right|^2. \tag{2.4}$$

If the optical field is linearly polarized and we take the polarization in the z direction, i.e. $\hat{\varepsilon}$=(0, 0, 1). then, $\hat{\varepsilon}\cdot\mathbf{r} = r\cos\vartheta$ and the angular distribution in a single-photon ionization process can be explicitly expressed as

$$\frac{d\sigma}{d\Omega} = \frac{\sigma_T}{4\pi}\left(1 + \beta P_2(\cos\Theta)\right) \tag{2.5}$$

where σ_T is total cross section for single-photon ionization, β is the asymmetry parameter that characterizes the PAD and $P_2(\cos\Theta) = \frac{1}{2}(3\cos^2\Theta - 1)$ is the second-order Legendre polynomial.

In multiphoton ionization processes, for linearly-polarized light the electron angular distribution can be expressed in a general form

$$\frac{d\sigma^{(N)}}{d\Omega} = \frac{\sigma_T^{(N)}}{4\pi} \sum_{j=0}^{N} \beta_{2j} P_{2j}(\cos\Theta), \tag{2.6}$$

where $\sigma_T^{(N)}$ is so called generalized total cross section for N photon ionization. It is expressed in units of $cm^{2N}s^{N-1}$; the coefficients β_{2j} are functions of microscopic atomic parameters and are independent of light intensity; P_{2j} are Legendre polynomials.

For two-photon ionization N=2, Eq. (2.6) becomes

$$\frac{d\sigma}{d\Omega} = \frac{\sigma_T}{4\pi}\left[1 + \beta_2 P_2(\cos\Theta) + \beta_4 P_4(\cos\Theta)\right]. \tag{2.7}$$

In the conventional technique of measuring the angular distribution of photoelectrons, the experimenters use linearly-polarized light to measure the photoelectron flux in the plane transverse to the laser beam. The axis of the quantization is determined by the direction of the electric vector $\hat{\varepsilon}$. The angle Θ is then the angle between the axis of quantization and the axis of the photoelectron detector. The angle Θ may be varied by rotating the direction of the electric field vector with a half-wave plate or $\lambda/2$ rhomb, while keeping the detector position fixed. See Fig. 2.5 for the geometry. With this experimental configuration one could obtain the angular distribution of the photoelectrons in a specific plane. Examples of the angular distributions from atomic rubidium using the conventional technique are shown in Fig. 2.6 [50].

The coefficients β_2 and β_4 can be obtained by fitting data to equation (2.7) (see the solid lines in Fig. 2.6). These coefficients are functions of three

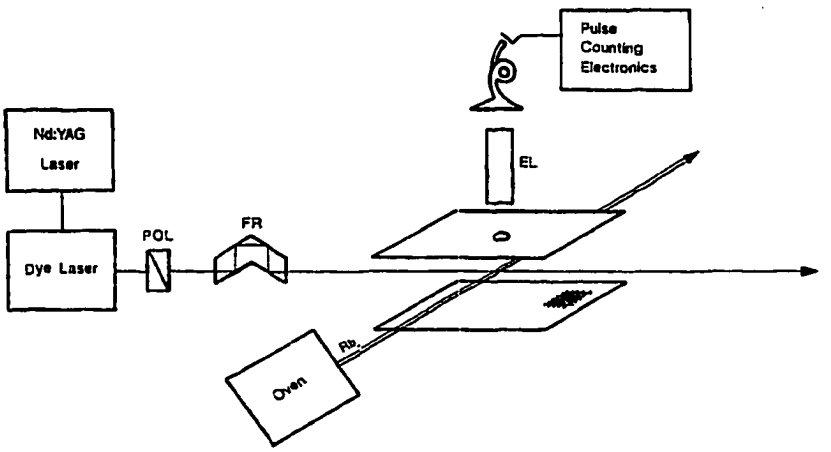

Figure 2.5: The experimental set-up for the measurement of photoelectron angular distributions by the conventional technique. The polarizer (POL) and Fresnel rhomb (FR) rotate the direction of linear polarization of the laser output. Photoelectrons ejected in the direction of the aperture in the upper shielding plate are focused by the electron lens (EL) on to the channel electron multiplier.
(Y.-Y. Yin and D.S. Elliott, Phys. Rev. A, **47**, 2881 (1993))

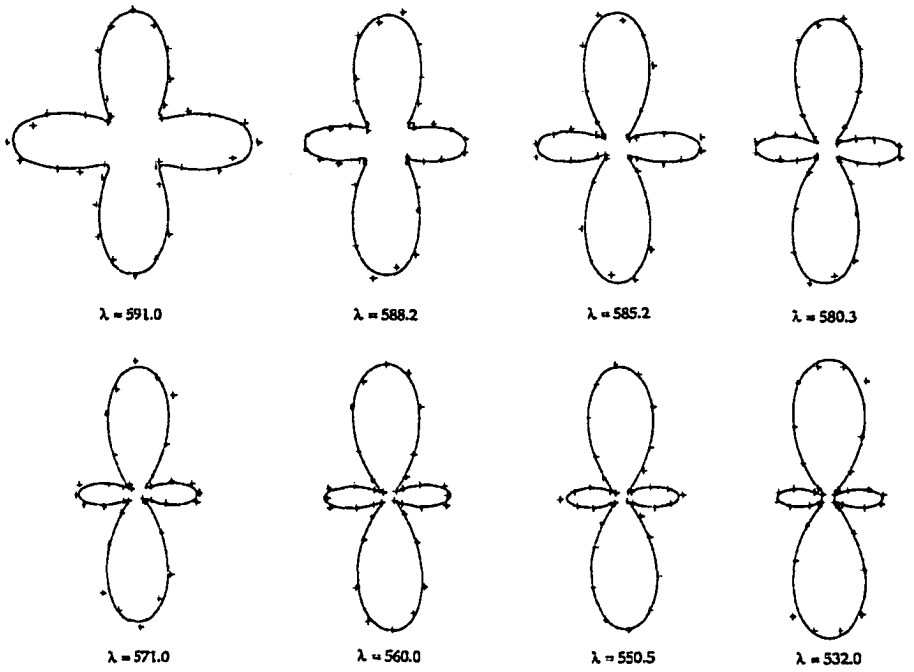

Figure 2.6: Examples of photoelectron angular distributions obtained by the conventional technique. The laser polarization is vertical in this figure. The smooth curves are least-squares-fitting to the data points (+). (Y.-Y. Yin and D.S. Elliott, Phys. Rev. A, **47**, 2881 (1993))

parameters: the phase difference between the *s*- and *d*-partial waves, $\Delta\xi = \xi_s - \xi_d$, the relative cross section of the *s*- and *d*-partial waves, σ_s/σ_d, and the relative cross section for photo-excitation of two fine structure components of the *d*-wave, $\sigma_{5/2}/\sigma_{3/2}$. In order to determine the three atomic parameters from two coefficients β_2 and β_4, additional measurements or theoretical results are required. Additionally, as we mentioned earlier, this measurement does not yield the phase differences directly, but its cosine value instead. The cosine function is bi-valued in the range $0 \sim 2\pi$, so this ambiguity must be solved by some other methods. In

order to help understand how to obtain the atomic parameters from the measurements of angular distributions with conventional technique we give a brief review of Yin and Elliott's work [50] in Appendix A.

In order to show the influence of the atomic parameters on the angular distributions, we plot several two-dimensional figures by changing the three parameters. Fig. 2.7 shows the pure *s*-wave (a) and pure *d*-wave (b). Fig. 2.8 ~ Fig. 2.10 show the superposition of the *s*- and *d*-waves. For the pure *d*-wave in Fig. 2.7b, the distribution has a null point at $\Theta = \pm 54.74°$ and $\pm 125.26°$, while for the superposition of the *s*- and *d*-waves, there is no null point for any of the distributions showing on Fig. 2.8 ~ Fig. 2.10. Instead, each of them has four dips (see Fig. 2.8b for the details) between the main lobes and the side lobes. In Fig. 2.8, the four curves represent angular distributions with the phase difference $\Delta\xi=0$ (blue curve), $\Delta\xi=\pi/4$ (red curve), $\Delta\xi=\pi/2$ (dark blue curve) and $\Delta\xi=\pi$ (green curve), respectively. The ratios of the cross sections are $\sigma_{5/2}/\sigma_{3/2}=11.5$ and $\sigma_s/\sigma_d=0.2$ for all the cases. From this figure we see that the maximum flux of the electrons is along the laser polarization (z-direction). As the phase difference increases, the main lobes along the z-axis become larger and larger, while the side lobes (i.e. the side ring around the waist of the angular distribution) become smaller. When $\Delta\xi=\pi$, the side lobes shrink to the minimum, and the main lobes increase to the maximum. In Fig. 2.9, we plot three distributions with the ratios of the cross section $\sigma_s/\sigma_d=0.1$ (blue curve), $\sigma_s/\sigma_d=0.4$ (red curve) and $\sigma_s/\sigma_d=0.7$ (green curve); for each of the three cases, $\sigma_{5/2}/\sigma_{3.2}=11.5$ and the phase difference $\Delta\xi=\pi/2$. Increasing the ratio σ_s/σ_d, decreases the main lobes and increases the side lobes. The distance of the opposite dips in the polar plot decreases with decreasing ratio σ_s/σ_d. When $\sigma_s/\sigma_d=0$, the case of pure *d*-wave, the four dips shrink to a null point (see Fig. 2.7 b). Fig. 2.10 shows the distributions with two different ratios of the cross sections between two *D* fine structure channels, $\sigma_{5/2}/\sigma_{3/2}=11.5$ (blue

curve) and $\sigma_{5/2}/\sigma_{3/2}=1.5$ (red curve). We maintain the phase difference $\Delta\xi=\pi/2$ and the ratio of cross sections $\sigma_s/\sigma_d=0.2$ for both the cases. These plots indicate the influence of the fine structure of the two *D* channels. $\sigma_{5/2}/\sigma_{3/2}=1.5$ is the case that the fine structure is negligible. This quantity affects the main lobes more than the side lobes. It is different from the other two parameters. Larger $\sigma_{5/2}/\sigma_{3/2}$ makes both main lobes and the side lobes smaller, but the four dips separate farther.

From these figures we learn that the angular distribution is affected by any of the three atomic parameters. The influence of the phase difference between *s*- and *d*-waves and σ_s/σ_d on PAD is much greater than that of the ratio $\sigma_{5/2}/\sigma_{3/2}$. This can be seen from Fig. 2.10, as $\sigma_{5/2}/\sigma_{3/2}$ changes from 1.5 to 11.5 (~ 8 times) the angular distribution only changes a little. The maximum of the main lobes increase ~10% and that the side lobes decrease ~10%. This argument suggests that the phase difference and σ_s/σ_d can be determined more accurately than $\sigma_{5/2}/\sigma_{3/2}$ from measurements of the photoelectron angular distribution.

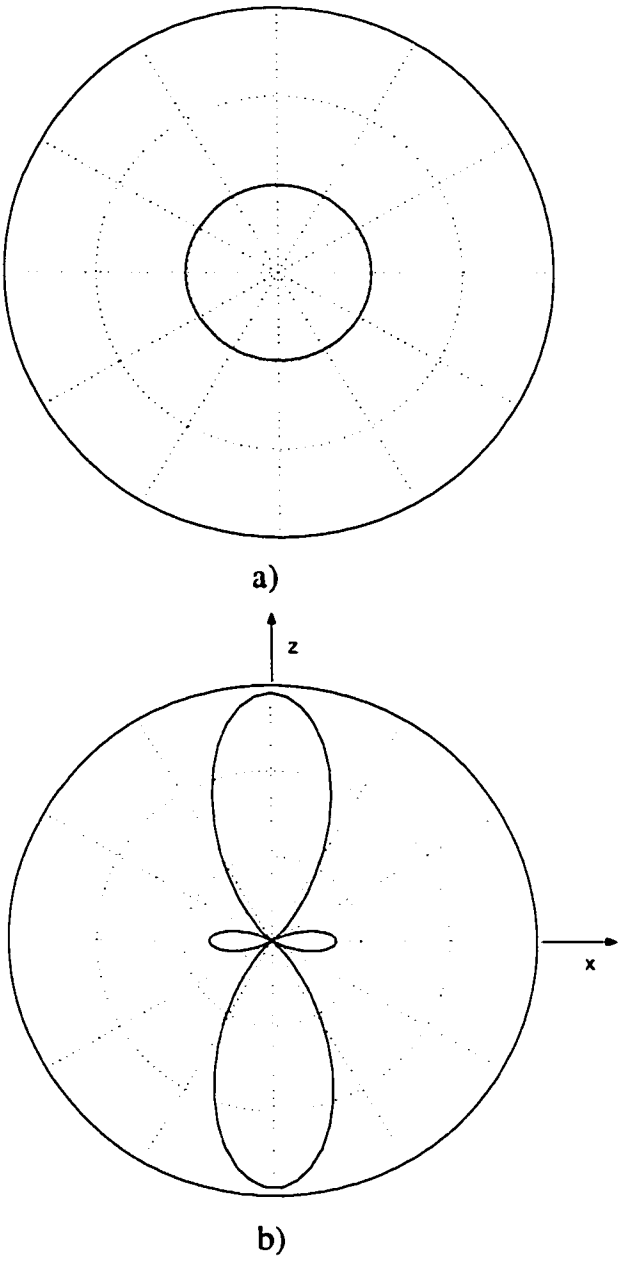

Figure 2.7: The angular distribution of photoelectrons for a) a pure *s*-wave and b) a pure *d*-wave.

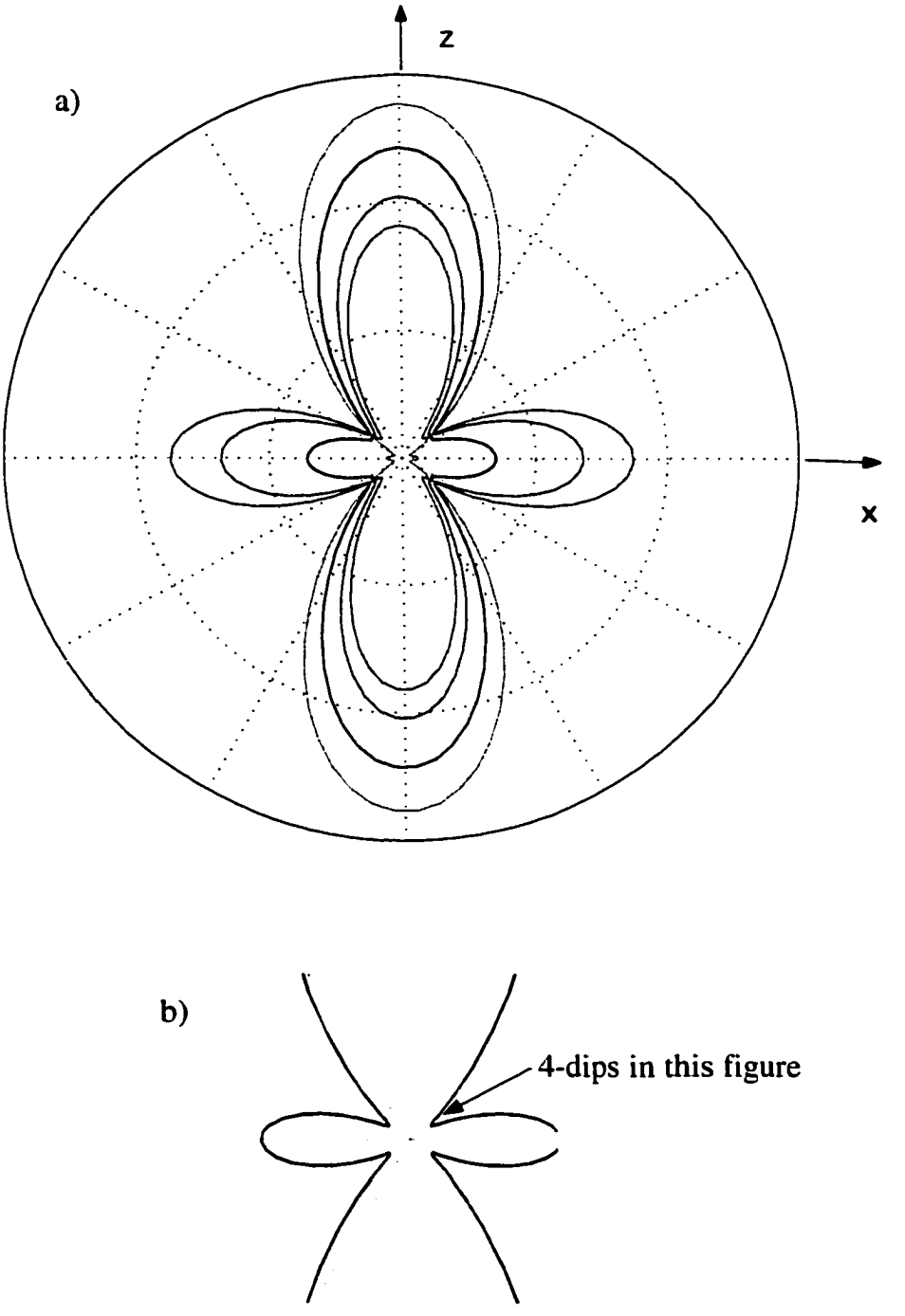

Figure 2.8: The effect of phase difference $\Delta\xi$ on angular distribution. blue curve: $\Delta\xi=0$, red curve: $\Delta\xi=\pi/4$, dark blue curve: $\Delta\xi=\pi/2$, green curve: $\Delta\xi=\pi$, $\sigma_{5/2}/\sigma_{3/2}=11.5$ and $\sigma_s/\sigma_d=0.2$ for all the cases.

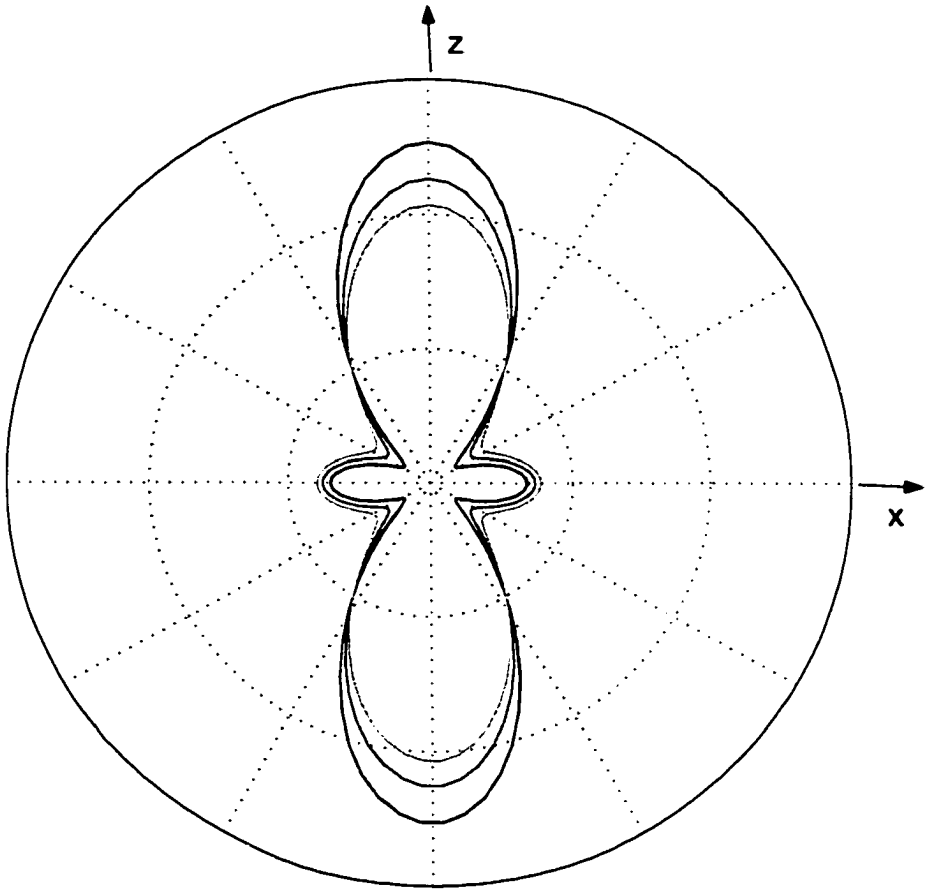

Figure 2.9: The effect of σ_s / σ_d on the angular distribution.
blue curve: $\sigma_s / \sigma_d = 0.1$, red curve: $\sigma_s / \sigma_d = 0.4$, green curve: $\sigma_s / \sigma_d = 0.7$.
$\sigma_{5/2} / \sigma_{3,2} = 11.5$ and the phase difference $\Delta\xi = \pi/2$ radian for all the cases.

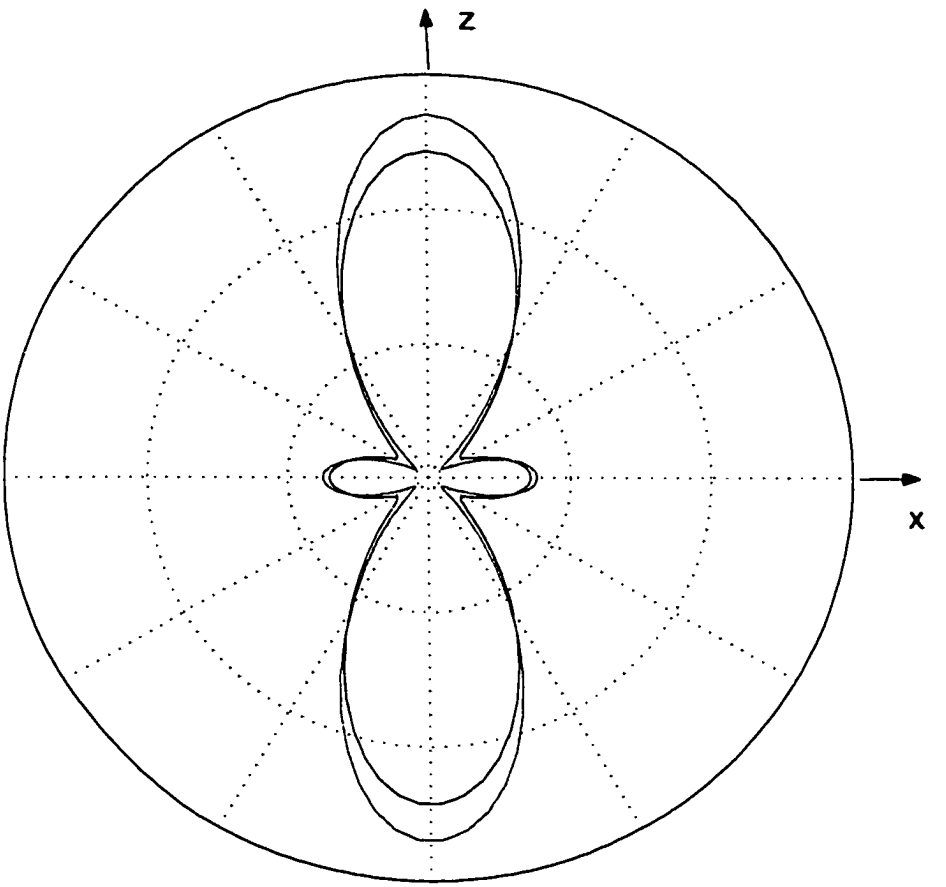

Figure 2.10: The effect of $\sigma_{5/2}/\sigma_{3/2}$ on the angular distribution. blue curve: $\sigma_{5/2}/\sigma_{3/2}=11.5$, red curve: $\sigma_{5/2}/\sigma_{3/2}=1.5$. $\sigma_s/\sigma_d=0.2$ and the phase difference $\Delta\xi=\pi/2$ radian for both the cases.

2.5 Summary of the theory of photoelectron angular distributions in two-photon ionization with arbitrarily-polarized light

We have mentioned that the major disadvantage for the determination of atomic parameters using linearly-polarized light is that a single measurement of the PAD is not sufficient to determine all the three parameters uniquely. One has to use the data from other experiments or theory to supplement the measurement of the PAD. In order to perform a complete determination of the atomic parameters using our newly developed technique, a general theory of the photoelectron angular distribution resulting from the two-photon ionization of rubidium with arbitrarily-polarized light is required. Elliott extended Lambropoulos and Teague's theoretical work [11] on the two- and three-photon ionization of alkali metals excited by linearly- and circularly-polarized light to include the case of arbitrarily-polarized light.

In order to describe the measurement of photoelectron angular distributions using elliptically-polarized light, we present the essentials of Elliott's theoretical work [53]. Based on the extended theory, the photoelectron angular distribution resulting from the two-photon interaction of rubidium with arbitrarily-polarized light can be expressed as

$$\frac{d\sigma}{d\Omega} = \frac{m\alpha^2\omega^2|\vec{k}|}{2\hbar} \sum_{i,j=+/-} |T_{ij}^{(33)}\epsilon_3^2 + T_{ij}^{(13)}\epsilon_1\epsilon_3 + T_{ij}^{(11)}\epsilon_1^2|^2, \tag{2.8}$$

where $T_{ij}^{(pq)}$ are the spatial components of the two-photon transition moments. The indices i, j =+ or - of the moments $T_{ij}^{(pq)}$ represent the spins of the ground and final state electrons, respectively, and p, q=1 or 3 represent the relevant spatial

components. ϵ_1 and ϵ_3 are two components of the unit vector $\hat{\epsilon}=\epsilon_1\hat{x}+\epsilon_3\hat{z}$ that describe the polarization of the laser field

$$\vec{E}(\vec{r},t)=E_0\,\hat{\epsilon}\exp[-i(\omega t-\beta y)]+\text{c.c.}, \tag{2.9}$$

where $+\hat{y}$ is the direction of propagation of the laser beam and the $\hat{z}$ axis is assigned as the vertical direction in our experiment. Depending on the relative magnitude and phase difference of the two components ϵ_1 and ϵ_3, the field may be linear, circular or elliptical, in a left-hand or right-hand sense. One polarization state of special interest in the present work is $\hat{\epsilon}=i\epsilon_1''\hat{x}+\epsilon_3'\hat{z}$, where ϵ_1'' and ϵ_3' are real and positive, and $\epsilon_1''\neq\epsilon_3'$. This vector describes left-elliptically-polarized light, where we conform with the convention of Born and Wolf [61] for labeling the sense of rotation. In this state the $\hat{z}$ component leads the $\hat{x}$ component, and the electric field vector rotates counterclockwise as a function of time as viewed by an observer facing the laser source. The major axis of the ellipse is vertical for $\epsilon_3'>\epsilon_1''$ and horizontal for $\epsilon_3'<\epsilon_1''$. By parallel arguments, the vector $\hat{\epsilon}=-i\epsilon_1''\hat{x}+\epsilon_3'\hat{z}$ describes right-elliptically-polarized light, which rotates clockwise when viewed by the same observer

The explicit forms of these moments are

$$T_{++}^{(33)}=\frac{1}{3}e^{i\xi_s}Y_{00}(\Theta,\Phi)S_{\bar{s}}-\frac{2}{3\sqrt{5}}e^{i\xi_d}Y_{20}(\Theta,\Phi)S_{\bar{d}}, \tag{2.10a}$$

$$T_{++}^{(13)}=\frac{1}{\sqrt{30}}e^{i\xi_d}\{2[Y_{21}(\Theta,\Phi)-Y_{2-1}(\Theta,\Phi)]S_{\bar{d}} -[Y_{21}(\Theta,\Phi)+Y_{2-1}(\Theta,\Phi)]S_{\Delta d}\}, \tag{2.10b}$$

$$T_{++}^{(11)}=\frac{1}{3}e^{i\xi_s}Y_{00}(\Theta,\Phi)S_{\bar{s}}+e^{i\xi_d}\left\{\frac{1}{3\sqrt{5}}Y_{20}(\Theta,\Phi)S_{\bar{d}}\right.$$

$$-\frac{1}{\sqrt{30}}\{[Y_{22}(\Theta,\Phi)+Y_{2-2}(\Theta,\Phi)]S_{\bar{d}}$$

$$\left.-[Y_{22}(\Theta,\Phi)-Y_{2-2}(\Theta,\Phi)]S_{\Delta d}\}\right\}, \qquad (2.10c)$$

$$T_{+-}^{(33)}=\sqrt{\frac{2}{15}}e^{i\xi_d}Y_{21}(\Theta,\Phi)S_{\Delta d}, \qquad (2.10d)$$

$$T_{+-}^{(13)}=\frac{1}{\sqrt{5}}e^{i\xi_d}\left[Y_{20}(\Theta,\Phi)-\sqrt{\frac{2}{3}}Y_{22}(\Theta,\Phi)\right]S_{\Delta d}, \qquad (2.10e)$$

$$T_{+-}^{(11)}=-\frac{1}{\sqrt{30}}e^{i\xi_d}[Y_{21}(\Theta,\Phi)-Y_{2-1}(\Theta,\Phi)]S_{\Delta d}. \qquad (2.10f)$$

The - - (- +) component is obtained from the + + (+ -) component by changing Y_{lm} $\rightarrow$ $Y_{l\,-m}$ and by changing the sign of the (13) component. The reduced two-photon transition moments $S_{\bar{s}}$ represent the average transition moment for excitation of the *S* continuum,

$$S_{\bar{s}}=(S_1+2S_2)/3,$$

the average transition moment for excitation of the *D* continuum,

$$S_{\bar{d}}=(5S_3+S_4+9S_5)/15,$$

and the asymmetry between the transition moments for the $D_{5/2}$ and $D_{3/2}$ waves,

$$S_{\Delta d}=(5S_3+S_4-6S_5)/15.$$

The notation S_1 ~ S_5 represent the radial transition moments for the various intermediate and final states for the two-photon transitions. We have discussed this notation in preceding section. In the case of linearly-polarized light, Eqs. (2.8) and (2.10) reduce to a special form of Eqs. (A1) and (A3), respectively, (see Appendix A).

The general definition for these moments

$$S=4\pi\sum_{n}\frac{\langle f|r|np\,^2P_j\rangle\langle np\,^2P_j|r|g\rangle}{\omega_{n,j}-\omega}, \tag{2.11}$$

was originally used by Lambropoulos and Teague [11]. $\langle f|$ is one of the three outgoing channels $\varepsilon\, s\ ^2S_{1/2}$, $\varepsilon\, d\ ^2D_{3/2}$,or $\varepsilon\, d\ ^2D_{5/2}$, and j=1/2 or 3/2 is the electronic angular momentum of the intermediate state.

The total photoionization cross sections for the three channels can be obtained by integrating the angular distribution of Eq. (2.8) over all angles, yielding

$$\begin{aligned}\sigma&=\int\frac{d\sigma}{d\Omega}d\Omega\\&=\frac{m\alpha^2\omega^2|\vec{k}|}{\hbar}\left\{\frac{1}{9}\left[S_{\frac{3}{2}}^2+\frac{8}{25}\left(\frac{5S_3+S_4}{6}\right)^2+\frac{12}{25}S_5^2\right]\right.\\&\left.+\frac{1}{9}\left[S_{\frac{3}{2}}^2-\frac{4}{25}\left(\frac{5S_3+S_4}{6}\right)^2-\frac{6}{25}S_5^2\right](\epsilon_1\epsilon_3^*-\epsilon_1^*\epsilon_3)^2\right\}.\end{aligned} \tag{2.12}$$

For linear polarization the second term in Eq. (2.12) vanishes. The two-photon cross sections, σ_s, $\sigma_{3/2}$, and $\sigma_{5/2}$, for photoionization into the $\varepsilon\, s\ ^2S_{1/2}$, $\varepsilon\, d\ ^2D_{3/2}$,or $\varepsilon\, d\ ^2D_{5/2}$ channels, respectively, and the total cross section for the d-wave, $\sigma_d=\sigma_{3/2}+\sigma_{5/2}$ can then be expressed as the following forms

$$\begin{aligned}\sigma_s&=\frac{m\alpha^2\omega^2|\vec{k}|}{\hbar}\frac{1}{9}\left(\frac{S_1+2S_2}{3}\right)^2,\\\sigma_{3/2}&=\frac{m\alpha^2\omega^2|\vec{k}|}{\hbar}\frac{8}{225}\left(\frac{5S_3+S_4}{6}\right)^2,\\\sigma_{5/2}&=\frac{m\alpha^2\omega^2|\vec{k}|}{\hbar}\frac{12}{225}S_5^2,\\\sigma_d&=\frac{m\alpha^2\omega^2|\vec{k}|}{\hbar}\frac{4}{45}\left(S_{\frac{1}{d}}^2+\frac{3}{2}S_{\Delta d}^2\right).\end{aligned} \tag{2.13}$$

In the absence of spin-orbit coupling in the intermediate or continuum states, $S_1 = S_2$ and $S_3 = S_4 = S_5$ (refer to Figs. 2.3 ~ 2.5). The relation, $S_3 = S_4 = S_5$, yields $\sigma_{5/2} = 1.5\sigma_{3/2}$.

For circular polarization, with $\pm i\epsilon_1 = \epsilon_3 = 1/\sqrt{2}$, the polarization factor in Eq. (2.12), $(\epsilon_1 \epsilon_3^* - \epsilon_1^* \epsilon_3)^2$ becomes -1, the excitation of the *s*-wave vanishes (the two terms with S_s^2 are cancelled), while the excitation rate of the *d*-wave increases by a factor of 1.5 over that for linear polarization. For any other polarization state, the effective cross section for the partial waves lies between these two extremes.

Based on the general formula (2.8), we can plot the photoelectron angular distributions with any polarization. Examples of three-dimensional angular distributions for two-photon ionization, resulting from three different polarization states of the optical field, are shown in Fig. 2.11. These distributions correspond to (a) linearly-polarized light, (b) right-elliptically-polarized light, and (c) circularly-polarized light. In each case, the laser beam is propagating in a direction nearly normal to the plane of the page (the $+\hat{y}$ direction). The distribution for linearly-polarized light is symmetric about an axis parallel to the laser polarization (i.e. the

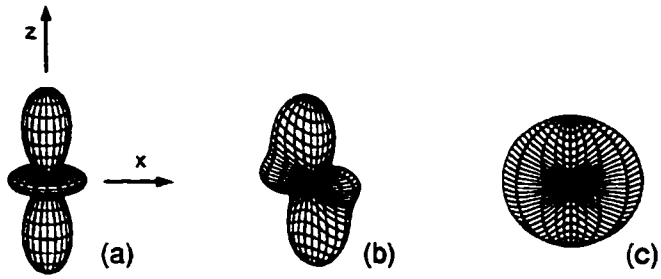

Figure 2.11: Examples of calculate photoelectron angular distributions for (a) linearly-polarized light, (b) right-elliptically-polarized light, and (c) circularly-polarized light. The propagation direction of laser beam is nearly into the plane of the page.

$\hat{z}$ axis in Fig. 2.11), while that for circularly-polarized light is symmetric about the axis defined by the laser propagation direction (the $\hat{y}$ axis). The symmetry of the angular distribution for elliptical polarization is reduced, but inversion symmetry about the origin is still evident. The asymmetry of this distribution reverses as the sense of the elliptical polarization is reversed.

Now we discuss the advantage of using elliptically-polarized light in the measurements of multiphoton ionization process, specifically, its unique ability to establish a complete measurement. It is instructive to reduce the general expressions for $d\sigma/d\Omega$ given in Eqs. (2.8) and (2.10), valid for all angles Θ and Φ, to the form restricted only in the x-z plane, i.e. $\Phi=0$ or π, and with the limited polarization state defined earlier, $\epsilon_1 = i\epsilon_1''$ and $\epsilon_3=\epsilon_3'$, where ϵ_1'' and ϵ_3' are real. This is a elliptically-polarized light. (We remove our previous restriction that ϵ_1'' and ϵ_3' are positive, allowing the sign of $\epsilon_1'' \epsilon_3'$ to indicate the sense of rotation of the field vector.) The angular distribution in this plane then takes the form

$$\begin{aligned}\frac{d\sigma}{d\Omega} = \frac{m\alpha^2\omega^2|\vec{k}|}{4\pi\hbar}\Bigg\{\Bigg|&\frac{1}{3}(e^{i\xi_s}S_{\bar{s}}^{-} - e^{i\xi_d}S_{\bar{d}}(3\cos^2\Theta - 1))\epsilon_3'^2 \\ &- 2ie^{i\xi_d}S_{\bar{d}}\sin\Theta\cos\Theta\epsilon_1''\epsilon_3' \\ &- \frac{1}{3}(e^{i\xi_s}S_{\bar{s}}^{-} + e^{i\xi_d}S_{\bar{d}}(3\cos^2\Theta - 2))\epsilon_1''^2\Bigg|^2 \\ &+ |-\sin\Theta\cos\Theta(\epsilon_3'^2 + \epsilon_1''^2) \\ &+ i(2\cos^2\Theta - 1)\epsilon_1''\epsilon_3'|^2 S_{\Delta d}^2\Bigg\}. \end{aligned} \tag{2.14}$$

This equation can be expressed as a harmonic series

$$\frac{d\sigma}{d\Omega}=\frac{m\alpha^2\omega^2|\vec{k}|}{4\pi\hbar}a_0(1+a_2\cos 2\Theta+a_4\cos 4\Theta+b_2\sin 2\Theta), \tag{2.15}$$

where

$$a_0=\frac{1}{9}\left(S_{\bar{s}}^2-S_{\bar{s}}S_{\bar{d}}\cos(\xi_s-\xi_d)+\frac{1}{4}S_{\bar{d}}^2\right)(\epsilon_3'^2-\epsilon_1''^2)^2$$
$$+\frac{1}{8}(S_{\bar{d}}^2+S_{\Delta d}^2)(\epsilon_3'^4+6\epsilon_1''^2\epsilon_3'^2+\epsilon_1''^4), \tag{2.16a}$$

$$a_2=\frac{1}{3a_0}[S_{\bar{d}}^2/2-S_{\bar{s}}S_{\bar{d}}\cos(\xi_s-\xi_d)](\epsilon_3'^4-\epsilon_1''^4), \tag{2.16b}$$

$$a_4=\frac{1}{8a_0}(S_{\bar{d}}^2-S_{\Delta d}^2)(\epsilon_3'^2-\epsilon_1''^2)^2, \tag{2.16c}$$

$$b_2=-\frac{2}{3a_0}S_{\bar{s}}S_{\bar{d}}\sin(\xi_s-\xi_d)\epsilon_3'\epsilon_1''(\epsilon_3'^2-\epsilon_1''^2). \tag{2.16d}$$

The coefficient a_0 only affects the overall amplitude of the photoelectron flux, but does not influence the shape of the angular distribution, which is determined completely by the three coefficients a_2, a_4, and b_2. These three coefficients are uniquely defined in terms of the ratios of reduced transition moments $S_{\bar{s}}/S_{\bar{d}}$ and $S_{\Delta d}/S_{\bar{d}}$, and the phase difference ξ_s - ξ_d, or equivalently σ_s/σ_d, $\sigma_{5/2}/\sigma_{3/2}$, and ξ_s - ξ_d. In the case of linear vertical polarization, which corresponds to $\epsilon_3'=1$ and $\epsilon_1''=0$, the coefficient b_2 vanishes. This distribution is symmetric about the $\hat{z}$ axis (see Fig. 2.11a). A measurement of this distribution alone is sufficient to determine only two of the three atomic parameters. We have already discussed this important point earlier. We have also mentioned that since this distribution depends on $\cos(\xi_s - \xi_d)$, not on the phase difference itself, an additional ambiguity results. However,

use of the elliptical polarization ($\epsilon_3' \neq \epsilon_1''$, and each nonzero!) will yield an asymmetric angular distribution whose only symmetry is upon inversion about the origin. The coefficient b_2 is not equal to zero in this case. The three fitting coefficients a_2, a_4, and b_2 uniquely determine the angular distribution, and hence all three of the atomic parameters can be determined simultaneously.

In the experiments we describe in this thesis, we collect photoelectrons ejected in all directions, not limited to the x-z plane. These 4π solid angle distributions are, of course, also sensitive to the ellipticity of the laser polarization, and our measurements exploit this to make our complete determinations.

CHAPTER 3
A NEW TECHNIQUE FOR MEASUREMENT OF PAD

This chapter describes the essentials of the technique we developed for the measurement of photoelectron angular distributions and the principle of the determination of atomic parameters. We discuss three parts of this technique in this chapter:

1. A specially designed micro-channel plate (MCP) electron detector, which collects the photoelectrons and forms a two-dimensional image on a phosphor screen of the MCP assembly.
2. Analysis of the trajectories of the photoelectrons for calculated images.
3. The data acquisition system.

We use this technique to carry out the complete measurements of two-photon ionization of rubidium as well as the quantum interference measurements with two-color laser fields.

3.1 Introduction

The first goal of the research discussed in this thesis is to develop a technique for determination of microscopic atomic parameters without relying on any other sources. To accomplish this goal we have developed a new approach to collect the photoelectrons for the measurements of angular distributions and introduced the use of elliptically-polarized light (as described in Sec. 2.5) to make the determination possible. In this chapter we describe this technique and the benefits it presents over the conventional method.

The conventional technique for measuring the angular distribution has encountered some problems. In this technique, the electrons are collected in a plane transverse to the laser beam by a single channel electron detector at different angles. This is customarily accomplished by fixing the detector in the vacuum chamber and rotating the laser polarization [e.g. 15, 25, 26, 32, 33, 49, 50]. The measured angular distribution is actually only a two-dimensional polar plot in a plane perpendicular to the laser direction. This polar plot is only a cross section of a 3-dimentional distribution (see Fig. 2.6). Because of this limitation, one could lose some information necessary to determine the atomic parameters and introduce a large uncertainty of the extracted quantities. Furthermore, only linearly-polarized light is used for the experimental convenience. This configuration leads to a problem that the three atomic parameters cannot be determined by these measurements alone. It must be augmented by results from another experiment or data from theory. Another drawback is that this experiment does not yield the phase differences directly, but its cosine value instead. Since the cosine function is bi-valued in the range $0 \sim 2\pi$, this ambiguity must be resolved by some other methods. In a recent theoretical work, it is pointed out [77]: "... In principle these quantities could be *indirectly* determined by measuring PADs and fitting theoretical curves to them. However, experimental errors could lead to the large uncertainty of the extracted phase shift after fitting. More importantly, apart from such an experimental uncertainty, there is a serious problem in the use of the PAD technique for determining phase shifts; for example, for nonresonant two-photon ionization of alkali-metal atoms from the *s* state, there are two fitting parameters, while *three* parameters are theoretically required for the unambiguous determination of phase shifts... If the spin-orbit interaction is not negligible, three independent physical quantities cannot be extracted from the two fitted quantities, i.e., the PAD technique faces a serious problem."

The technique we developed thoroughly solved these problems. It is completely different from the conventional technique, and includes two new developments: a detector to measure the angular distribution by collecting the photo-electrons emitted into a 4π steradian space and the use of elliptically-polarized light in making a unique determination of the three atomic parameters.

With our technique, there is no need to rotate the polarization of the laser field while collecting the data, as the electrons ejected into the entire 4π steradian solid angle are collected by a Micro-Channel Plate (MCP) assembly and projected onto its phosphor screen. Each photoelectron creates a bright spot on the phosphor screen (refer to Fig. 3.1). After accumulating the electrons over thousands of laser shots, a two-dimensional electron image forms on the phosphor screen. The image is recorded by a CCD camera and stored by a computer. This image represents the angular distribution of the photoelectrons and allows us to determine the three microscopic parameters of the rubidium atom in the photo-ionization process.

The other critical distinction with the conventional technique is that we use elliptically-polarized light to measure the angular distribution instead of using linearly-polarized light. It is unique in that using elliptically-polarized light can constitute a complete photo-ionization measurement. With linearly-polarized light in the measurements the two fitting parameters are not enough to extract the three atomic parameters as mentioned above, while with elliptically-polarized light, there are three fitting parameters to fit the angular distribution images. In our analysis, we first create a theoretical image based on the experimental conditions using elliptically-polarized light, and then we fit the calculated image data to the measured image data by adjusting the three atomic parameters. These three parameters are determined simultaneously with the best fit of the calculated image to the measured image. We will discuss the details of this method in Chapter 5.

These measurements represent a complete determination of the relative photo-ionization cross-sections and continuum wave function phase differences

interfaced to a laboratory computer to record the images on the phosphor screen and use a monitor to observe the bright spots on the screen. The brightness of the spots depends on the voltages V_a and V_o. We find that the voltage on the phosphor screen V_a controls the brightness of the electron images more than the output voltage V_o does. The image should be taken with adequate brightness of the spots and with discrete spots showing on the monitor.

Fig. 3.2 is a photograph of the detector in the vacuum chamber.

This detector was originally introduced by Helm *et al* [52]. In order to measure asymmetric angular distributions, we had to modify his original design. It is well known that there are two parabolic trajectories that start from the source (i.e. the interaction region) and strike the micro-channel plate at the same point. In the case of asymmetric angular distributions, it is necessary to separate the electrons initially ejected in all directions to preserve the asymmetric property of the image on the phosphor screen of MCP. The image is a two-dimensional projection of the photoelectron angular distribution. This is very important for us to extract the correct atomic parameters from the images. The original apparatus failed to do this. We have successfully made a modification to separate the overlapped electrons on the two-dimensional distribution images by using very low field strengths in the region between the two field plates, and by keeping the interaction region near to the upper plate (5.5 mm). The distance between the two meshes is greatly reduced from 10 cm in the original design to 1.35 cm, and the acceleration field strength is reduced from 80 V/cm to ~1 V/cm. This is a critical accomplishment for the experiment in our studies.

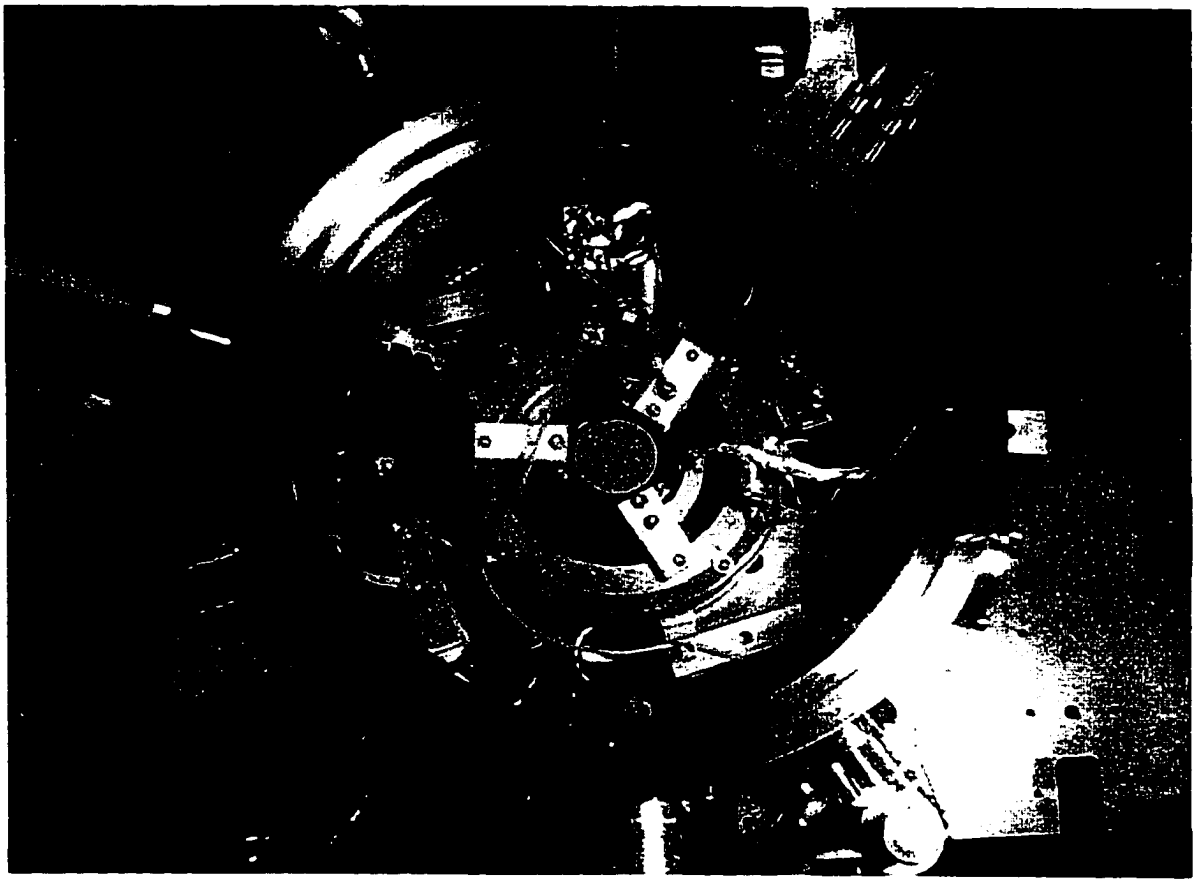

Figure 3.2: Micro-Channel Plate assembly in the vacuum chamber
(Top view)

For comparison, we show two images in Fig. 3.3 produced with our modified detector (Fig. 3.3a) and the one similar to Helm's design (Fig. 3.3b). These two images are taken both with linearly polarized light, 45 degree from vertical. We see that the image in Fig. 3.3a) clearly shows the asymmetric structure with a bright spot and a ring. However, Fig. 3.3b) shows a nearly symmetric image. The bright spot and the ring disappear. The corresponding angular distribution that produces the images is plotted under the images. We will discuss the reason for this difference in next section.

Figure 3.3: Images taken with a) our modified detector and b) the detector of Helm's design. The laser light is linearly polarized, 45° from vertical. The corresponding angular distribution is plotted under the images. The image in a) clearly shows the asymmetric structure with a bright spot and a ring. However, the image b) is a nearly symmetric, and the bright spot and the ring disappear.

3.3 Analysis of trajectories of photoelectrons for calculated images

In order to calculate the theoretical image we need to map the trajectory of the photoelectrons traveling from the interaction region to the phosphor screen of the Micro-Channel Plate assembly. Assuming a photoelectron ejected at an initial angle (Θ,Φ) (refer to Fig. 3.4) with initial kinetic energy ε and mass m, the initial velocity of the electron is $v=\sqrt{2\varepsilon/m}$. In our experimental set-up, the uniform electric dc field is anti-parallel to the z axis, therefore the direction of the acceleration of the electron is in z direction. The magnitude of the acceleration is $a=\frac{eV}{mD}$, where D =1.35 cm is the spacing between the two mesh plates. The angle between the initial momentum of the photoelectron and the uniform field is the same as the polar angle Θ. The equation of the motion of the electron yields

$$\begin{aligned} d &= v_z t + \frac{1}{2} a t^2 \\ &= \sqrt{\frac{2\varepsilon}{m}} \cos\Theta\, t + \frac{eV}{2mD} t^2 \end{aligned} \tag{3.1}$$

and

$$\begin{aligned} r &= v_r t \\ &= \sqrt{\frac{2\varepsilon}{m}} \sin\Theta\, t \end{aligned} \tag{3.2}$$

The meanings of the parameters in Eqs. (3.1) and (3.2) are:

$d \approx 0.55$ cm --- the distance between interaction region and upper mesh,

v_z and v_r --- the z and the radial component of the velocity, respectively,

r--- the transverse distance from the interaction region to the landing point of the electron on the upper mesh (see Fig. 3.4),

V --- the potential difference between the plates,

e --- the electronic charge, and

t --- the time required for the electron to reach the upper mesh from the interaction region.

Substituting into Eq. (3.1) with

$$\sqrt{\frac{2\varepsilon}{m}}\,t=\frac{r}{\sin\Theta} \quad \text{and} \quad t=\frac{r}{\sin\Theta}\sqrt{\frac{m}{2\varepsilon}}$$

from Eq. (3.2), we have

$$\frac{eV}{4\varepsilon D}r^2+\sin\Theta\cos\Theta r-d\sin^2\Theta=0.$$

Solving this equation, the transverse distance r can be expressed as a function of the experimental parameters and Θ,

$$r=\frac{2\varepsilon D}{eV}\sin\Theta\left(\sqrt{\cos^2\Theta+\frac{eVd}{\varepsilon D}}-\cos\Theta\right). \tag{3.3}$$

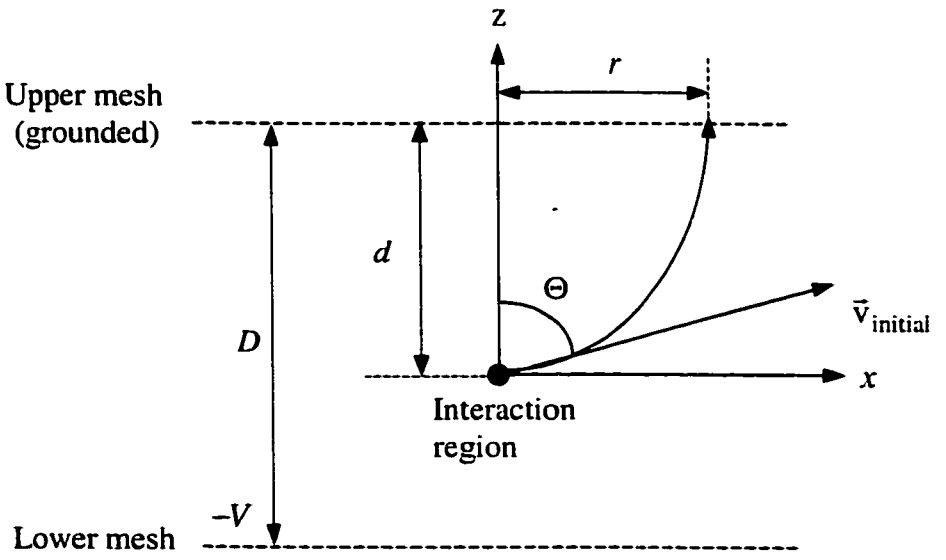

Figure 3.4: Trajectory of the electron in the region between the two mesh plates (not scaled).

Alternatively, we can write an expression for Θ in terms of r from Eq. (3.3)

$$\Theta = \frac{1}{2}\left[\arccos\left(\frac{1}{\sqrt{1+(r/d)^2}}\right) \pm \arccos\left(\frac{1-(eVd/2\varepsilon D)(r/d)^2}{\sqrt{1+(r/d)^2}}\right)\right]. \qquad (3.4)$$

From this equation, we see that each r corresponds to two values of Θ, as expected for parabolic trajectories. After passing through the mesh, the electrons are rapidly accelerated toward the micro-channel plate by a high field (190 V/cm). This field is created by a bias voltage (95 V) between the bottom side of the MCP and the upper mesh, which are separated by ~5 mm (see Fig. 3.1). This design avoids any apparent further transverse motion of the electrons. r therefore can be considered to be the distance between the center of the image and the landing point of the electron on the phosphor screen.

Referring to Fig. 3.5, we can write the differential relative intensity of electron signal detected by a pixel of the CCD array as

$$dI_{i,j} = \frac{d\sigma}{d\Omega}\left|\frac{d\Omega}{dA}\right|\Delta A F^2(\vec{r},t)\rho_{at}dVdt\,, \qquad (3.5)$$

where dσ/dΩ is the magnitude of the photoelectron angular distribution in the direction that electrons project onto the pixel with indices i, j, $|d\Omega/dA|\Delta A$ is the solid angle that maps into the pixel area ΔA, $F(\vec{r},t)$ is the photon flux in the interaction region, and ρ_{at} is the density of the atomic beam. The integrals are taken over the entire interaction volume and the pulse duration. For two photon ionization, the rate is given by $W=\sigma_2 F^2$, where W is expressed in reciprocal second, σ_2 is the generalized 2-photon ionization cross section in cm^4 s. The photon flux is expressed in photons cm^{-2} s^{-1}. Based on these units we can verify that the differential relative intensity of signal $dI_{i,j}$ in Eq. (3.5) is dimensionless.

Integrating Eq. (3.5) over the entire interaction region and over the laser pulse duration, we obtain the relative intensity of the average signal detected by each pixel

$$I_{i,j} = \int_V \int_t \frac{d\sigma}{d\Omega} \left| \frac{d\Omega}{dA} \right| \Delta A F^2(\vec{r},t) \rho_{at} dV dt \,. \tag{3.6}$$

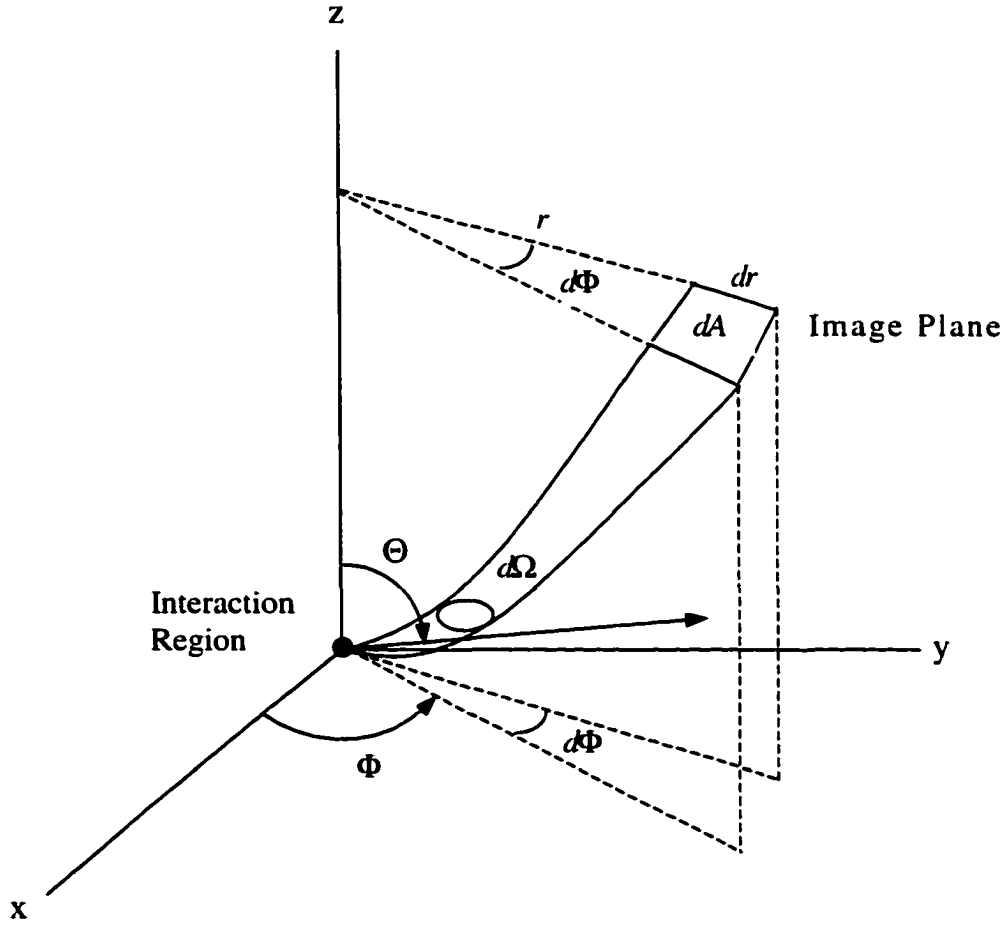

Figure 3.5: Mapping the trajectory of photoelectrons onto image plane

Because the interaction volume is very small compared with the dimension of the geometry of the detector, dσ/dΩ and $|d\Omega/dA|\Delta A$ can be taken out of the integral. The approximation of Eq. (3.6) can be written as

$$I_{i,j} \approx \frac{d\sigma}{d\Omega}\left|\frac{d\Omega}{dA}\right|\Delta A\int_V dV\int_t F^2(\vec{r},t)\rho_{at}dt\,. \tag{3.7}$$

The factor $\int_V dV\int_t F^2(\vec{r},t)\rho_{at}dt$ is difficult to determine with high precision, but can be considered as a constant when the laser intensity is stable. It only affects the overall magnitude of the signal. Eq. (3.7) becomes

$$I_{i,j} \approx \frac{d\sigma}{d\Omega}\left|\frac{d\Omega}{dA}\right|\Delta A\,. \tag{3.8}$$

Based on this equation we can calculate each pixel value (relative) $I_{i,j}$ of an image on the phosphor of MCP, and hence the entire image. dσ/dΩ can be calculated by the angular distribution formula Eqs. (2.8) and (2.10). The pixel area ΔA on the image plane depends on the image size and the pixel area of the CCD array ΔA_{CCD} = 8.4 μm × 9.8 μm. Because we measure the relative pixel value (relative intensity), we consider ΔA as an adjustable constant when processing data. Therefore it is not necessary to know the area of each pixel for each image. Finally the term

$$\frac{d\Omega}{dA}=\frac{\sin\Theta d\Theta d\Phi}{rdrd\Phi}=\frac{\sin\Theta d\Theta}{rdr}\,,$$

where $\frac{d\Theta}{dr}$ can be expressed as an explicit form by differentiating Eq. (3.3)

$$\begin{aligned}\frac{d\Theta}{dr}=\frac{eV}{2\varepsilon D}&\left(\sqrt{\cos^2\Theta+\frac{eVd}{\varepsilon D}}-\cos\Theta\right)^{-1}\\ &\times\left(\frac{\sin^2\Theta}{\sqrt{\cos^2\Theta+eVd/\varepsilon D}}+\cos\Theta\right)^{-1}.\end{aligned} \tag{3.9}$$

Then we have

$$\frac{d\Omega}{dA}=\frac{\sin\Theta d\Theta d\Phi}{rdrd\Phi}$$
$$=\frac{1}{r}\frac{eV}{2\varepsilon D}\sin\Theta\left(\sqrt{\cos^2\Theta+\frac{eVd}{\varepsilon D}}-\cos\Theta\right)^{-1} \quad (3.10)$$
$$\times\left(\frac{\sin^2\Theta}{\sqrt{\cos^2\Theta+eVd/\varepsilon D}}+\cos\Theta\right)^{-1}.$$

In conclusion, using Eqs. (2.8), (2.10), (3.8), and (3.10), we can calculate the image for any polarization state of the laser based on the experimental and atomic parameters.

We can also determine the radius of the image in the plane of the phosphor screen by differentiating Eq. (3.3) and letting $\frac{dr}{d\Theta}=0$, yielding

$$r_{\max}=\frac{2\varepsilon D\sqrt{1+eVd/\varepsilon D}}{eV}. \quad (3.11)$$

Based on this analysis, we can explain why the Helm's original design failed to work for our measurements. Let's look at an example. From Eq. (3.3), the electrons ejected at an angle Θ and those ejected at an angle π-Θ strike the phosphor screen at different locations r. The distance between these two points is

$$\Delta r=\frac{2\varepsilon D}{eV}\sin 2\Theta. \quad (3.12)$$

In our apparatus, D=1.35 cm and V~ 1 V. For an electron energy ε = 0.25 eV (λ=560 nm) and Θ=45°, Δr=6.8 mm. This is a large separation, easily resolved on

the image. For the detector employed by Helm et al. [52], D =10 cm and V~ 800 V. At ε=0.25 eV and Θ=45° for this detector Δr=0.06 mm. We can clearly see the difference between these two designs. With Helm's apparatus, this distance Δr is about 100 times smaller than that in our experiments. In other words, the separation on the phosphor screen, for the electrons ejected at an initial angle Θ and $\pi-\Theta$, is 100 times smaller for Helm's design. In this design, the electrons ejected from the two directions are actually overlapped on the phosphor screen. This is critical for our measurements, as we must separate the electrons ejected in all directions to preserve the asymmetry of the photoelectron angular distribution created with the elliptically-polarized light in the two-dimensional image on the phosphor screen. Even for the images obtained with linearly-polarized light, we observed the difference between the images obtained by Helm's apparatus and our modified one. As we mentioned in Sec. 3.2, the two images in Fig. 3.3, which were taken with linearly-polarized light oriented at 45° from vertical, show different patterns. Image a) taken with our modified detector shows an asymmetric structure, and the ring is clearly seen; while the image b) taken with the detector similar to Helm's original design (D =5.5 cm, V~ 31 V) look nearly symmetric and the ring disappears, which can be explained as follows. The electrons ejected from the upper lobe of the angular distribution (see Fig. 3.3b) are initially toward the directions around 45° from vertical, but the electrons in the lower portion of the ring eject with the directions around π – 45°. In our detector, these electrons are easily separated, but with Helm's detector geometry, the electrons from these two portions are actually overlapped in the left region of the image. The same argument applies to the right region of the image. This is the reason why the ring disappears and the image is nearly symmetric.

3.4 Acquisition of data

A schematic diagram of the data acquisition system is shown in Fig. 3.6. A photodiode is used to generate a train of electronic pulses (10 Hz) synchronized with the pulsed laser light. A trigger generator converts the pulse sequence into two TTL pulse (5V) trains, which trigger the camera and the video card (Falcon Super VGA Frame Grabber in the PC), respectively. The TM-7AS camera has an electronic shutter with various shutter rates. The benefit of using a camera with a shutter is that this avoids the background caused by the laser light. The width of the pulses and the delay between the two pulse sequences can be adjusted separately. The camera trigger is delayed by 35~40 ms with respect to the frame grabber trigger (i.e. the trigger pulse goes to frame grabber first).

The screen phosphorescence is accumulated on the charge-coupled-device elements of the camera. The video signal is sent to the frame grabber to be converted from the analog to digital form and the data is stored in the Frame Buffer memory. A data acquisition program interfaces to the Falcon frame grabber (video card) via library routines provided by the video card manufacturer. The purpose of the program is to grab an image area from video memory (frame buffer in the Falcon frame grabber) when an external trigger (TTL trigger as shown in Fig. 3.6) is applied to the video card and add the image data to the previously captured images of the same area in video memory. In this way, a composite image of a certain area (180×180 pixels) of the screen can be obtained. The Falcon video card acquires an RS170 standard video signal at 640×480 (pixels) resolution. Once the data acquisition is complete, the summation buffer is normalized to 255. Both the normalized and unnormalized data are saved as ASCII files. The images in Fig. 3.3 are recorded using this mode.

The frame grabber has a Brooktree BT252 analog-to-digital converter, which converts the video signal to 256 voltage levels. A programmable gain and offset is

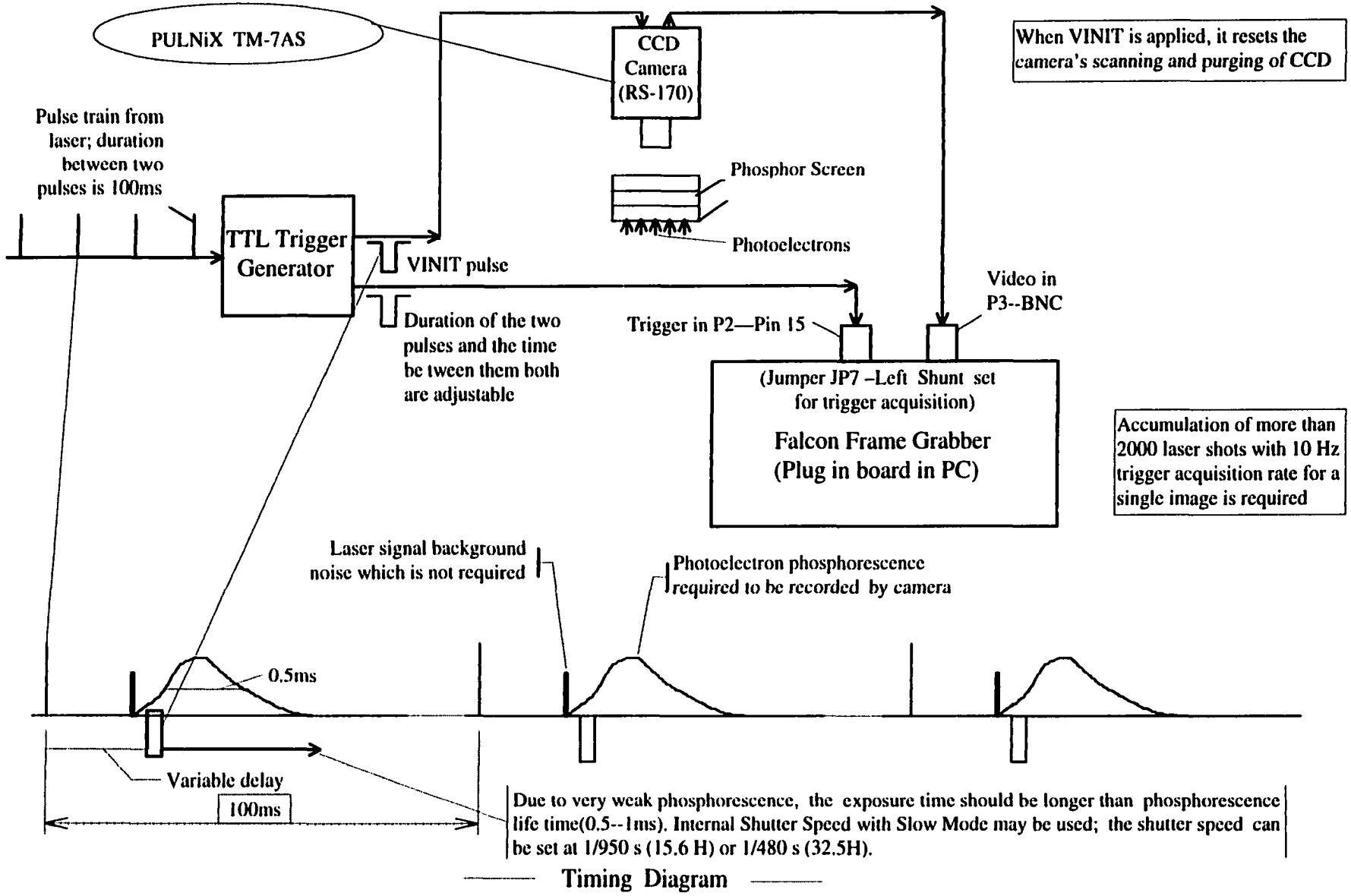

Figure 3.6: Block diagram for data acquisition system

provided with the frame grabber. According to the Falcon Tool Box User's Guide of the frame grabber, "The gain and offset adjustment is provided by setting the lower and upper voltages of the video input. Digitization converts the 256 voltage levels between lower and upper limits into a pixel value from 0 to 255." We used two kinds of settings for the voltage levels. One starts from 0, say 0~80. In this case, a 0 value corresponds to 0 volts; a value of 80 corresponds to 0.375 volts and all other values can be arrived at by linear interpolation. The other setting starts from a non-zero value, say 23~40, which is equivalent to 0.108 V~0.188 V. We call the 0~80 setting the *zero-starting setting* and the 23~40 setting the *non-zero-starting setting*. For both of these settings, the video signal detected by each pixel is a relative value. This value could be influenced not only by the settings mentioned above but also by many other factors. These factors include any non-uniformities of gain of the MCP detector, the phosphor screen, or the CCD array in the camera. In order to decrease the influence of these factors on our images, we use the non-zero-starting setting to take images for data analysis. We will see soon that this setting is better for collecting the data for quantitative analysis.

In order to explain the difference between the two settings we draw two graphs in Fig. 3.7. The horizontal axis represents the voltage setting whose range is 0~255 voltage levels (or 0~1.2V); the vertical axis represents the pixel value from 0~255. For the zero-starting setting, (Fig. 3.7a) the lower limit of the voltage range is 0. In this case all signals, including the background signal, with voltage less than the upper limit V_{upper} are amplified and recorded linearly. (The recorded pixel value is equal to the input voltage level.) For the non-zero-starting setting (Fig. 3.7b), a signal with voltage less than lower limit V_{lower} will be cut off and given a zero pixel value; a signal between the voltage range V_{lower}~V_{upper} is assigned a pixel value that is proportional to the input voltage level minus the lower limit (see Fig. 3.7b). A voltage equal to or greater than the upper limit corresponds to a pixel value of 255 for the both settings. In other words, when the

computer algorithm converts the relative intensity value of each cluster to the number "1", and places the "1" at the pixel closest to the center of the cluster. We call this recording scheme the *threshold detection scheme.*

An example of the raw images on the phosphor screen taken by only a single laser shot is shown in Fig. 3.8. The horizontal axes are the array number of the pixel elements. The vertical axis is the recorded signal intensity of each pixel in the array after subtracting the background image, determined by blocking the atomic beam. The image shown in Fig. 3.8 (a) is collected in a zero-starting setting with the voltage range of the video input setting 0~80. Under this setting, we see that this image still contains a strong background even after subtracting the background image data. The large peaks covering several array elements correspond to the single electrons, while the small peaks are the remaining background noise. The images in Fig. 3.8 (b) and (c) are both recorded with non-zero-starting setting with the lower and upper voltages of the video input being 23 and 40. We see that these images have much less background. But the image in Fig. 3.8 (b) is recorded with linear scheme, and the pixel value is the normalized data. The maximum value is 255; while Fig. 3.8 (c) is taken with the threshold detection scheme. We see that all the pixel values at the central location of each electron cluster are converted to "1". Each peak in these images presents a single electron. In Fig. (c), the sum of the pixel values in each image is actually the number of the electrons. Figs. 3.8 (b) and (c) represent different data sets. We use non-zero-starting setting and threshold detection scheme to take images for data analysis.

The PC is able to analyze the image for each laser pulse, and add the result to the accumulated image in less than 0.1 s, the time between successive laser pulses. We find that this detection scheme is essential for quantitative analysis in our measurements, as the image distortions introduced by the irregularities of the factors mentioned above are eliminated.

In our experiments, we take images at nine different wavelengths and different polarization states of the laser. At each wavelength, we accumulate data over 8000~ 25000 laser pulses for an image. Each image consists of approximately 10^5 electrons with approximately 10~20 electrons for every laser pulse to avoid overlap of the electrons and space charge effects, which could affect the parabolic trajectory of the photoelectrons as they travel toward the upper mesh plate.

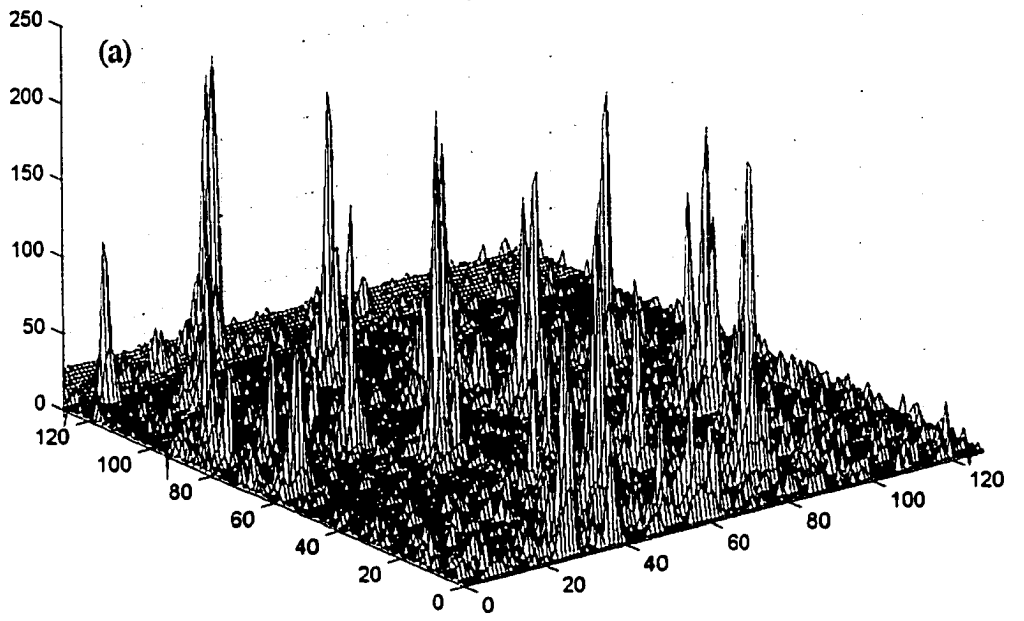

Figure 3.8: (a) Raw image taken by a single laser shot. The horizontal axes indicate the number of pixel elements (128×128). The vertical axis is the brightness of each pixel. This single shot image is recorded using the zero-starting setting with the voltage range of the video input setting 0~80, which is obtained by subtracting the background image data from the row image data. It is clearly seen that the image still has a strong background and each peak contains several bright pixel elements.

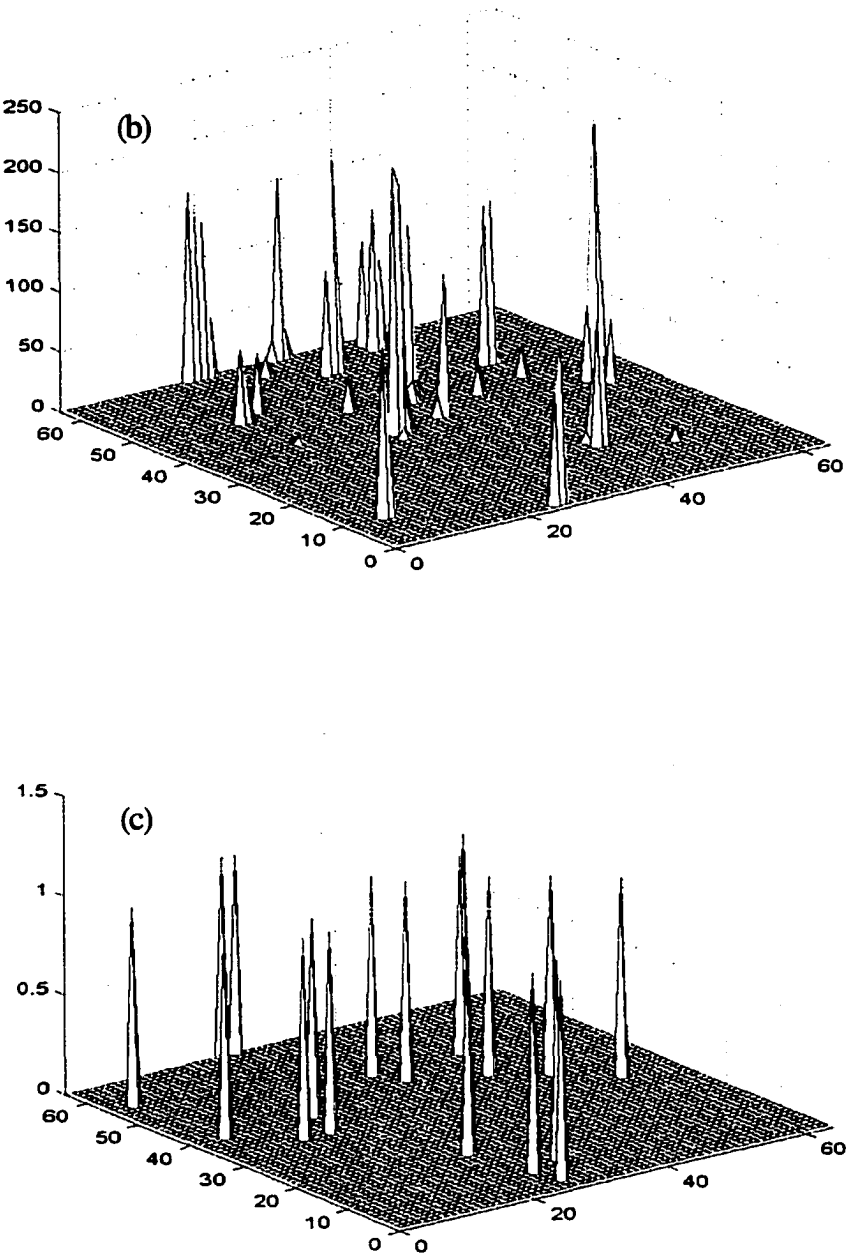

Figure 3.8 (continued): (b) and (c): Raw images taken on a single laser shot (different data) with the non-zero-starting setting (the voltage range of the video input is 23/40). The horizontal axes indicate the number of pixel elements (64×64). The vertical axis is the brightness of each pixel. Each peak represents a single electron. In Fig. (b), the data are taken with linear scheme. It is clearly seen that each peak contains several bright pixels and the peaks have different heights. In Fig. (c), the data are taken with threshold setting all the pixel values at the center location of each electron are converted to 1, so that the height for all peaks is 1 and each peak contains only one pixel.

3.5 Sample images taken with various polarizations of the laser light

Now we show some examples of photoelectron images taken by laser light with different polarization states in Fig. 3.9. For all the images, the laser beam propagates in the $\hat{y}$ direction [refer to the coordinate frame in Fig. 3.9 (c)]. These images are produced by the electrons with the angular distributions shown in Fig. 2.11. For the three images produced with linearly-polarized light in Figs. 3.9 (a) ~ (c), the two bright areas, labeled M_u and M_l, on the figures corresponding to the two lobes in the angular distribution along the direction of polarization, and the ring are clearly seen. With the vertically-polarized light (Fig. 3.9a), the upper lobe of the angular distribution is projected upward, the lower lobe is downward. The electrons from the two lobes are projected onto the image screen directly above the interaction region and created the central bright spot. The electrons comprising the ring around the axis initially travel outward within a small angle with the horizontal plane. Due to the uniform dc electric field, they project onto the image plane to form a perfectly circular ring. With the laser polarization still linear, but rotated 45°, the two bright areas separate, as seen in Fig. 3.9 (b). The maximum (M_u) corresponding to upper lobe is shifted slightly to the left. The electrons in the lower lobe initially travel down and to the right in the uniform field, but have more time to spread out before reaching the image plane, forming a more diffuse area (M_l). In this case, the ring is not perfectly circular, but still clearly visible. The final sample image for linear polarization is shown in Fig. 3.9 (c), corresponding to horizontal polarization. In this case the two lobes form two bright areas on the left and right symmetrically, while the ring forms a single band across the center of the image.

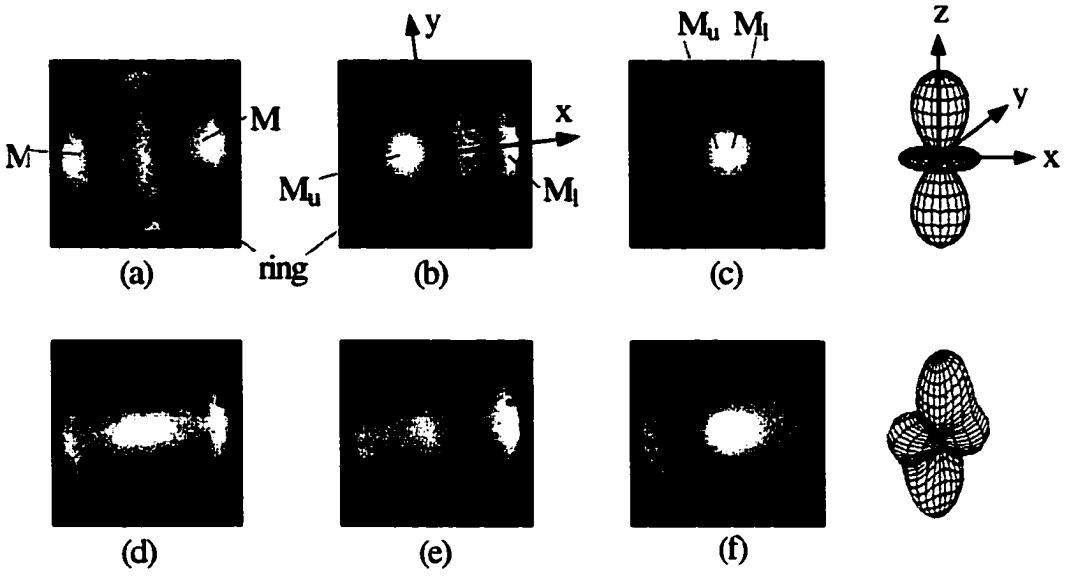

Figure 3.9: Several examples of images on the phosphor screen of MCP assembly created with different polarizations of light. The polarizations are (a) linear, horizontal, (b) linear, –45° from vertical, (c) linear, vertical, (d) circular, (e) left-elliptical, major axis horizontal, and (f) left-elliptical, major axis vertical. (The dark point in the lower right region of each image is a damaged spot on the phosphor screen.)

The images created by elliptically-polarized light are more complicated. They are characterized by the asymmetric distribution that might be understood from the angular distributions shown in Fig. 2.11 (b). The major axis of the ellipse is vertical for Fig. 3.9(d) and horizontal for Fig. 3.9(e). The dark band on the image resulted from the local minimum in the upper side of the distribution. The image in Fig. 3.9(f) generated by circularly-polarized light has a single bright band with two black areas located on both sides symmetrically. The image might be understood by the doughnut-shaped angular distribution in Fig. 2.11(c).

These images were taken using the linear detection scheme with zero-starting setting. In this image, we simply sum the images by adding the pixel value over a large number of laser pulses. When the zero-starting setting was used, there was a strong background as mentioned earlier. We measured the background image by blocking the atomic beam immediately after taking the image. In order to show the images, we subtract the background data from the raw image data. It is clearly seen that, in Fig. 3.8a), the image still has non-negligible background because the zero-starting setting makes the measurement more sensitive than non-zero-starting setting to collect the background noise and to record non-uniformities in the detector or CCD array. And this is a linear detection scheme. With this scheme, we find a 10% variation from one side of the image to the other. This problem will make the data impossible to fit well with a theoretical image because the linear detection scheme records the non-uniformities of the phosphor screen or CCD array. Therefore, the image does not reflect the right angular distribution of photoelectrons. Indeed, the images in this figure could not be fitted well by any of our theoretical images, although they appear to be reasonable qualitatively. The benefit for the threshold detection scheme is that it eliminates the non-uniformities. In other words, for threshold detection scheme, the pixel value is "1" for each single photoelectron. This character makes the same value anywhere on

the image, regardless of how the gain of the detector may vary across the image. This is the major reason to use the threshold detection scheme.

On the other hand, in each of the images shown in Figs. 3.8a) and 3.8b), which are recorded by linear detection scheme, the pixel values are not normalized to "1". As we have mentioned earlier, each bright cluster peak indicates a single electron. A single laser shot creates a number of clusters with different heights. Therefore after accumulating the data with thousands of laser shots, the summation of image pixel value in a specific area may not indicate the number of electrons located in this area, even though collecting data with thousands of laser shots may reduce the influence statistically.

For quantitative analysis, the image has to be taken by the threshold detection scheme with each pixel value normalized to "1" (see Fig. 3.9c) for each single laser shot as stated in the previous section. In order to obtain the atomic parameters from the measured image, we then create a calculated image based on the parabolic trajectory of the photoelectrons from the interaction region to the phosphor screen as we have described in Sec. 3.3.

We will show some of the images taken by threshold detection scheme and describe the details for deriving the atomic parameters based on these images in Chapter 5.

CHAPTER 4
EXPERIMENTAL SET-UP

In this chapter, we describe the details of the experimental apparatus, including the laser system, the vacuum system, the generation of the atomic beam and the influence of the earth's magnetic field on the trajectories of photoelectrons and its cancellation. We use this equipment for our complete measurements of two-photon ionization in rubidium atom, as well as the experiments of quantum interference with two-color laser fields.

4.1 The laser system

The dye laser system used in the experiment consists of a tunable oscillator and three stages of amplification, pumped by the output (532 nm) of a frequency-doubled Nd:YAG (neodymium-doped yttrium aluminum garnet) laser (Laser Photonics). The dye laser oscillator is of the Littman design [51], a short-cavity, longitudinally pumped configuration. It consists of an end mirror, a dye cell, a diffraction grating (2400g/mm), and a tuning mirror. The laser cavity is very short, only ~5 cm long. A small portion (~3%) of the 532 nm laser beam is split off from the main beam and is focused to 0.2~0.3 mm at the center of the 2-mm path length dye cell using a 450 mm focal length lens. The pump pulse energy was kept below 1mJ/pulse to prevent damage to the dye cell and to provide stable operation of the oscillator. The laser output is derived from the zeroth-order reflection of the diffraction grating. With this short cavity, longitudinally-pumped dye laser

oscillator, the output is measured to be 1-3 longitudinal modes in a nearly-lowest-order Gaussian transverse mode.

The amplifiers are longitudinally pumped in a 0.75 in. diameter aperture, 0.25 in. thick, Brewster-angled, laminar flow dye cells. We use two dye cells for the first and second stage of amplification, respectively. A temporal delay of about 4 ns between pumping the oscillator and the first amplifier compensates for the build-up time of the laser pulse in the oscillator and reduces the loss of fluorescence in the amplifier. The delay between pumping the adjacent two amplifiers is about 2 ns.

Three mixtures of dyes were used in the experiments to cover the range of the wavelengths from 540 nm to 590 nm at eight different wavelengths. Fluorescein 548 in methanol + base (NaOH 200 mg/l) at the concentration of 1.6×10^{-3} M (642 mg/l) and 8.7×10^{-4} M (349 mg/l) was used for oscillator and amplifiers, respectively, with maximum lasing wavelength at 546 nm; Rhodamine 590 (R6G) in methanol was used at the concentration of 1.4×10^{-4} M (76 mg/l) for the oscillator and 5.5×10^{-5} M (30 mg/l) for the amplifiers with maximum lasing wavelength at 560 nm; and Rhodamine 610 in methanol at 1.6×10^{-4}M (85 mg/l) for the oscillator and 7.9×10^{-5} M (43 mg/l) for the amplifiers with maximum lasing wavelength at 582 nm.

The energies of 532 nm pump laser beams and the dye laser output we have used in the experiments are listed in table I.

Table 4.1: Laser energy

Stage of dye laser	Pump energy	Dye laser output
Oscillator	0.4 ~ 0.8 mJ	30 ~ 100 μJ
First stage amplifier	5 ~ 10 mJ	0.5 ~ 1 mJ
Second stage amplifier	15 ~ 25 mJ	2 ~ 5 mJ

4.2 The vacuum system

The vacuum system consists of two chambers, the oven chamber and the interaction chamber. The former contains an oven and nozzle assembly that serves as the rubidium atom source. The interaction chamber contains the Micro Channel Plate (MCP) detector assembly and the pair of field plates that we have described earlier.

A high vacuum environment is a critical requirement for both chambers, especially when UV light is used in the interaction chamber since the ionization of residual gas by the UV light can influence the measurements of the electron angular distributions. Each vacuum chamber has an ion gauge to measure the pressure separately. We pre-evacuate the entire system to a pressure of ~10^{-2}-10^{-3} Torr using a mechanical pump. Then we further pump the oven chamber by a diffusion pump with a liquid nitrogen cryotrap to reach a pressure of ~ 2×10^{-8} Torr when the oven is cool and ~2×10^{-7} Torr when the oven is at the operating temperature. Liquid nitrogen is filled into the cryotrap from a 60 liter dewar automatically by a controller. The interaction chamber is pumped by a 6-in. cryopump (CSA-102, pump speed: 1500 liter/sec), which reduces the vacuum pressure of the interaction chamber to 2~3 $\times10^{-8}$ Torr. The pressure is maintained at this level during the entire period of taking data. Using a cryopump prevents oil contamination inside the chamber. When using a diffusion pump, thin oil coatings can cause a stray static electric field that may affect the results of the measurements. Also the micro-channel plate requires a dry-pumped clean environment. According to the manual, "A poor vacuum environment will most likely shorten MCP life or change its operating characteristics."

The two chambers are separated by a stainless steel plate with a 4 mm diameter hole at the center. The small hole allows only a fraction of the rubidium atoms to pass through into the interaction chamber, helping reduce the background

noise. It also helps to maintain a steady high-vacuum pressure in the interaction chamber as the pressure in the oven side increases due to the release of gas from the heating elements of the oven.

We also have a small turbo molecular pump (Turbo-V80, pump speed: 75 liter/sec) installed on the interaction chamber. The opening for the turbo pump on the chamber is directly in line with the atomic beam. It helps evacuate the rubidium atom beam after the atoms pass the interaction region. The atomic beam could reflect from the wall of the chamber, resulting in background noise if a turbo molecular pump were not installed, especially when the oven is first turned on and is still approaching the required stable operating temperature. Since the pumping speed of the turbo pump is relatively low, and its mechanical failure during the course of our experiments could cause the entire vacuum system to vent to atmosphere (which may damage the MCP even though we have an automatic shut off circuit for the high voltage to the MCP), we operated this pump only during the oven warming period before we started taking data.

Fig. 4.1 shows the vacuum system, and other equipment.

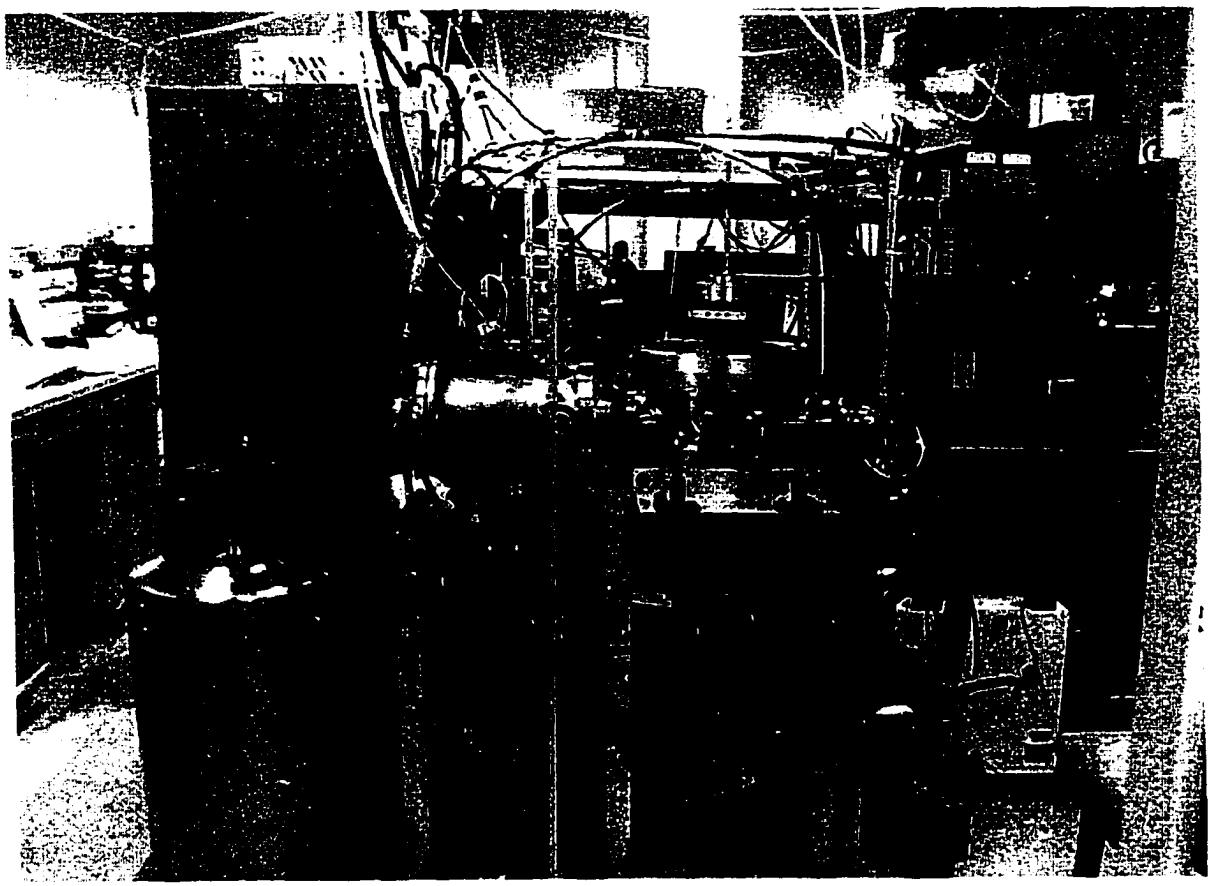

Figure 4.1: The vacuum system and other equipment

4.3 Generation of the atomic beam

The effusive atomic beam is generated in a two-stage oven, as shown in Fig. 4.2. The oven is made of stainless steel and consists of two parts: a reservoir for the rubidium metal and a nozzle. The cylindrical reservoir and the nozzle body both have four holes parallel to the axis of the cylinders into which we insert the heating elements made of Nichrome wires with ceramic insulators. The two parts of the oven are heated separately and each has a thermocouple [ANSI letter K, Chromel(+) ---Alumel(-)] to measure the temperature. The oven is maintained at a body temperature of 145° C. The nozzle, with an aperture diameter of 0.9 mm, is held at a slightly elevated temperature to discourage rubidium condensation and dimer formation. The oven produces an atomic beam density of 3×10^7 cm $^{-3}$ at the interaction region, a distance of ~37 cm from the oven nozzle (see Fig. 4.3 for the configuration of the apertures). There are two apertures located in the interaction chamber to reduce the size of the atomic beam. The first aperture is 15 cm from the interaction region with a diameter of d_3=0.5 mm; the second one is a beam stopper, which is 2.5 cm from the first one, with a diameter of d_4=1 mm. The beam stopper has a box-like metal cover to prevent the reflected atoms from the stopper entering the interaction region and causing serious background noise that masks the image. This is extremely important for obtaining clear electron images. The nozzle and the two apertures select the atoms in a nearly collimated atomic beam. The effective beam diameter was measured to be ~ 1 mm by moving the laser beam up and down and observing the change in the intensity of the image.

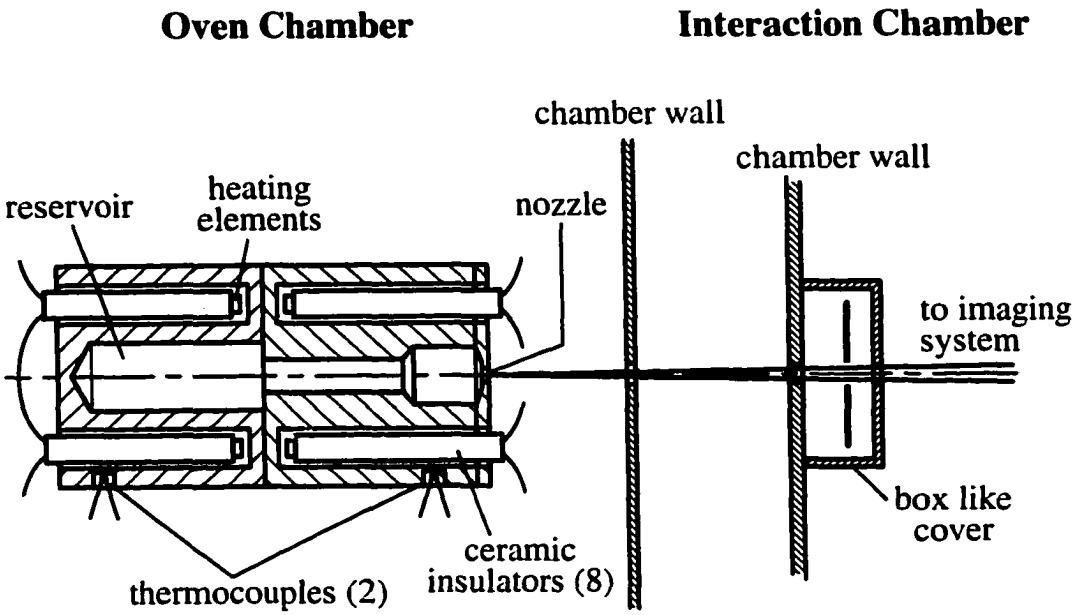

Figure 4.2: The oven and atomic beam apertures

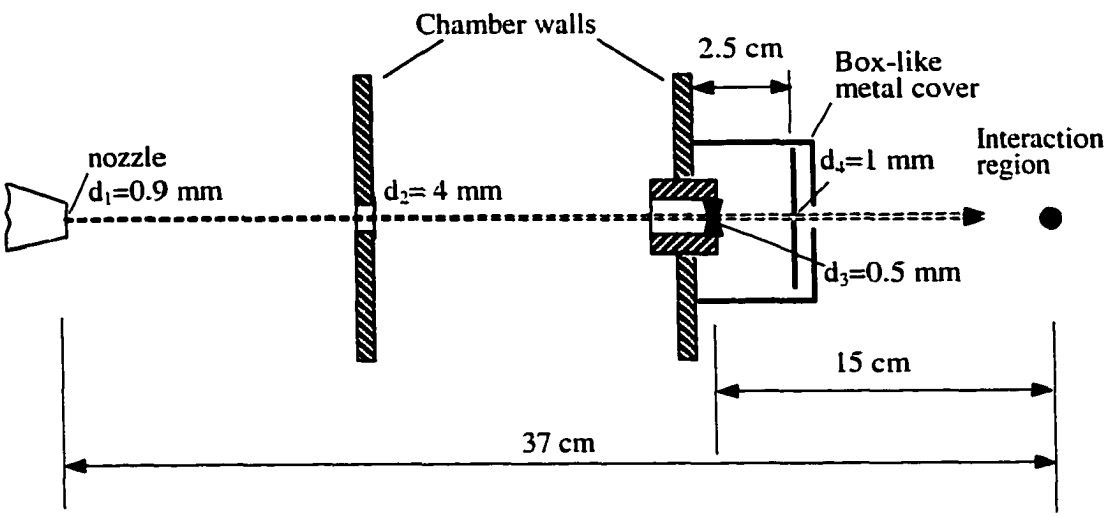

Figure 4.3: The apertures for collimating atomic beam

4.4 The influence of the earth's magnetic field on the trajectories of photoelectrons and its cancellation

The earth's magnetic field will affect the trajectories of the photoelectrons moving towards the MCP and hence distort the photoelectron images. We therefore have to reduce the influence of the earth's magnetic field. We can estimate the minimum radius of the curvature of the electrons moving around the interaction region due to the magnetic field. Comparing this radius with the dimension of the space where the photoelectrons move around, we can see that the influence of the earth's magnetic field cannot be ignored.

The force an electron experiences in a magnetic field $\vec{B}$ is

$$\vec{F} = e\bar{v} \times \vec{B}$$

and the force causing the electron to move in a circular orbit of radius R is

$$F = \frac{mv^2}{R}$$

where e is the electron charge and $\bar{v}$ is the velocity of the electron, and m is the mass of the electron.

For the minimum radius of the motion of the electron in the field, the velocity is perpendicular to the field, i.e. $F=evB$. In this estimate calculation, we only need to consider the initial velocity of the electron ejected in the interaction region. Setting

$$\frac{mv^2}{R} = evB,$$

we get the minimum radius of the motion

$$R = \frac{mv}{eB} \tag{4.1}$$

Replacing v with the expression in terms of the electron energy ε

$$v = \sqrt{\frac{2\varepsilon}{m}} \tag{4.2}$$

and combining Eq. (4.1) and Eq. (4.2), we have

$$R = \frac{\sqrt{2m\varepsilon}}{eB}. \tag{4.3}$$

In our experiments, the minimum initial kinetic energy (corresponding to the longest wavelength of the laser beam, 590 nm) of the photoelectron is 25.70 meV or 0.041×10^{-19} J. The earth's magnetic field is ~0.5 Gauss. According to Eq. (4.3), the minimum radius of the curvature is ~ 1 cm. This radius is comparable with the distance between the interaction region and the upper mesh of our detector system, 0.55 cm (see Sec. 3.2). It is clearly seen that the earth magnetic field cannot be ignored when taking data.

In order to reduce the influence of the earth's magnetic field on the motion of the electrons in the interaction region and the surrounding area, we installed three orthogonal pairs of magnetic coils with diameter of 90 cm around the vacuum system (see Fig. 4.1). The currents in the three pairs of coils can be adjusted separately to assure that the earth's magnetic field in the interaction region and the surrounding space is less than 10 mG in three directions (vertical and two horizontal). From Eq. (4.3), the minimum radius is 54 cm at this field level. This minimum radius is much larger than the dimension of the space where the electrons travel from the interaction region to the upper dc field mesh plate. The effect of the field at this level on the image is negligible. We observed the effect of the earth's field on our images. When the current of the coils was turned off, the image was distorted and shifted. When the current was turned on, the image was back to normal.

4.5 Summary

In this chapter we have described the laser system, the vacuum system and the generation of the atomic beam. We use these systems for both the complete measurements of two-photon ionization in atomic rubidium and the quantum interference experiments with two-color laser fields. We also discussed the influence and cancellation of the earth's magnetic field, which is important for obtaining undistorted image data.

CHAPTER 5

COMPLETE MEASUREMENTS OF TWO-PHOTON IONIZATION IN ATOMIC RUBIDIUM

In this chapter, we describe the details of our complete measurements of two-photon ionization of atomic rubidium, including the experiment, results and discussions. The present work is motivated largely through questions raised in the previous incomplete measurements [50] in our group stated in Chapter 2 and Appendix A. These measurements implied that either 1) the relative cross sections for ionization into the continuum $^2D_{5/2}$ and $^2D_{3/2}$ channels were highly unbalanced; or 2) the continuum channel phase differences were in strong disagreement with expected values. The present work is to further this study.

5.1 Background and basic concept

In the past thirty years, a common feature of research in the area of atomic photo-ionization has been the effort toward "complete" measurements. Such an experiment was defined to yield the complete set of atomic parameters describing the process under consideration. These parameters include the relative photo-ionization cross sections between the channels in the multi-photon ionization process, as well as the phase differences between the continuum waves.

Various techniques for complete measurements of photoionization processes have been reported in the past. Most complete determinations have included a measurement of the photoelectron angular distribution using linearly-polarized light. For these measurements, additional information or experimental data are

required to supplement the measurements for the complete determination, since the single measurement of PAD is insufficient to completely characterize the interaction. The measurements of spin polarization and angular distribution complement each other to form a complete determination of the photoionization process. For example, Kaminski et al [20] carried out these experiments in cesium. They measured the angular distribution and spin polarization of photoelectrons produced by linearly-polarized light from the $7^2P_{1/2}$ excited state of Cs. Combination with earlier cross-section data from others allowed them to perform a complete determination. Such studies of spin polarization give information on details of the photoionization process (for a review, see Kessler 1985 [58], for example). However, the low efficiency of the Mott detector used in the spin polarization experiment makes the measurements difficult. The most recent reports of complete measurements make use of circular-dichroism effects on photoelectron angular distributions [59, 60]. Circular-dichroism is a phenomenon where the response of the system to right- and left-circularly polarized light is different. In these experiments, linearly-polarized light was used to excite and align the atoms or molecules and alternately right- and left-circular light to ionize them. In addition to the requirement of multiple measurements in all the previous experiments, they typically yield only the cosine of the phase difference of continuum waves, rather than the phase difference directly as we have mentioned earlier.

A "complete" measurement of a physical process represents an optimum knowledge of physics extracted from the experiment. Let us now discuss the measurements necessary for that purpose in photoionization. It can easily be seen that, as a result of the selection rules for dipole radiation for two-photon ionization of alkali atoms in the ground S state, the ionization occurs to continuum S and D states via a virtual intermediate P state. The process involves five ionization

pathways that can be expressed by five radial transition matrix elements. Since there are three final continuum states $\varepsilon^2S_{1/2}$, $\varepsilon^2D_{3/2}$, $\varepsilon^2D_{5/2}$, the three outgoing channels can be described by the three reduced two-photon transition moments, $S_r = |S_r|e^{i\phi_r}$ with r= s, $d_{3/2}$, $d_{5/2}$. There are thus six independent parameters, three moduli and three phases. The three moduli express the three cross sections σ_s, $\sigma_{3/2}$ and $\sigma_{5/2}$.

Unlike the angular parts of the continuum function, which are determined by spherical harmonics, the radial parts are not well known. Since only the phase differences between the partial waves are relevant, one of the phases can be chosen arbitrarily. For the two D fine structure channels, we estimate, using bound state energy levels [54], that the magnitude of the phase difference is only 0.003π. As we show later in this thesis, this estimated phase difference is smaller than the uncertainty in our measurements of $\Delta\xi=\xi_s-\xi_d$, and we therefore neglect any phase difference between these two continuum D channels. In this case, the relative photoionization cross sections σ_s/σ_d and $\sigma_{5/2}/\sigma_{3/2}$ and the relative phase difference $\Delta\xi=\xi_s-\xi_d$ are sufficient to describe the photoionization process. Also, a complete description must include the sign of the relative phase shift. Our technique has performed the complete measurements of two-photon ionization of rubidium successfully.

5.2 Experiment

In this section, we discuss our experiments on two-photon ionization of atomic rubidium. We choose atomic rubidium in our studies because alkali metals have the advantages of relatively easy preparation in the form of an atomic beam, low ionization potentials, and the simplicity of the alkali energy level scheme. The last of these is critical for the theoretical understanding and interpretation of the results. The isotopic abundance of ^{85}Rb and ^{87}Rb is 72% and 28%, respectively.

The purity of rubidium used in our experiments was 99.8%. The experimental apparatus employed in the present study consists of a pulsed dye laser system, the vacuum system and data acquisition system, which we have described in chapter 3. In this section, we first describe the optical system for this measurement and discuss the polarization characteristics of the laser fields, which are quite important for our measurements and data analysis. Then we present the experimental procedure, results and discussions.

5.2.1 Optical system

The optical system is shown schematically in Fig. 5.1. The laser beam first passes through a half-wave Fresnel rhomb, which rotates the polarization direction of the light. The light polarization is rotated by twice the rotation angle of the Fresnel rhomb. The linearly-polarized light then is further purified by a high quality Glan air prism polarizer which is rotated by an angle accordingly to match the polarization of light. The polarization is linear to better than one part in a thousand. A quarter-wave Fresnel rhomb is used to convert the linearly-polarized light into elliptically-polarized light. The angle between the polarization direction and the incident plane of the incoming laser light on the $\lambda/4$ rhomb determines the ellipticity of the ellipse. When the angle is 45°, circularly-polarized light emerges from the quarter-wave rhomb. A second half-wave Fresnel rhomb is used to rotate the elliptically-polarized light.

We determine the wavelength of the light using a quarter-meter monochromator, calibrated with a He-Ne laser at 632.8 nm and the 532.0 nm harmonic output of the Nd:YAG laser. We also carry out our photoionization measurements with the 532 nm harmonic light directly in our experiments.

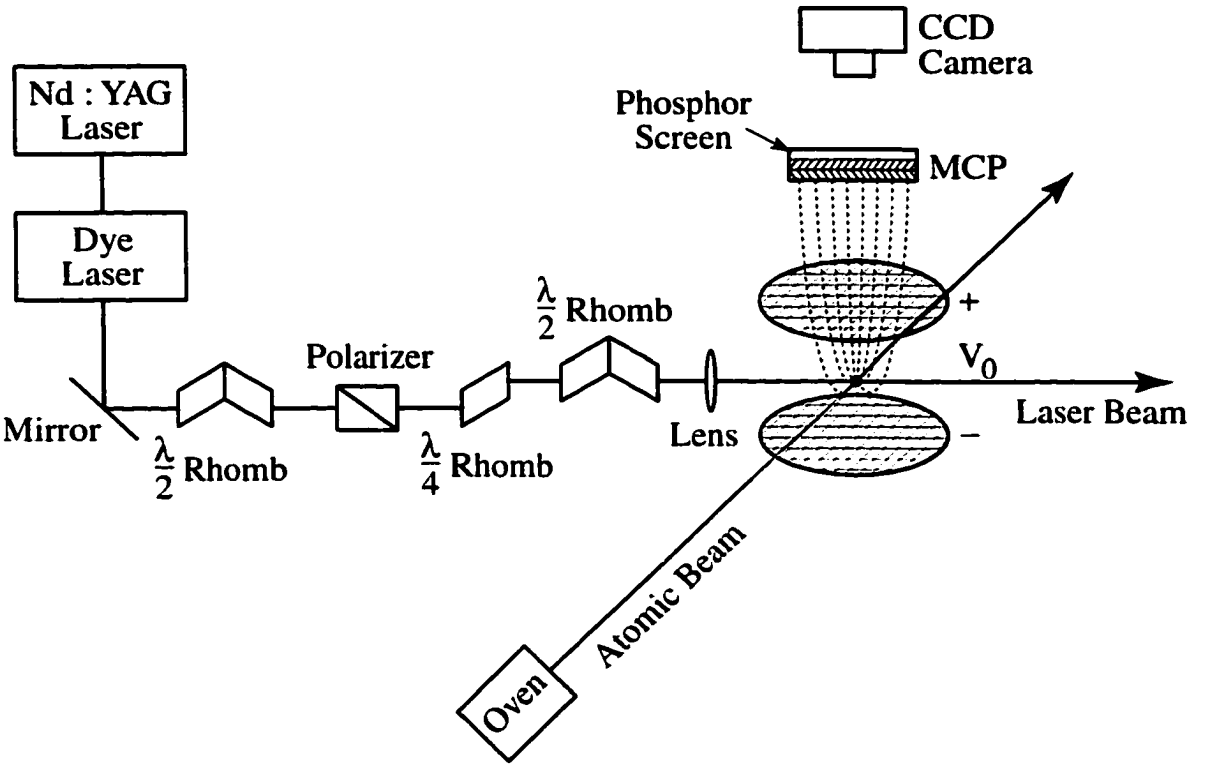

Figure 5.1: The optical system and imaging system.

5.2.2 Analysis of the polarization of laser fields

Now we discuss the details of the polarizations of the laser fields. The polarization of the optical field is critical for these measurements. We control the polarization using the optical components shown in Fig. 5.1. We employ different polarization states and various wavelengths of light to obtain the electron images. For data analysis we only select two light polarization states in the experiments. For linearly-polarized light, the direction of the polarization is set to 45° from vertical. For elliptically-polarized light, the major axis of the ellipse is set to be horizontal. It is generated by rotating the first λ/2 Fresnel rhomb by 11.25°and the polarizer by 22.5°, both in the clockwise direction. (We describe all rotations as viewed by an observer looking into the laser source. In this analysis, the laser beam propagates in the $+\hat{y}$ direction.) The λ/4 rhomb, oriented vertically as shown in the figure, converts the linearly-polarized light to right-elliptically-polarized light with the major axis vertical. The second λ/2 rhomb at 45° from vertical then rotates the ellipse 90°, making its major axis in the horizontal direction.

The sense of rotation of the elliptical light can be determined by the phase shifts of the S- and P-polarized components resulting from the two total internal reflections in the λ/4 Fresnel rhomb. Born and Wolf showed [60] that the P-polarized (vertical) component is advanced relative to the S-polarized (horizontal) component. From this argument, light entering the λ/4 rhomb in the linear polarization state $\hat{\epsilon}=\sin 22.5^\circ \hat{x}-\cos 22.5^\circ \hat{z}$ will emerge from the rhomb as right elliptically-polarized light, $\hat{\epsilon}= -i\sin 22.5^\circ \hat{x}+\cos 22.5^\circ \hat{z}$, with the major axis vertical from the rhomb. This polarization has been mentioned in Sec. 3.4, $\hat{\epsilon}=-i\epsilon_1'' \hat{x}+\epsilon_3' \hat{z}$. These two polarization states can be illustrated by Lissajous figures as below.

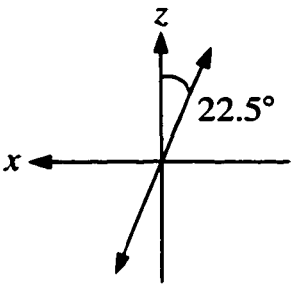

Laser beam along ⊙

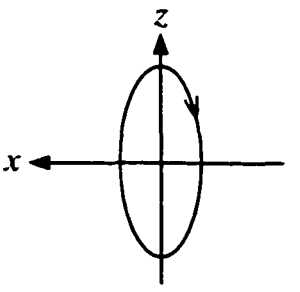

The linear light entering the λ/4 Fresnel rhomb

The elliptical light emerging from the λ/4 Fresnel rhomb

Referring to the definition of the field Eq. 2.9, we can write the two components of the complex amplitude of the field.

$$\tilde{E}_x = \epsilon''_1 e^{-i(\omega t+\frac{\pi}{2})}$$
$$\tilde{E}_z = \epsilon'_3 e^{-i\omega t}.$$

Taking their real parts

$$E_x = \epsilon''_1 \cos(\omega t + \frac{\pi}{2})$$
$$E_z = \epsilon'_3 \cos\omega t,$$

we immediately see that the field rotates in the clockwise direction or that it is right-elliptically-polarized light.

The second λ/2 Fresnel rhomb, which is set at 45° from the vertical, rotates the ellipse by 90°and reverses the rotation sense. The major axis of the elliptical polarization is thus horizontal, and the sense of the rotation is left-handed, $\hat{\epsilon} = i\cos 22.5°\,\hat{x} + \sin 22.5°\,\hat{z} = i|\epsilon_1|\,\hat{x} + |\epsilon_3|\,\hat{z}$. Similarly, this polarization state can be illustrated by a Lissajous figure as below.

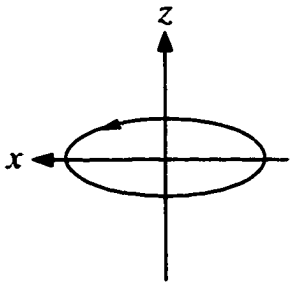

The elliptical light emerging
from the λ/2 Fresnel rhomb

Most of our measurements were carried out using left-elliptically-polarized light. Two sets of data in our experiment taken with right-elliptically-polarized light were obtained by rotating the first λ/2 rhomb and polarizer in the counter-clockwise direction.

We also carried out measurements at each wavelength using linear polarization, oriented at 45° from the vertical. For experimental convenience, we did not move the λ/4 rhomb out of the system. Instead, we rotated the first λ/2 rhomb and the polarizer to the vertical orientation. We also rotated the second λ/2 rhomb 22.5° from vertical in the counter-clock-wise direction to change the polarization direction from vertical to 45°. Similarly, for linear horizontal polarization, we rotated the second λ/2 rhomb to an angle of 45° from vertical. We inserted an additional linear polarizer (not shown in Fig. 5.1) after the final rhomb to improve the polarization purity.

For each of the polarization states, including linear and elliptical light, we confirmed the polarization of the field by measuring the transmission power of the beam through a Glan-laser polarizer. The intensity of the light passing through the polarizer can be expressed as (see Appendix B for the derivation)

$$P_t = P_0(|\varepsilon_1|^2 \sin^2 \vartheta' + |\varepsilon_3|^2 \cos^2 \vartheta') \qquad (5.1)$$

where P_0 is the power of the incident linear light, ϑ' is the polarizer orientation from $\hat{z}$ axis. ε_1 and ε_3 are two components of the unit polarization vector $\hat{\varepsilon} = i\varepsilon_1 \hat{x} + \varepsilon_3 \hat{z}$ of the elliptically-polarized light.

For linear polarization, we set $\vartheta' = 0°$ and $90°$ to measure the polarization of the vertically-polarized incident light. We rotate the analyzer from 0^o to 360^o in 11.25^o increments, and fit the data points of the intensities to Eq. 5.1 to obtain the ratio $\varepsilon_3/\varepsilon_1$. As an example, Fig. 5.2 shows the data points, the best fit curves and the corresponding ellipse for the light at λ = 575 nm. The data in this figure are measured after the second $\lambda/2$ rhomb. The major axis of the ellipse is horizontal. The sense of the elliptical light is not shown in this figure.

This measurement does not yield the sense of the polarization, but it allows us to determine the magnitude of the ellipticity very precisely. We find that the typical rms deviation between the measured transmitted power and the best fit function of the form of Eq. 5.1 is ~1% of the maximum transmitted power. The determination of the polarization is straightforward in principle, but is somewhat complicated in practice because the optical elements are not ideal and the alignment of the optical elements is not perfect. Since these instrumental effects are wavelength dependent, the measurements have to be carried out over the entire wavelength range used to minimize the errors. We measured $\varepsilon_3/\varepsilon_1$ at five different wavelengths between 532 nm and 591 nm, and fitted a linear function to these measurements. The data of $\varepsilon_3/\varepsilon_1$ show a slight variation with wavelength (see Fig. 5.3) which is due to the variation of the phase shift induced upon total internal reflection inside the Fresnel rhombs. We calculate nine interpolated values of ellipticity from the best fitting procedure for the nine wavelengths with which we

take the image data. We use these nine values of ϵ_3/ϵ_1 when fitting the image data to reduce the error of the measurements.

In Appendix C, we present the derivation of the best fitting parameters $|\epsilon_1|$ and $|\epsilon_3|$ of the Eq. (5.1) to experimental data.

5.2.3 Procedure of experiments

After the vertically-polarized light from the second dye laser amplifier goes through the series of optical polarization components (as shown in Fig. 5.1) to obtain the required polarization state, it then enters the interaction chamber. The dye laser beam is weakly focused by a 50 cm focal length lens to a radius of ~0.30 mm (the intensity at this radius is e^{-2} of the maximum intensity) in the interaction region. The radius is determined by measuring the transmission through a 0.254 mm diameter pinhole and assuming a perfect Gaussian beam shape. We estimate the peak laser intensity to be on the order of 0.2 $GWcm^{-2}$ when the laser pulse energy is 2.5 mJ. The interaction volume is estimated to be $\sim 10^{-4}$ cm^3 and there are about 3×10^3 atoms in the region.

After passing through the chamber, the laser beam emerges through a fused silica window oriented 45° from the vertical. The reflection from the window goes into a light trap. This design greatly reduces light scattering in the chamber. Also the window allows a helium-neon laser beam to pass through the chamber from the other side, which makes the optical alignment much easier.

The laser beam interacts with the rubidium atoms to drive the two-photon ionization process, exciting the atoms from the ground $5^2S_{1/2}$ state via the intermediate virtual nP state to the continuum *s*- and *d*-states as shown in Fig. 2.2. As we have described in Chapter 3, the photoelectrons ejected in the interaction

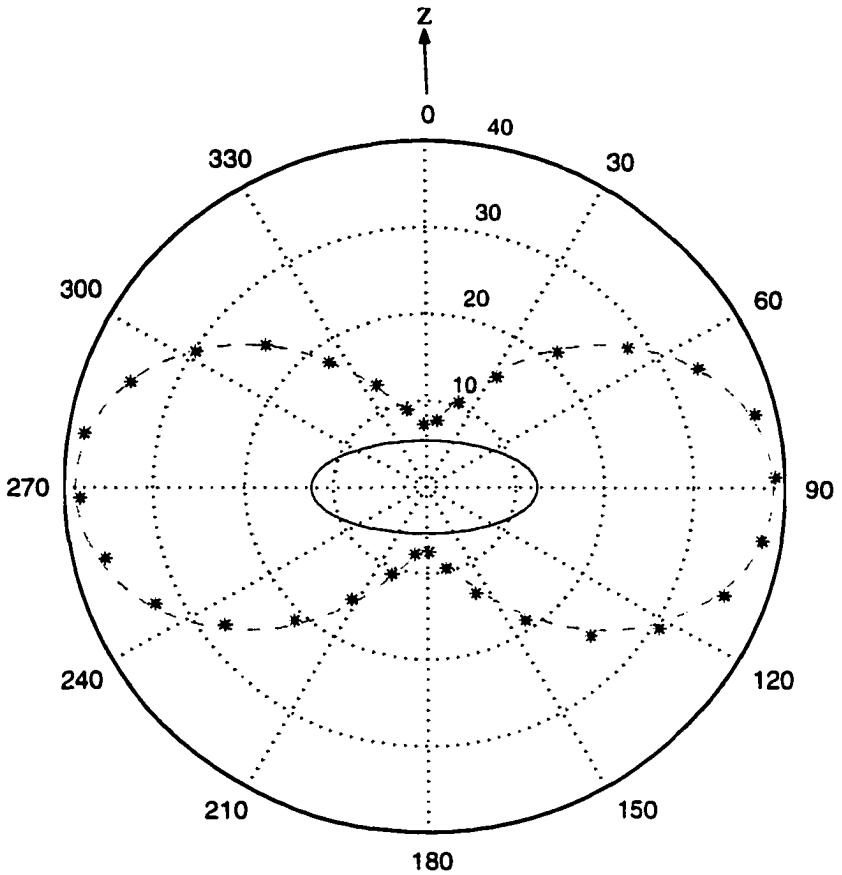

Figure 5.2: Determination of ellipticity of elliptically-polarized light. The stars are the data points of the transmitted power through the polarizer, the dashed line is the best fit of Eq. (5.1) to the data and the solid line is the corresponding ellipse. The data is measured after the second $\lambda/2$ rhomb.

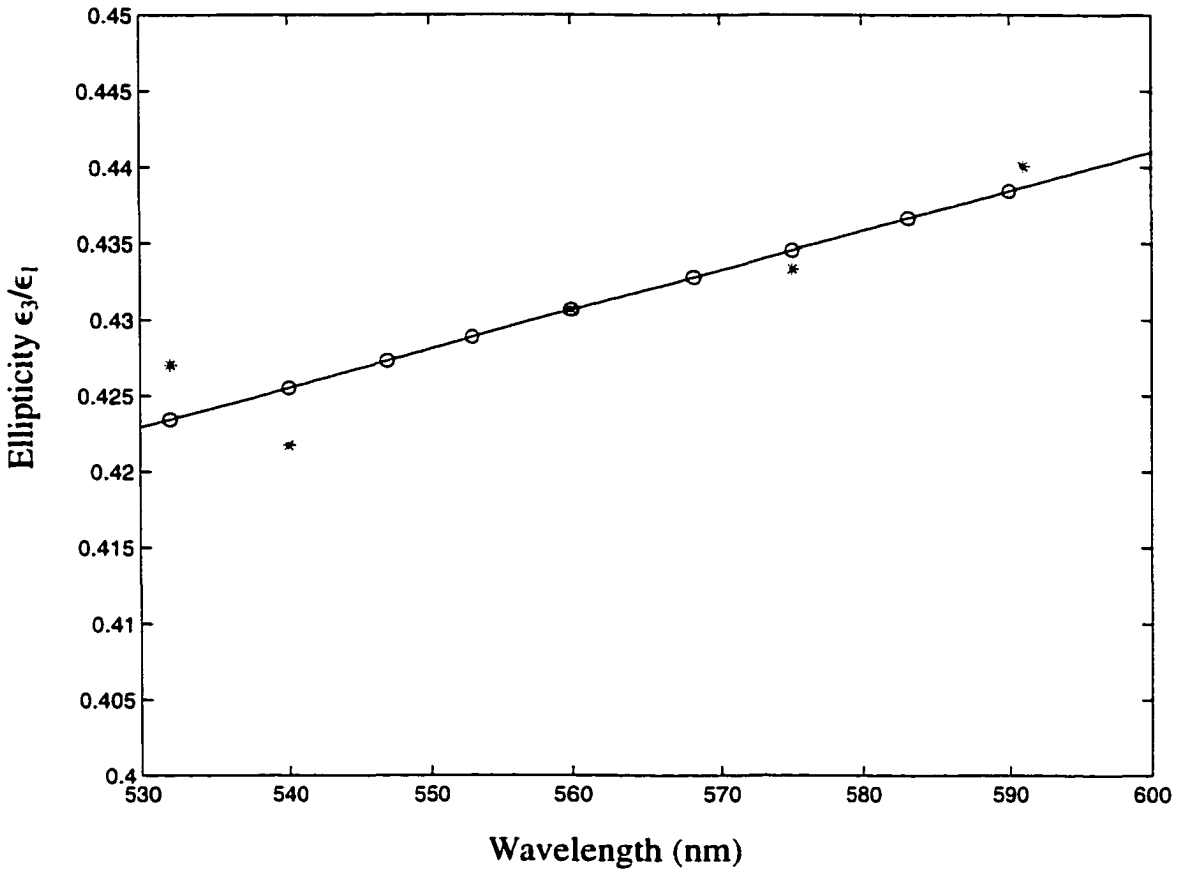

Figure 5.3: Ellipticity verses wavelength. The stars are data points of measured ellipticity for five different wavelengths, the solid line is the best fit to the data and the circles are the interpolated data for nine wavelengths with which we take the image data.

region are accelerated towards the micro-channel plate by the uniform dc electric field (See Fig. 3.1) and form an image on the screen of the MCP assembly. The image size depends on the wavelength of the laser field, the distance from the interaction region to the MCP, and the field strength between the two field plates. We collect an image data by accumulating the images over thousands of laser shots. We take images with various laser polarization states and nine different wavelengths.

5.3 Results and discussions

In this section we first show two images taken with left- and right-elliptically-polarized light at the wavelengths of 540 nm and 583.3 nm, respectively, using threshold detection scheme and describe the details of these images. Then we discuss the procedure for fitting theoretical images to measured images and the details to obtain the atomic parameters. We give our results of the three atomic parameters determined from the fitting process and discuss our results. We also show two examples of images recorded with linearly-polarized light at λ=540 nm and λ=583.3 nm and compare these images with the calculated ones using the atomic parameters obtained from the image data with elliptically polarized light.

5.3.1 Fitting theoretical images to measured images

In this section we first show an example of photoelectron images recorded using the threshold setting with all pixel values at the center of detected photoelectron clusters converted to "1" for each single laser shot. We have already discussed that only images taken with this setting could be used for quantitative analysis. In Fig. 5.4, (a) is the recorded image, which is taken with left-elliptically-polarized laser light at λ=540.0 nm with the ellipticity of the laser polarization $\epsilon_3/\epsilon_1 = -0.426i$. This image is one of the images we have used for extracting the atomic parameters, (b) is the corresponding calculated image. The axes are labeled with the pixel number, 1~128 in the $\hat{y}$ direction and 1~64 in the $\hat{x}$ direction. A full frame for the camera is not available in shutter mode. In this mode the camera only records a field for each laser shot. In other words, the image data for every other column are all zero. We only plot the non-zero data in the image area. Therefore there are only half as many columns of data as rows. The direction of laser propagation is along the y axis in this figure. We see that the image is nearly symmetric with respect to the x axis, but asymmetric to the y axis.

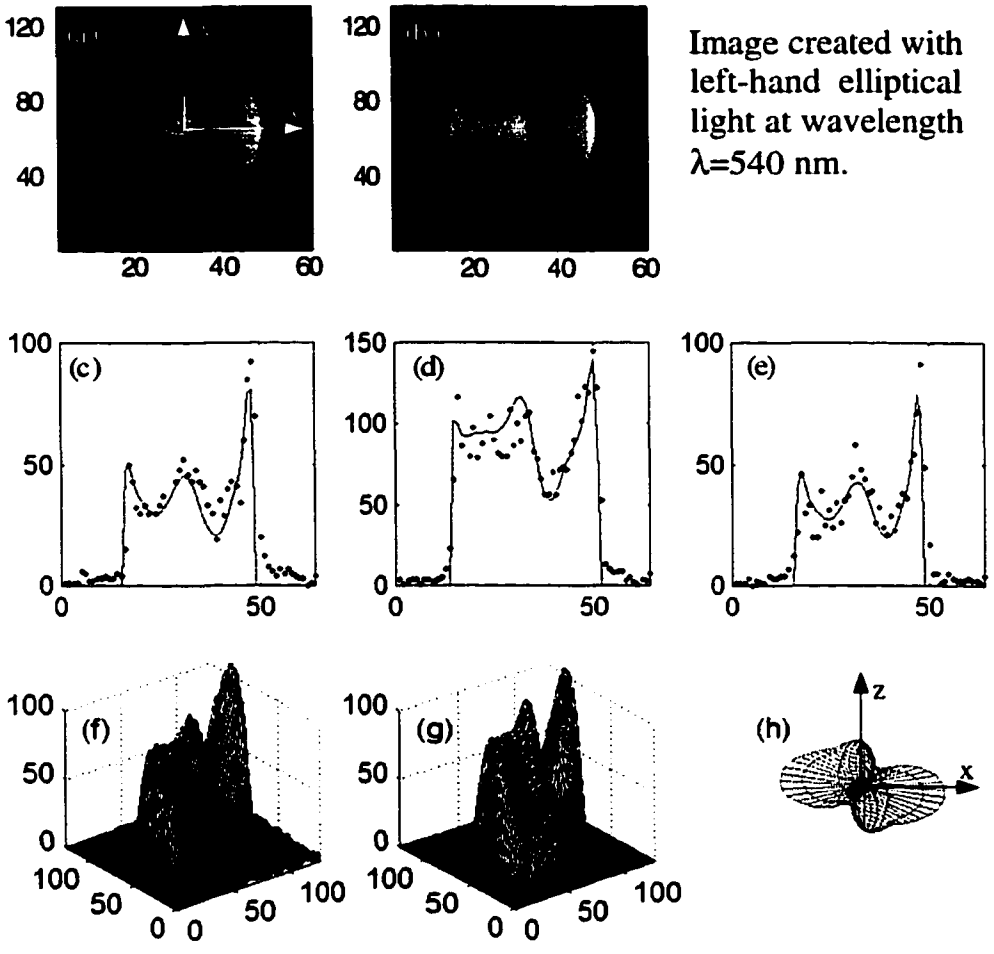

Figure 5.4: Example of an image taken with left-elliptically polarized light. (a) is the measured image, (b) is the corresponding calculated image. (c), (d), and (e) are cross-sectional slices for rows 45, 65 and 85, respectively, showing the data points and the best fitting curve. (f) and (g) are mesh plots for images (a) and (b), respectively, and the calculated angular distribution that produces this image is shown in Fig. (h).

This is because photoelectron angular distributions (see Fig. (h)) are symmetric with respect to the x-z plane, but asymmetric to the y-z plane. According to the angular distribution, we can also expect that the number of the electrons should be equal, not only in the upper half and lower half regions, but also in the left and right half portions of the image. Indeed, we sum the pixel values in each half plane and find that the number of the electrons in each half plane matches the number of electrons in the other plane within 2% in all the images we have taken for quantitative analysis. In Fig. (f) and (g), we plot the three-dimensional images (mesh plot) that correspond to Fig. (a) and (b), respectively. The labels on the vertical axes in these mesh plots indicate the number of the electrons. In fig. (f), the recorded image, we take the average of the adjacent non-zero data columns and insert the average value into the zero-value column. Then we take the average of the adjacent three columns and insert the average values into the central one of the three columns. This smoothing process helps the figure to illustrate the image clearly without losing its reality. The number of pixels in this plot is 128×128. We see that Figs. (f) and (g) look very similar. It should be pointed out that we do not smooth the raw data shown in Fig. (a) for data analysis in order to extract the atomic parameters correctly.

The image size is determined by the distance d between the interaction region and the top mesh, the spacing D and the dc voltage V_{dc} between the two mesh plates, and the laser wavelength, which determines the kinetic energy of the electrons. The image size increases with decreasing laser wavelength. The geometric parameters D and d are fixed when taking data. We control the image size by adjusting the dc voltage V_{dc} that provides the uniform dc field. The image diameter is typically controlled to ~1.5 cm (see table 5.1), which is much greater than the size of the interaction region, but much smaller than the size of the plane meshes. If the image is too small, the electrons will overlap on the phosphor screen of the MCP and it will decrease the resolution of the image. Also averaging

screen of the MCP and it will decrease the resolution of the image. Also averaging over the interaction volume will smooth the peaks and the valleys. Conversely, if the image is too large, the non-uniformities of the phosphor screen, the CCD array and the electric field (edge effect) may distort the images.

In order to obtain the atomic parameters from a measured image using elliptically-polarized light, we have to create a calculated image by using the experimental parameters, i.e. the distance d between the top mesh and the interaction region, the distance D between the two meshes, the voltage V applied between the meshes, a parameter that represents the size of the interaction region, and a scaling factor between the image size and the size of the phosphor screen. To do this, it is necessary to calculate the angular distribution based on the Eqs. (2.8) and (2.10), and map the parabolic trajectory of the photoelectrons from the interaction region to the phosphor screen of the MCP as described in section 3.3. To obtain the smallest root-mean-square (rms) deviation between the theoretical image and the measured image, we define

$$\chi = \sqrt{\frac{\sum_{i=1}^{a}\sum_{j=1}^{b}(I_{ij}^{(c)} - I_{ij}^{(e)})^2}{N}}, \tag{5.2}$$

where $I_{ij}^{(c)}$ is the pixel value of the calculated image at the i^{th} row and the j^{th} column of the image data matrix, $I_{ij}^{(e)}$ is the corresponding pixel value of the measured image, and N is the total number of the pixels of the image. As we have mentioned that the angular distribution depends on the three atomic parameters or equivalently, the three parameters $S_{\bar{s}}/S_{\bar{d}}$, $S_{\Delta d}/S_{\bar{d}}$, and ξ_s - ξ_d, and the images depend on the experimental parameters, we fix the experimental parameters and change the values of $S_{\bar{s}}/S_{\bar{d}}$, $S_{\Delta d}/S_{\bar{d}}$, and ξ_s - ξ_d to calculate the theoretical image. We then calculate the rms deviation over all the pixel values of the calculated

this procedure. For example, if we set $S_{\bar{s}}/S_{\bar{d}}$ = -0.46 to -0.36, $S_{\Delta d}/S_{\bar{d}}$ = -0.38 to -0.28 and ξ_s - ξ_d = 2.00 to 2.10 with an increment of 0.02 for each of these settings, the program will calculate the image for 216 combinations of these parameters and find the best fitting set of the parameters. It is worth pointing out that we first set the parameters with a larger range and with a larger increment for trial calculation. This trial calculation may be repeated for several times. This is the most important procedure in our data analysis for extracting the atomic parameters from the angular distribution that creates these images.

The calculated image shown in Fig. 5.4 (b) is the best fitting image to the data in Fig. 5.4(a). Fig. 5.4(c) to (e) illustrate three cross-sectional slices for rows 45, 65 and 85 of the image, respectively, showing the data points (from the measured image (a)) and the best fitting curves (from the calculated image (b)). Fig. (h) is the photoelectron angular distribution.

The results from all the nine wavelengths of laser light are listed in Table 5.2.

As we discussed earlier, the images obtained with linearly-polarized light can not be used for quantitative analysis for determining the atomic parameters due to insufficient conditions. However, we could use the cross sections and phases determined with elliptically-polarized light to produce the linear-polarization angular distributions. Fig. 5.5 illustrates both the recorded (a) and the calculated images (b) with linear light at the wavelength of 540 nm. The polarization direction of the light is 45° from vertical, i.e. ϵ_3/ϵ_1=+1. The calculated image in Fig. 5.5 (b) is based on the data we determined from the image with elliptically-polarized light in Fig. 5.4(a). To match the measured image, we adjust the amplitude of the signal, the size and position of the image. Fig. (c), (d), and (e) are cross-sectional slices for rows 45, 65 and 85, respectively, showing the data points (from Fig. (a)) and the cross section curve (from Fig. (b)). Figs. (f) and (g) are mesh plots for image (a) and (b), respectively. The calculated angular

Table 5.1: Experimental parameters for each wavelength

λ (nm)	ε (meV)	V (V)	Number of shots	ϵ_3/ϵ_1	Pulse energy (mJ)	Image radius (cm)
590.0	26	0.05	8000	$+0.438i$	1.3	0.55
583.3	74	0.40	8000	$+0.437i$	1.3	0.65
583.3	74	0.40	8000	$-0.437i$	1.3	0.65
575.0	135	0.65	8000	$-0.435i$	1.3	0.82
568.2	187	1.0	25000	$-0.433i$	2.5	0.80
560.0	251	1.4	10000	$-0.431i$	2.5	0.79
553.0	307	1.8	10000	$-0.429i$	2.5	0.77
547.0	356	2.2	25000	$-0.427i$	2.5	0.81
540.0	415	2.2	10000	$-0.426i$	2.5	0.86
532.0	484	2.6	10000	$-0.424i$	2.5	0.88

Table 5.2: Relative two-photon moments, cross sections and continuum wave functions as determined from the photoelectron images.

λ (nm)	$S_{\bar{s}}/S_{\bar{d}}$	$\lvert S_{\Delta d}/S_{\bar{d}}\rvert$	σ_s/σ_d	$\sigma_{5/2}/\sigma_{3/2}$		$\xi_s-\xi_d$ (rad)
				$S_{\Delta d}/S_{\bar{d}}>0$	$S_{\Delta d}/S_{\bar{d}}<0$	
590.0	−0.55(2)	0.35(2)	0.32(3)	0.27(3)	12(3)	2.36(7)
583.3	−0.47(2)	0.33(2)	0.25(3)	0.30(3)	11(3)	2.34(6)
575.0	−0.45(2)	0.32(2)	0.22(3)	0.32(3)	10(3)	2.25(6)
568.2	−0.40(2)	0.32(2)	0.18(2)	0.32(3)	9(2)	2.15(4)
560.0	−0.42(2)	0.36(2)	0.19(2)	0.26(3)	14(2)	2.08(4)
553.0	−0.43(2)	0.34(2)	0.20(2)	0.29(3)	11(2)	1.98(4)
547.0	−0.38(2)	0.36(2)	0.15(2)	0.26(3)	13(2)	2.02(4)
540.0	−0.39(2)	0.35(2)	0.16(2)	0.27(3)	12(2)	1.96(4)
532.0	−0.38(2)	0.34(2)	0.15(2)	0.29(3)	11(2)	1.85(4)

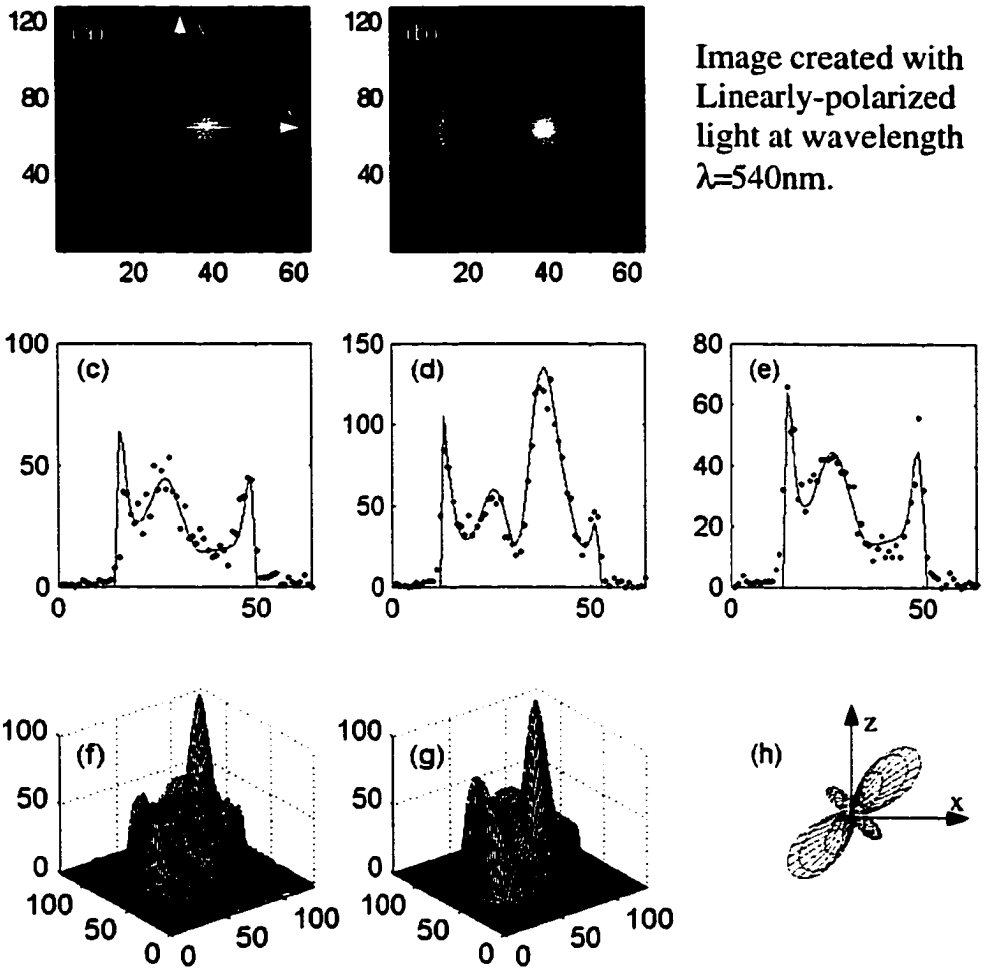

Figure 5.5: Example of an image taken with linearly-polarized light at 45° from vertical (θ = + 45°). (a) is the measured image, (b) is the corresponding calculated image. (c), (d), and (e) are cross-sectional slices for rows 45, 65 and 85, respectively, showing the data points and the best fitting curve. (f) and (g) are mesh plots for images (a) and (b), respectively, and the calculated angular distribution that produces this image is shown in Fig. (h).

distribution that produces this images is shown in Fig(h). Similar to Figs. 5.4 and 5.5, we show two more images taken at laser wavelength of 583.3 nm. In Fig. 5.6, (a) is the recorded image, which is taken with right-elliptically-polarized laser light with the ellipticity of the laser polarization $\epsilon_3/\epsilon_1 = +0.437i$. This image is also one of the images we have used for extracting the atomic parameters, (b) is the corresponding calculated image. Fig. 5.6(c) to (e) illustrate three cross-sectional slices for row 45, 65 and 85 of the image, respectively, showing the data points (from the measured image (a)) and the best fitting curves (from the calculated image (b)). Fig. (h) is the corresponding photoelectron angular distribution. Note that the two minima of this distribution in the x – z plane are located in the second and fourth quadrants. While in Fig. 5.4 (h), the angular distribution associated with left-elliptically-polarized laser light, the two minima in the x – z plane are located in the first and third quadrants. From these two distributions we also see that with shorter laser wavelength the distribution becomes more elongated. In Figs. 5.4(a) and 5.6(a), the dark bands of the images are located in right-hand side and left-hand side, respectively. Fig. 5.7 illustrates both the recorded (a) and the calculated images (b) with linear light at the wavelength of 583.3 nm. The polarization direction of the light is 45° from vertical, i.e. $\epsilon_3/\epsilon_1 = -1$. The calculated image in Fig. 5.5 (b) is based on the data we determined from the image with elliptically-polarized light in Fig. 5.6(a). The calculated angular distribution that produces this image is shown in Fig. (h).

In order to estimate the statistical error of the data, we collected five sets of images for both 547 nm and 568.2 nm wavelengths. Each image data were collected by accumulating the images over 5000 laser shots. Based on the five sets of data taken from each of these two wavelengths we calculate the average values of the three parameters and their standard deviations. These data are listed in Table 5.3. From these data we see that percentage uncertainties for ξ_s - ξ_d are about 1.5%

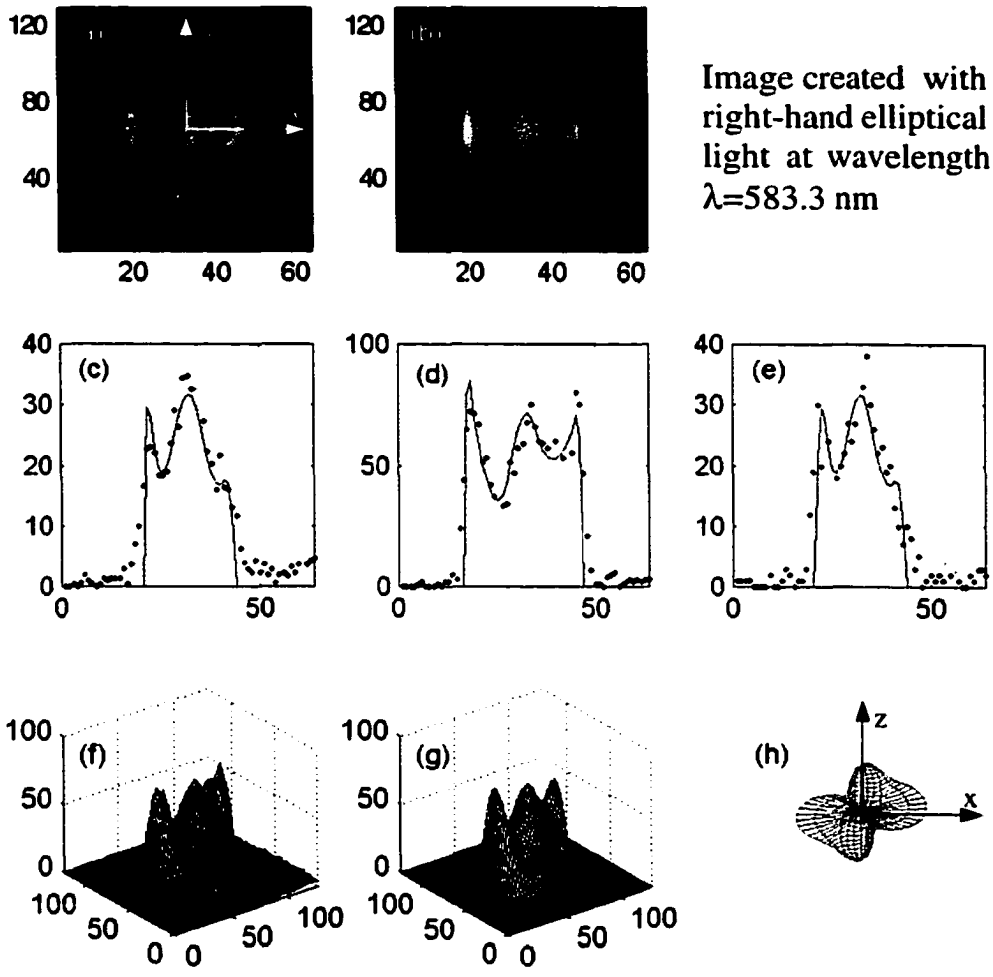

Figure 5.6: Example of an image taken with right-elliptically-polarized light. (a) is the measured image, (b) is the corresponding calculated image. (c), (d), and (e) are cross-sectional slices for rows 45, 65 and 85, respectively, showing the data points and the best fitting curve. (f) and (g) are mesh plots for images (a) and (b), respectively, and the calculated angular distribution that produces this image is shown in Fig. (h).

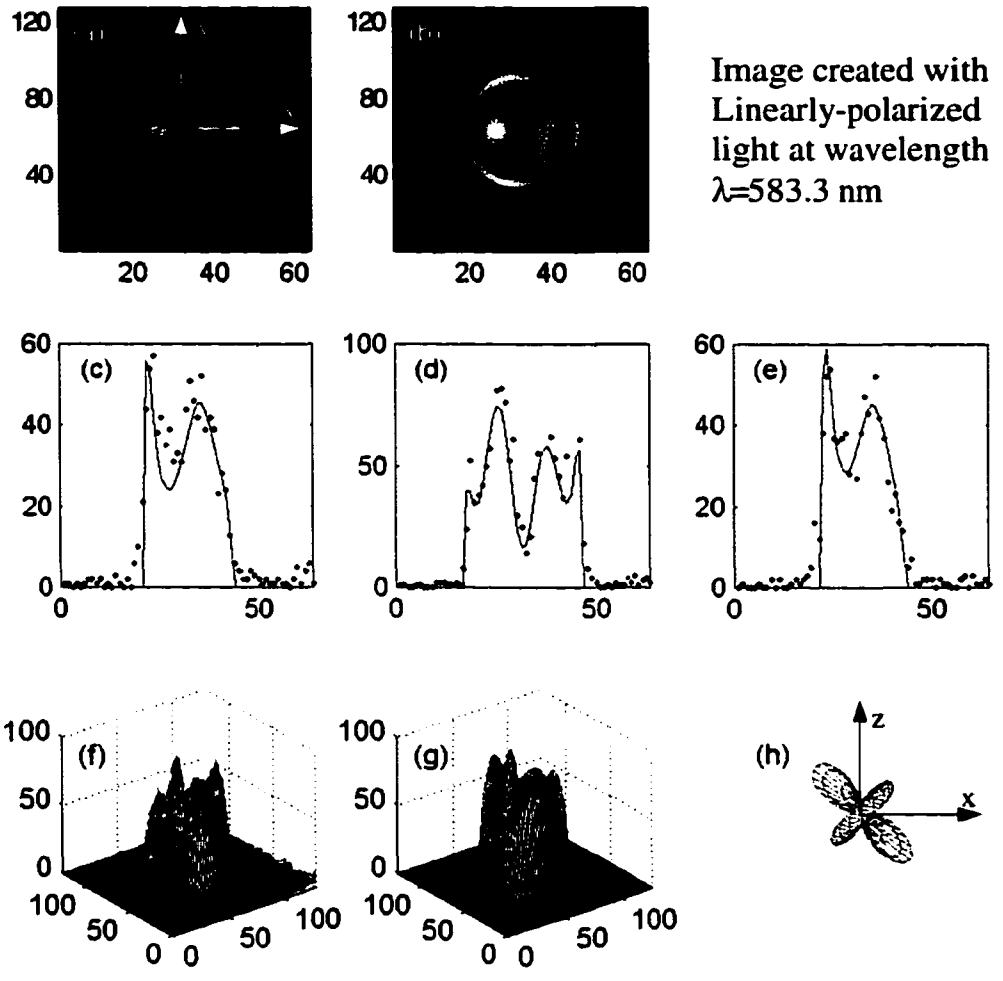

Figure 5.7: Example of an image taken with linearly-polarized light at 45° from vertical ($\theta = -45°$). (a) is the measured image, (b) is the corresponding calculated image. (c), (d), and (e) are cross-sectional slices for rows 45, 65 and 85, respectively, showing the data points and the best fitting curve. (f) and (g) are mesh plots for images (a) and (b), respectively, and the calculated angular distribution that produces this image is shown in Fig. (h).

and 1%; for σ_s / σ_d are 7% and 6%; for $\sigma_{5/2} / \sigma_{3/2}$ are 9% and 6%, respectively. We can also see that the statistical error for the phase difference is very small, while that for the ratios of the cross sections are larger but acceptable. The systematic error may be caused by any non-uniformities in the detector system and shot noise. The background noise for most of the images is less than 5% of the average image pixel value. The background noise, which we estimate to be only about 2% of the maximum signal over the entire image area, does not change the distribution observably. It increases the average pixel value of each image. Therefore the influence of the background to the parameters is estimated to be less than 2%. Another factor for the error of the measurements is the influence of the upper mesh. Some electrons hit the wires instead of going through the mesh. The paths of these electrons will be changed and hence it affects the distribution. Because of the high acceleration field between the mesh and the phosphor screen of the MCP assembly, the paths will not be changed visibly. And because the images are much larger than the holes of the mesh, the influence is further reduced. One more factor for the error is the finite size of the interaction region. When we fitted the calculated images to the measured images, we did not account for the vertical size of the interaction region. Because the interaction region is much smaller than the images, this influence is also unnoticeable. Consider these factors and the systematic error we give larger uncertainties to the atomic parameters we quote in Table 5.2.

Table 5.3: The values and the standard deviations of the atomic parameters for images taken with 547 nm and 568.2 nm wavelength laser light.

Wavelength (nm)	$\xi_s - \xi_d$	σ_s / σ_d	$\sigma_{5/2} / \sigma_{3/2}$
547.0	2.02±0.03	0.15±0.01	13.4±1.2
568.2	2.15±0.02	0.18±0.01	8.4±0.6

5.3.2 Relative cross sections of *s*- and *d*-waves

From Eq. (2.13), we can express the cross section ratios as

$$\sigma_s/\sigma_d=\frac{5}{4}\left(\frac{(S_{\bar{s}}/S_{\bar{d}})^2}{1+\frac{3}{2}(S_{\Delta d}/S_{\bar{d}})^2}\right) \tag{5.3a}$$

and

$$\sigma_{5/2}/\sigma_{3/2}=\frac{3}{2}\left(\frac{1-S_{\Delta d}/S_{\bar{d}}}{1+\frac{3}{2}S_{\Delta d}/S_{\bar{d}}}\right)^2, \tag{5.3b}$$

Based on the best fitting values of $S_{\bar{s}}/S_{\bar{d}}$ and $S_{\Delta d}/S_{\bar{d}}$, we can determine the cross-section ratios σ_s/σ_d and $\sigma_{5/2}/\sigma_{3/2}$. These relative cross sections are also presented in Table 5.2. Since the angular distribution and the coefficients given by Eqs. (2.8), (2.10) and (2.14) ~ (2.16) depend on the square of $S_{\Delta d}/S_{\bar{d}}$, the sign of $S_{\Delta d}/S_{\bar{d}}$ cannot be determined uniquely in our measurements, and hence the ratio of the cross sections, $\sigma_{5/2}/\sigma_{3/2}$ has two possible values. We list both values in Table 5.2. Positive $S_{\Delta d}/S_{\bar{d}}$ yields $\sigma_{5/2}/\sigma_{3/2}<1.5$, while $\sigma_{5/2}/\sigma_{3/2}>1.5$ is from negative $S_{\Delta d}/S_{\bar{d}}$.

Fig. 5.8 shows the values of σ_s/σ_d as a function of photoelectron kinetic energy. The ratio of the relative cross sections of the *s*- and *d*-waves decreases with increasing photoelectron energy to an energy up to about 200 meV. Beyond that range, the change is relatively small. In addition to data from the present work (solid circles), we also plot three sets of theoretical results. The theoretical data points are calculated based on a Sturmian basis set (x signs) [62] and a Hartree-Fock basis set (+ signs) [63], respectively. The solid line is the result from recent theoretical work [78]. This work is based on the relativistic second-order perturbation theory. This result shows a large discrepancy with both our results and the previous theoretical works (x and + signs). The fine structure effect is ignored in all these calculations. The energy dependence of the Sturmian basis

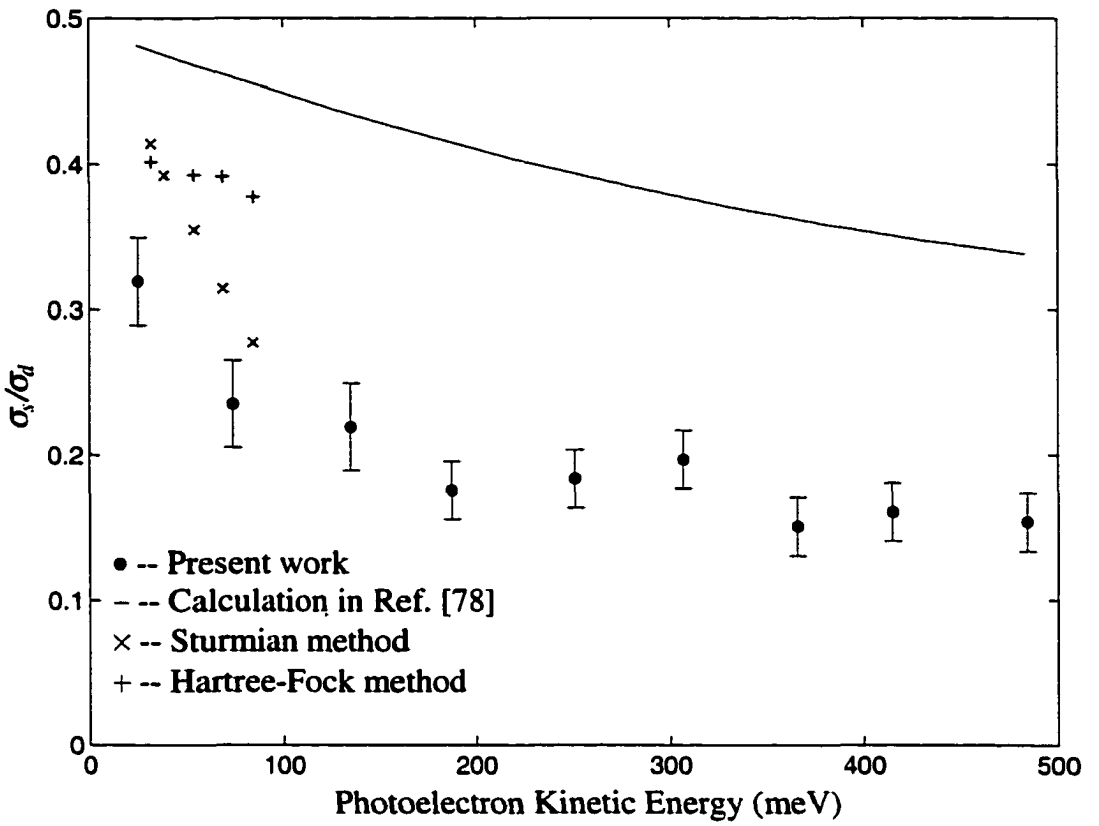

Figure 5.8: The ratio of cross sections σ_s / σ_d as a function of photoelectron kinetic energy. The ×-signs and the plus (+) signs represent the data calculated based on a Sturmian basis set [62] and a Hartree -Forck basis set [63], respectively. The solid circular data points are from the present work. The solid line is the theoretical result from Ref. [78].

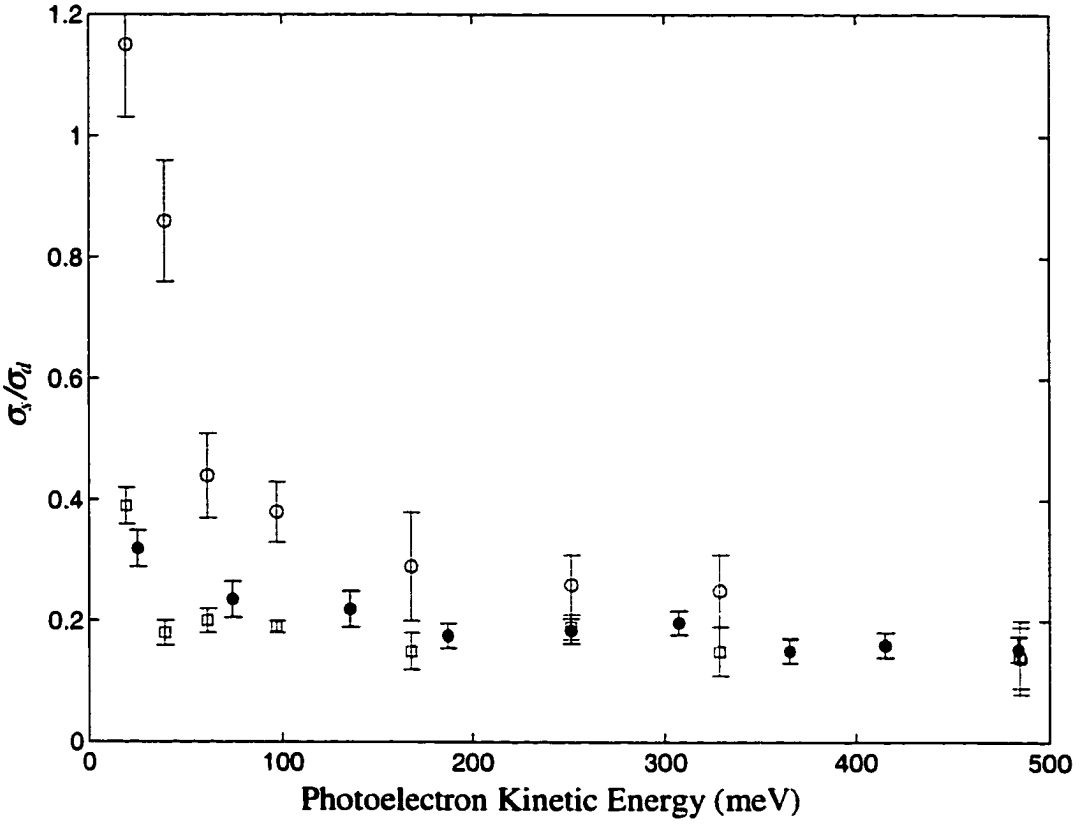

Figure 5.9: The ratio of the cross section σ_s / σ_d as a function of the photoelectron kinetic energy with a comparison to the previous work [50] using conventional technique for measuring the PAD. The solid circular points (dark blue) are the results of present work. The data points from the previous work were obtained by ignoring the fine structure effect (red open circles) and by using the calculated value of $\cos(\xi_s - \xi_d)$ (red squares). The latter results are in reasonable agreement with our present results.

the results also have large deviation from 1.5, which cover from 2 ~ 23 or 0.18 ~ 1. These data were obtained using the calculated value of phase difference, together with the experimental fitting parameters. In view of the inconsistent deviation of these data and the dependence on various assumptions as mentioned earlier, we regard the present results as the more reliable determination.

Fig. 5.11 is a figure from resent theoretical work [78]. The solid line in this figure is the result from this work. The solid circles are our experimental results. The triangle and the solid square data points are results from bound state spectra from [55] and [79], respectively. The ratios $\sigma_{5/2}/\sigma_{3/2}$ from the bound state transitions are close to 1.5, which is the value with ignoring the fine structure effect. Our data show a large discrepancy with these data. This discrepancy suggests fine structure effect for the ratio $\sigma_{5/2}/\sigma_{3/2}$.

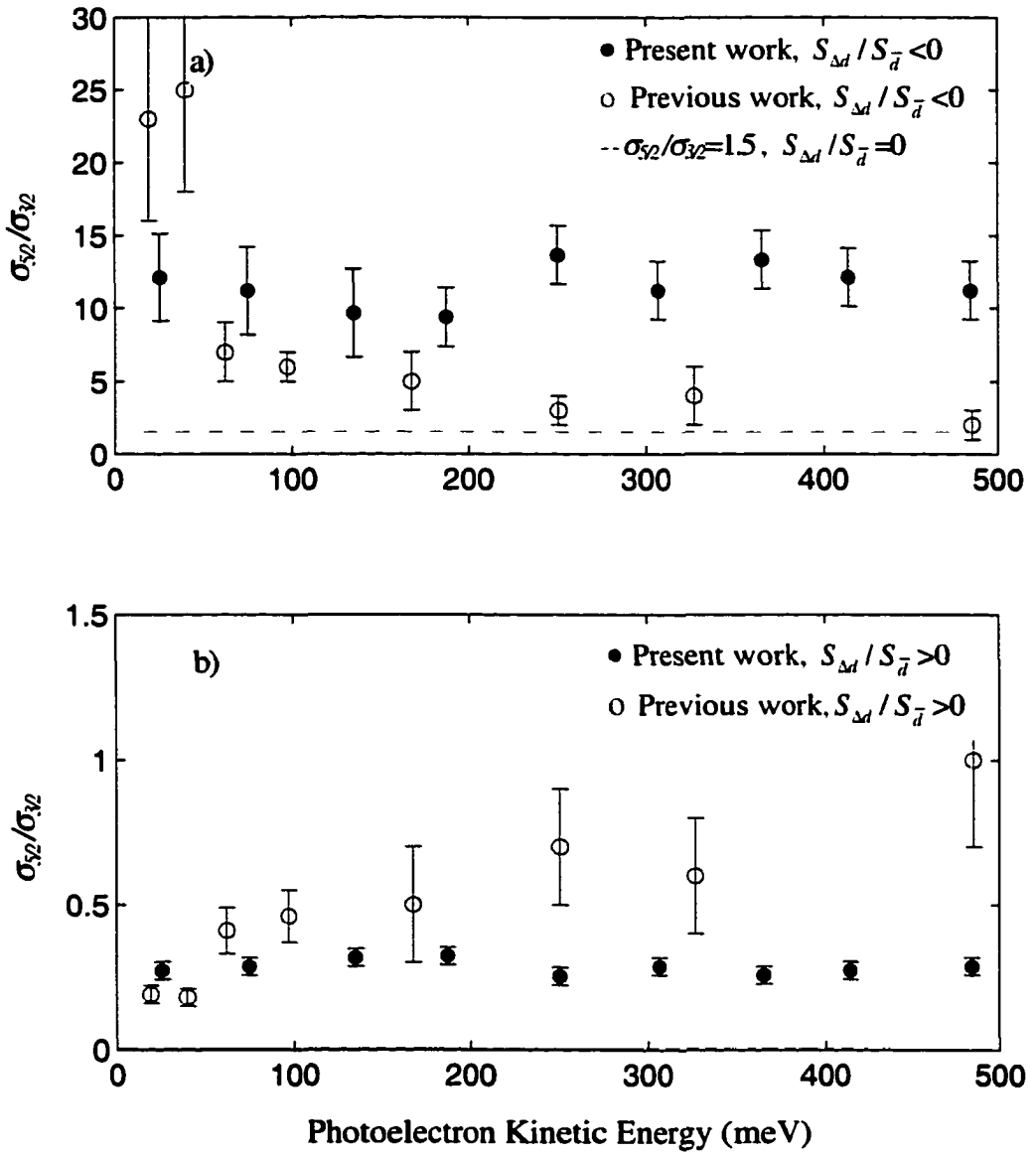

Figure 5.10: The ratio of cross sections $\sigma_{5/2}/\sigma_{3/2}$ as a function of photoelectron kinetic energy. The solid circular data points are from the present work and the open circles are the data from the previous work [50] using conventional technique for measuring the PAD. Data associated with a) $S_{\Delta d}/S_{\bar{d}}<0$ and b) $S_{\Delta d}/S_{\bar{d}}<0$. The dash line (--) represents the value ca lculated based on the Eq. (5.3b) with $S_{\Delta d}/S_{\bar{d}}=0$ (i.e. ignoring the fine structure effect).

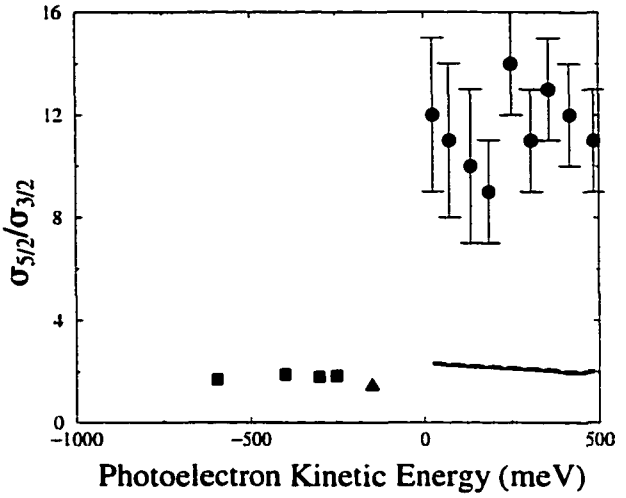

Figure 5.11: The ratio of the cross section $\sigma_{5/2}/\sigma_{3/2}$ as a function of the photoelectron kinetic energy with a comparison to the results from theoretical works. The solid circular points are the results of present work. The solid line is the result from resent theoretical work [78]. The triangle and the solid square data points are results from bound state spectra from [55] and [79], respectively. (J. Colgan and M.S. Pindzola, PRL, 86, 1998 (2001))

5.3.3 Relative phases between *s*- and *d*-waves

We can calculate the phase difference in terms of the quantum-defect phase shift and Coulomb phase shift. The quantum-defect phase shifts for *s*- and *d*-waves can be expressed as (see Appendix E)

$$\delta_s=(3.131-0.175\varepsilon+0.359\varepsilon^2)\pi \tag{5.4a}$$

and

$$\delta_d=(1.347+0.599\varepsilon-1.39\varepsilon^2)\pi \tag{5.4b}$$

The quantum-defect phase difference between s- and d- waves

$$\delta_s-\delta_d=(1.784-0.774\varepsilon+1.749\varepsilon^2)\pi \tag{5.5}$$

where ε is the photoelectron kinetic energy in Rydbergs. The Coulomb phase has the form [57]

(5.6)

$$\eta_{l'} = \arg\{\Gamma[l' + 1 - (i/k)]\},$$

where l' is the electron orbital angular momentum. This leads to a phase difference between s- and d-waves of the form (see Appendix D)

$$\eta_s - \eta_d = \tan^{-1}\frac{1}{2\sqrt{\varepsilon}} + \tan^{-1}\frac{1}{\sqrt{\varepsilon}}, \tag{5.7}$$

The total phase difference is given by the sum of the quantum-defect phase shift and the Coulomb phase difference

$$\begin{aligned}\xi_s - \xi_d &= (\delta_s - \delta_d) + (\eta_s - \eta_d) \\ &= (1.784 - 0.774\varepsilon + 1.749\varepsilon^2)\pi + \arctan\left(\frac{1}{2\sqrt{\varepsilon}}\right) + \arctan\left(\frac{1}{\sqrt{\varepsilon}}\right)\end{aligned} \tag{5.8}$$

In Fig. 5.12, we plot the results of the continuum phase difference from our determination as a function of the kinetic energy of the photoelectron, ε. For comparison, we also show the expected values of the phase difference as given by the Eq. (5.8) (solid line), and the data points of the phase differences from the theoretical results of Refs. [62] and [63] .We see from the figure that there is very good agreement between our experimental determinations and the expected values or theoretical values. The agreement of these results is a direct experimental confirmation of the quantum defect theory over a large range of photoelectron kinetic energies for the first time. These reasonable results of phase difference and the ratio of the cross sections σ_s/σ_d also convince us that our developed technique is successful in the measurement of photoelectron angular distributions and determination of atomic parameters.

5.4 Conclusions

In this chapter we have presented the details of out complete measurements of two-photon ionization in rubidium atom using our newly-developed method. In other words, we have successfully determined the three microscopic atomic parameters--the relative cross sections between *S* and *D* ionization channels and two *D* fine structure states as well as the phase difference between *s*- and *d*-continuum waves. The measured phase differences are in excellent agreement with expected values over the entire range of photoelectron kinetic energy from 0 to 0.5 eV. The measured relative cross sections for ionization into *S* and *D* channels are in fair agreement with one set of theoretical data, but have a large discrepancy with resent theoretical results. However, our present results are quite consistent with the previous experimental data using the conventional technique for measurement of PAD. Both the relative cross sections and phase differences are slow varying functions of the photoelectron energy. The ratios of cross sections of the two *D* channels show a large deviation with theoretical values, but are fairly consistent with the previous experimental data, which were obtained using the calculated value of quantum defect phase difference and Coulomb phase shift without ignoring the fine structure effect. These calculated phases have been verified by our present experimental results. From this comparison, our present experimental data seem reasonable. And furthermore, the present data consistently deviate from 1.5. The ratios $\sigma_{5/2}/\sigma_{3/2}$ from the bound state transitions are close to 1.5, which is the value with ignoring the fine structure effect. Our data show a large discrepancy with these data. This discrepancy between the experimental data and the results from the bound state value suggests fine structure effect for the ratio $\sigma_{5/2}/\sigma_{3/2}$.

CHAPTER 6

QUANTUM INTERFERENCE BETWEEN ONE- AND TWO-PHOTON IONIZATION PROCESSES

6.1. Introduction

The coherent control of atomic and molecular processes has attracted much attention and seen great growth in the past decade. The process of coherent control is based on the quantum mechanical interference effect. The best-known example of interference is Young's double-slit experiment in optics. At each slit, a new cylindrical wave emerges and has a fixed phase related to the incident wave. An interference pattern appears on the observation screen with bright and dark fringes that depend on whether the two waves are in or out of phase at any point on the screen, that is, whether the interference is constructive or destructive. Since the intensity at a point is proportional to the square of the total electric field at that point, the expression for the total intensity contains a cross term with a phase difference between these two waves. It is the phase difference that governs the intensity at any point.

The interference effect in atomic and molecular transition processes, which connect the same initial and final states through different pathways, occurs by using two external laser fields with different frequencies. Quantum dynamical processes are wave phenomena, subject to constructive and destructive interference. The light waves themselves do not interfere significantly, as they have different frequencies, but the wave functions produced by the light waves strongly interfere. By varying the relative phases and amplitudes of the light

waves, it is possible to control the product distribution. This is because the probability of forming a specified product is proportional to the square of the sum of the transition amplitudes for the two pathways between the specified states. That is, the probability

$$\begin{aligned} P &= |A_1 + A_2|^2 \\ &= |A_1|^2 + |A_2|^2 + (A_1 A_2^* + A_1^* A_2), \end{aligned} \tag{6.1}$$

where A_i is the transition amplitude of obtaining the product through path i (i=1,2), and $|A_1|^2$ and $|A_2|^2$ are the probabilities for independently obtaining the product from path 1 and 2, respectively. $(A_1 A_2^* + A_1^* A_2)$ is the interference term, which contains a phase difference between the complex amplitudes. The total probability can be also written as

$$P = P_1 + P_2 + P_{12}\cos(\Delta), \tag{6.2}$$

where Δ is the phase difference between the two transition amplitudes due to the phase of optical fields and the atomic phase. Varying the laser phase allows one to control the distribution of the product.

The idea of phase control for a molecular transition process was first proposed and studied extensively by Brumer and Shapiro [65]. The experimental observation of quantum interference using phase control was first reported by Elliott and coworkers [38]. They observed the interference between two ionization processes in mercury by varying the phase difference between visible light of λ = 554 nm and its third harmonic UV light. Fig. 6.1 shows the transition processes and the ionization signal measured as a function of argon pressure in a delay cell. Each process was resonantly enhanced by the $6p^1P_1$ intermediate state and lead to the same continuum state. The overall transition probability was varied sinusoidally with a modulation depth of ~32% by changing the relative phase of the two fields.

The bound state population control process was first extended to molecular systems by Gordon and co-workers [40], who applied it to diatomic molecules (HCl and CO), and later by Bersohn and co-workers [41], who controlled the population transfer in a number of polyatomic molecules, such as NH_3, CH_3I, trimethylamine, triethylamine and cyclooctatetriene. These measurements represent an extension of using the quantum interference effect to large, complex molecules. The modulation depth of 75% was achieved for the case of CH_3I, while the typical value for all of the studies was 25-50%. The interference observed in all these studies is associated with fundamental and third harmonic (ω-3ω) transitions, in which the initial and final states are both discrete bound states. In this case the interference occurs only between either two odd-order processes or two even-order processes.

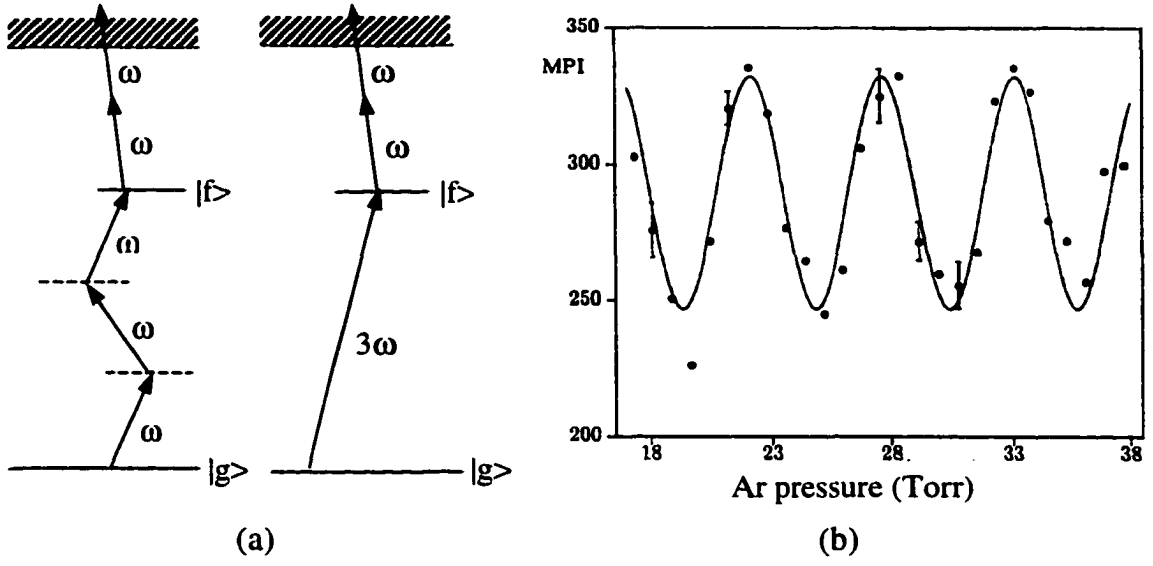

Fig. 6.1. The experimental observation of quantum interference in mercury.
(a) The two processes in Hg that interfere using two color fields and
(b) The ionization signal measured as a function of argon pressure in a delay cell. The solid curve in (b) is the best fit to the data.
(Chen, Yin and Elliott, PRL, **64**, 507, 1990)

Control of bound-to-continuum transitions by quantum interference between paths has also been studied by several groups. Gordon's group [66] reported that quantum interference can be used to control the branching ratio in a chemical reaction of HI and DI. They controlled the relative amounts of HI^+ and I^+ produced in the photo-excitation (ω-3ω) of HI by varying the phase difference between two laser beams with wavelength of 354.98 nm and its third harmonic 118.33 nm. The HI^+ and I^+ signals were modulated as the phase difference was varied, with the HI^+ signal lagging the I^+ by as much as 150°. A second demonstration of control over the branching ratio was reported by Shnitman *et.al.* [76]. In this process, control over the Na(3d)/Na(3p) branching ratio in the photodissociation of Na was demonstrated using two incoherently related laser sources. Their results showed a depletion in the Na(3d) product of at least 25% and a concomitant increase in the Na(3p) yield as the relative frequency of the two lasers was scanned. This process is independent of the relative phase between the two light fields. The possibility of controlling the branching ratio by using two uncorrelated lasers was first discussed by Chen, Brumer and Shapiro [68].

Almost at the same time with Shnitman's report, two other studies on the control of the branching ratio by using incoherently related lasers were reported by Pratt and Elliott's group. Pratt [69] reported his studies using this technique to control the energy distribution of photoelectrons ejected from NO by small tunings from resonance in either or both of the two resonant pathways. Elliott and co-workers [70] controlled the quantum states of Ba^+ produced by the ionization of Ba atoms. They observed the branching ratio change from 95% to 58% in tuning one laser from one side of resonance to the other.

Bound-continuum coherent control of angular distributions of photoelectrons has also been achieved by quantum interference between competing channels. Elliott and co-workers observed the asymmetric angular distributions of photoelectrons produced from Rb atoms [49] and NO molecules [71] using a

fundamental field and its second harmonic (ω-2ω). These measurements were severely limited in that the photoelectron flux was detected by using the conventional technique stated earlier, in which four discrete photoelectron detectors in a plane were used. Therefore these measurements only illustrate the variation of photoelectron flux with varying the relative phase between the two fields. More complete measurements could be helpful in more fully understanding the interference effect and exploring the interference measurements to determine the phase difference between the continuum waves with even and odd parity, which cannot be obtained by single color experiments.

In the preceding chapters we have described the measurements of PAD with our newly-developed technique and the method to determine the phase difference between two even-parity continuum waves. In the present chapter, we describe our investigation of a quantum mechanical interference between an even-parity and an odd-parity wave in rubidium with two-color laser fields. Our motivations for this study are in the following aspects:

- To develop an intuition of the asymmetric angular distributions of photoelectrons (i.e. the asymmetric electron cloud) created by interfering even- and odd-order photoionization processes and give us insight into the quantum interference phenomena.
- To obtain photoelectron images through quantum interference control over PAD using perpendicularly-polarized two-color laser fields.
- To determine the phase difference between even- and odd-continuum waves based on the analysis on these images.
- To test the degree to which the atomic wavefunction of the continuum state formed by the two-color field can be described as the coherent superposition of the individual continuum states.

The major purpose of this study is to derive the phase difference between even- and odd-continuum waves based on the analysis of measured angular distribution images using two-color laser fields. In a recent theoretical work, Nakajima [77] proposed a method of determining the phase difference between even- and odd-continuum states by isolating the contributions of different ionization channels. These include using circularly-polarized light (eliminating the *s*-wave) for the measurement of PAD to determine the phase difference between *p*- and *d*-waves and using linearly-polarized light, but measuring the photoelectron flux at a special angle (at which the *d*-wave does not exist) to determine the phase between *p*- and *s*-waves. Nakajima pointed out that the use of linearly- and circularly-polarized light is complementary. Also this suggested method is based on the conventional technique of measuring the PAD. As we have mentioned earlier that this technique has some disadvantages for this measurement. With our technique, we collect the photoelectrons ejected in all directions and create a photoelectron image on the screen of our detector. By fitting a theoretical image to the measured image we could derive the phase difference between even- and odd-waves. This technique provides a sensitive means of determining the atomic parameters. The information can be extracted from these measurements since the transition amplitude for the process depends on the phase shift of the two optical fields and the phase of the continuum states.

In this chapter, we report the first observation of quantum interference using perpendicularly-polarized two-color laser fields. One field is the second harmonic of the other. The fundamental visible field (λ=560 nm) is polarized vertically and the UV field (λ=280 nm) is polarized horizontally. We measure the photoelectron angular distributions produced by interfering even- and odd-order processes of the Rb atom using our newly-developed electron detection technique. We present the details of experiments, the results and analyses, including the determination of the relative phase between the two optical fields and how to extract the phase

difference from measured images. We will show the extremely asymmetric angular distribution images as the optical phase between the two fields was varied using both perpendicularly-polarized and parallel-polarized two-color laser fields. In order to determine the relative phase of continuum waves using quantum interference experiment, it is required to design a method to measure the relative phase between the two laser fields -- the vertically-polarized fundamental visible field and the horizontally-polarized second harmonic UV field. We will describe this method in detail.

We derived the phase difference between the *p*- and *d*-continuum waves from the angular distribution images for the first time. The measured value of the phase difference is in good agreement with the value calculated based on quantum defect theory.

6.2 Phase control over the angular distribution of photoelectrons

In this section we describe the principle of phase control over the angular distributions of photoelectrons ejected from two pathway optical interactions in atomic rubidium. This ionization process produces quantum interference between two bond-continuum transition channels, $5s^2S_{1/2} \rightarrow n^2P \rightarrow \varepsilon d\ ^2D_{3/2,5/2}$, $\varepsilon s\ ^2S_{1/2}$ for two- photon process and $5s^2S_{1/2} \rightarrow \varepsilon p\ ^2P_{1/2,\ 3/2}$ for one-photon process, excited by the

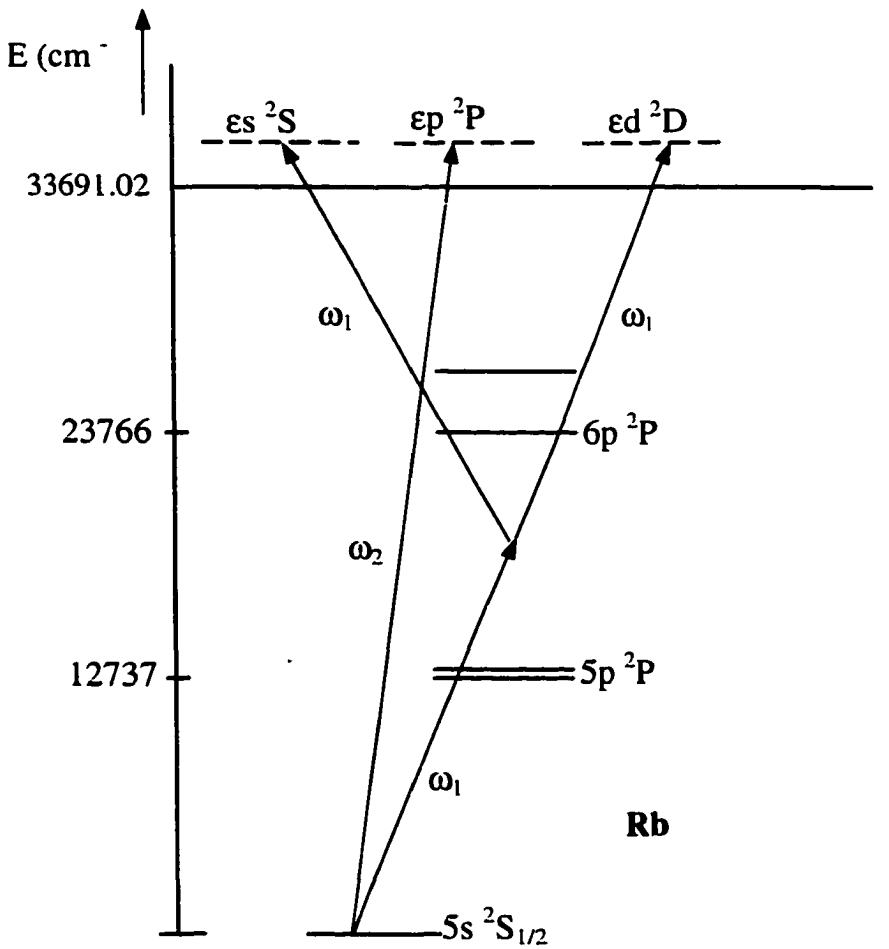

Figure 6.2: Energy level diagram of atomic rubidium for two-color experiments. The arrows indicate the pathways of quantum interference by two-color laser fields with frequency ω_1 and $\omega_2 = 2\omega_1$

fields of frequency ω_1 (λ=560nm) and ω_2 (λ=280nm) = $2\omega_1$, respectively. A diagram for selected Rb energy levels and the ionization processes is shown in Fig. 6.2.

The electric field of the coherent light waves acting on the atoms can be expressed as

$$\mathbf{E}(t) = \mathbf{E}_1\cos(\omega_1 t+\phi_1) + \mathbf{E}_2\cos(\omega_2 t+\phi_2), \tag{6.3}$$

where $\mathbf{E}_1$ and $\mathbf{E}_2$ are the amplitudes of the fundamental and second harmonic fields, respectively, and ϕ_1 and ϕ_2 are the phases of the two fields. Under these circumstances the continuum state wave function is a coherent superposition of even-parity εS and εD waves and an odd-parity εP wave. Therefore, the overall wave function would lead to an asymmetric angular distribution.

When an atom is simultaneously excited by optical electric fields, $E_1(\omega_1)$ and $E_2(\omega_2)$, the total transition amplitude for excitation is the sum of an amplitude for absorbing one photon of frequency ω_2 and an amplitude for absorbing two photons of frequency ω_1. In this case, the symmetry becomes of extreme importance. The angular distribution of photoelectrons is proportional to the square of the sum of the total transition amplitude

In order to determine the relative quantum phase between even and odd partial waves based on the measured angular distributions of photoelectrons, Elliott [72] extended the theory of multiphoton ionization of atoms presented by Bebb and Gold to include ionization with multiple-frequency laser fields. According to the extended theory, for a two-color field with the visible beam polarized in the z direction and UV beam polarized in the x direction, the angular distribution of photoelectrons can be written as

$$W(\Theta,\Phi) \propto \sum_{i,j=+/-}\left|\frac{eE^{2\omega}\exp(i\phi_{2\omega})}{2\hbar}O_{ij}^{(1)} + \frac{e^2(E^{\omega})^2\exp(2i\phi_{\omega})}{4\hbar^2}T_{ij}^{(33)}\right|^2 \tag{6.4}$$

where E^{ω} and $E^{2\omega}$ are the amplitudes of the fundamental frequency (ω) and second harmonic (2ω) components of the laser field, respectively, ϕ_{ω} and $\phi_{2\omega}$ are the phases of the two optical waves, and $O_{ij}^{(p)}$ and $T_{ij}^{(pq)}$ are the spatial components of the one- and two-photon transition moments, respectively. The indices i, j =+ or − represent the spin of the ground and final state electron, respectively, and p, q=1 or 3 represent the relevant spatial components, which are expressed as the following explicit forms

$$O_{++}^{(1)} = \frac{-4\pi i}{\sqrt{6}} e^{i\xi_p} \left\{ -Y_{11}(\Theta,\Phi) R_{3/2} + Y_{1-1}(\Theta,\Phi) \frac{R_{3/2} + 2R_{1/2}}{3} \right\} \tag{6.5a}$$

$$O_{+-}^{(1)} = \frac{-4\pi i}{\sqrt{3}} e^{i\xi_p} Y_{10}(\Theta,\Phi) \left(\frac{R_{3/2} - R_{1/2}}{3} \right) \tag{6.5b}$$

$$T_{++}^{(33)} = \frac{1}{3} e^{i\xi_s} Y_{00}(\Theta,\Phi) S_{\bar{s}} - \frac{2}{3\sqrt{5}} e^{i\xi_d} Y_{20}(\Theta,\Phi) S_{\bar{d}} \tag{6.5c}$$

$$T_{+-}^{(33)} = \sqrt{\frac{2}{15}} e^{i\xi_d} Y_{21}(\Theta,\Phi) S_{\Delta d} \tag{6.5d}$$

For two laser fields with parallel polarization in the x direction, the equations (6.4) and (6.5) are the same except that $T_{++}^{(33)}$ and $T_{+-}^{(33)}$ in Eqs. (6.4), (6.5c) and (6.5d) should be changed to $T_{++}^{(11)}$ and $T_{+-}^{(11)}$, respectively. (See Eq. (2.10c) and (2.10f) for the explicit form of these amplitudes) The — (−+) component is obtained from the ++ (+−) component for the $O_{ij}^{(1)}$ terms by changing $Y_{lm} \rightarrow -Y_{l-m}$, and $Y_{lm} \rightarrow Y_{l-m}$ for the $T_{ij}^{(33)}$ terms. Equations (6.5a) and (6.5b), which are associated with the single–photon transition, contain only the phase of the p-partial wave, ξ_p. $R_{1/2}$ and $R_{3/2}$ are single–photon transition moments from the ground state $5s^2S_{1/2}$ to the continuum $\varepsilon^2 P_{1/2,\,3/2}$. Equations (6.5c) and (6.5d) contain the phases of s- and d-

waves, ξ_s and ξ_d. $S_{\bar{s}}=\frac{S_1+2S_2}{3}$ and $S_{\bar{d}}=\frac{5S_3+S_4+9S_5}{15}$ are the average moments for exciting the s- and *d*-waves, respectively, and $S_{\Delta d}=\frac{5S_3+S_4-6S_5}{15}$ is the asymmetry in the moments for exiting the *d*-wave. The S_i (i=1~5) represent two-photon transition moments for transitions $5s^2S_{1/2}\rightarrow n^2P\rightarrow\varepsilon^2S_{1/2}$ and $5s^2S_{1/2}\rightarrow n^2P\rightarrow\varepsilon^2D_{3/2,\ 5/2}$, as explained in Chapter 2 in detail. It is clear from inspecting Eqs. (6.4) and (6.5) that the phase terms $cos(\Delta\phi+\xi_p-\xi_s)$ and $cos(\Delta\phi+\xi_p-\xi_d)$ are involved in the angular distribution expression. By adjusting $\Delta\phi = \phi_{2\omega} - 2\phi_{\omega}$, which is the relative phase between the two fields, very asymmetric angular distributions can be obtained. Based on these equations we are able to calculate the 3-dimensional angular distributions and 2-dimensional images, so that we can determine the phase difference between even (*s*- or *d*-) and odd (*p*-) waves by fitting the calculated images to the recorded images.

6.3 Experiment

The experimental apparatus consists of a vacuum system, a laser and optical system, a detector and a data acquisition system. The details of the apparatus have already been described in Sec. 3.2 and Chapter 4, as shown schematically in Figs. 3.1 and 3.2 for the detector, Fig 4.2 for the oven and Fig. 5.1 for the optical and laser system. For this study, we have modified the optical system to satisfy the requirements for performing the two-color interference experiment. A Mach-Zehnder-like set-up and a phase delay cell are the two major parts of this system. In this section, we describe the Mach-Zehnder-like set-up and related measurements.

6.3.1 Mach-Zehnder interferometer and adjustment of UV and visible beams

The configuration of the optics is shown schematically in Fig. 6.3. A vertically polarized 560 nm dye laser beam is first weakly focused by a 100 cm focal length lens and then split into two components at the input beam splitter (SP) of a Mach-Zehnder interferometer-like set-up. The beam splitter SP reflects 35% of the power to a type I phase-matched BBO crystal to generate the second harmonic 280 nm UV light, which is polarized horizontally. The transmitted 560 nm visible beam is then reflected by a mirror M_1 and is overlapped with the UV beam at mirror M_3, which reflects 99% of the UV power. Thereafter both the visible and UV beams travel together through a variable density N_2 delay cell into the interaction chamber and cross an atomic beam of rubidium. In order to observe the interference, we must ensure that the two beams are overlapped and parallel to each other to at least 10^{-2} mrad, as will be shown in Sec. 6.3.5. To satisfy this condition, we use the following adjustment procedure. We first adjust mirror M_2 until the transmitted visible beam from the BBO is overlapped with the visible

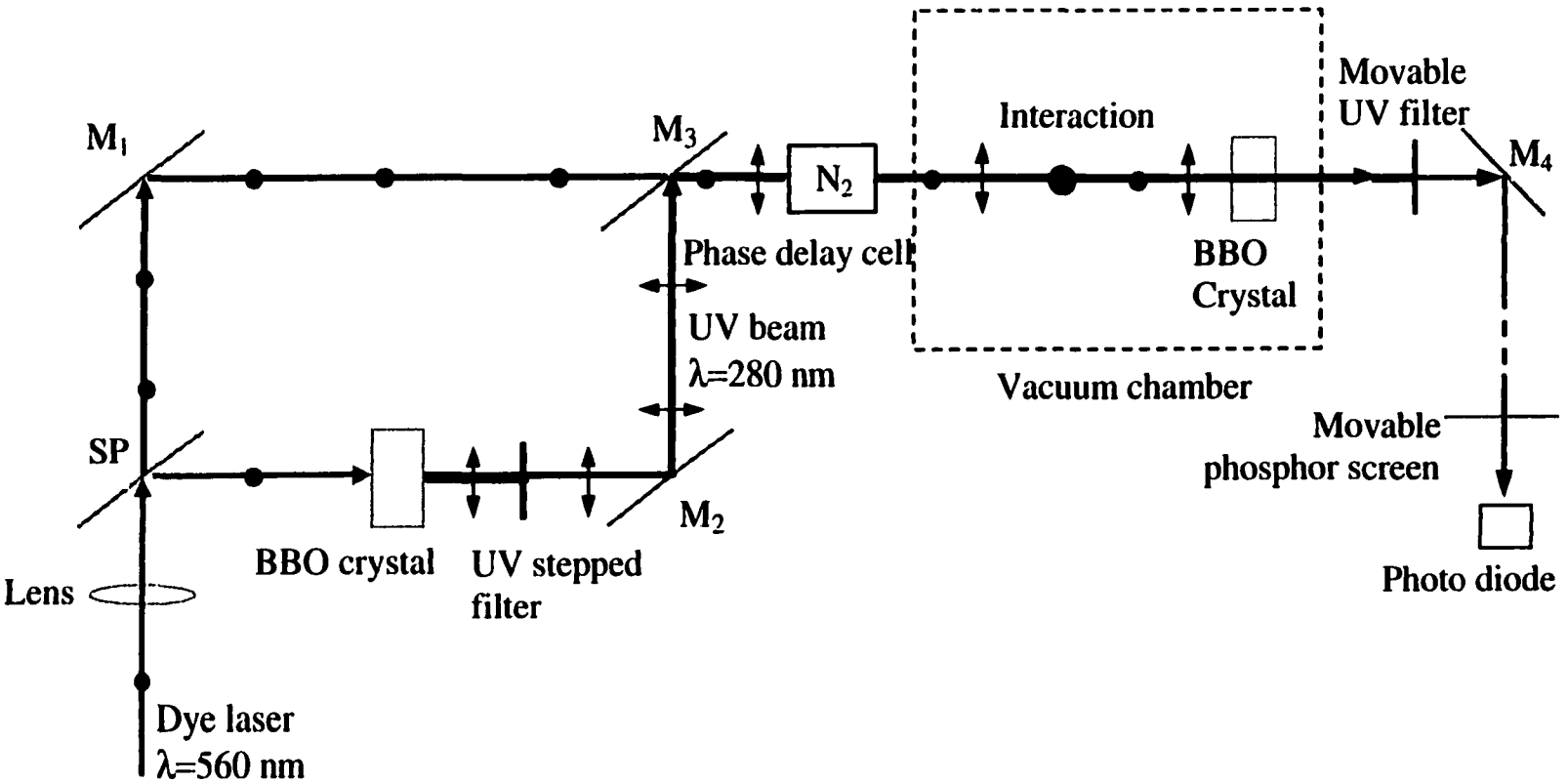

Figure 6.3: Schematic diagram of optical system for perpendicularly- polarized two-color field experiment.

beam from mirror M_1 at mirror M_3. This adjustment may need to be repeated many times until the interference fringes appear on one surface (towards the mirror M_2) of mirror M_3. Then we adjust mirror M_3 until the interference fringes between the two visible beams appear on a screen three meters away.

In order to measure the relative phase between the two perpendicularly-polarized optical fields, we insert a second BBO crystal inside the vacuum chamber at a distance ~40 cm behind the interaction region. After passing through the interaction region, both the UV and visible beams pass through the second BBO crystal. The two UV beams and the visible beam emerging from the back window of the vacuum chamber pass through a UV filter, which absorbs the visible light. Then the two UV beams are projected onto a florescence screen. We carefully adjust the mirror M_3 to make the two UV beams overlapped. When the interference pattern (parallel fringes) between the two UV beams appears, we continue to adjust the mirror M_3 to make the spacing between the fringes larger and larger. When the intensity is uniform, the two beams are overlapped well enough for this experiment. We will describe our method for measuring the relative phase between the UV and visible beams in Sec. 6.3.3.

We placed a stepped density UV filter (density and transmission vary in eleven steps across the surface length) just after the first BBO to adjust the power of the UV beam. In addition, the two mirrors M_2 and M_3 are specified for high reflection at the wavelength of 280 nm, but only partially reflective at 560 nm. Therefore, after passing through the stepped filter and then being reflected by these mirrors, only a very small portion (it was measured to be 5 μJ) of the visible beam from this branch of the Mach-Zehnder interferometer remains. This is only 2.5×10^{-3} of the power of the visible beam used for the two-photon ionization process, and does not affect the ionization signal to any significant level.

It is necessary to note that the two optical path lengths of the UV beam and visible beam from the beam splitter SP to mirror M_3 must be very closely matched in order to obtain the interference using the nanosecond pulse laser. We can estimate how close they have to be matched by considering the coherence length of the laser. We measured the frequency bandwidth of the dye laser to be $\Delta\nu \approx 10$ GHz with a Fabry-Perot etalon. The coherence time is roughly equal to the reciprocal of the frequency bandwidth, i.e. $\Delta t \approx 1/\Delta\nu = 10^{-10}$ s. The coherence length of the laser is $\sim c\Delta t \approx 3$ cm, where c is the speed of light in vacuum. Therefore, in order to see clear interference between these two beams, the optical lengths of the two arms of the Mach-Zehnder interferometer must be matched at least to within 0.3 cm. We carefully adjusted the mirrors M_2 and M_3 to fulfill this condition.

6.3.2 The phase delay cell

We use a phase delay cell to control the relative optical phases of the two laser fields. The phase difference between the UV and visible fields can be changed by varying the N_2 pressure in the phase delay cell because the refractive index of N_2 varies with wavelength.

After passing through the delay cell, a laser beam with a wavelength λ will experience an additional phase shift

$$\phi_n = (n-1)\frac{2\pi L}{\lambda} \tag{6.6}$$

where n is the refractive index of nitrogen gas in the cell and L is the path length of the cell. On the other hand, by varying the pressure of the nitrogen gas, the phase of the light wave will undergo a shift

$$\phi_p = \frac{2\pi nL}{\lambda}\cdot\frac{\Delta P}{P_o} \tag{6.7}$$

where n is the refractive index at standard temperature and pressure (STP). After the UV and visible laser beams pass through the cell, the phase difference between the two fields will be

$$\Delta(2\phi_{vis} - \phi_{uv}) = \frac{4\pi L(n_{vis} - n_{uv})}{\lambda} \cdot \frac{\Delta P}{P_o} \tag{6.8}$$

where ΔP is the pressure change of the nitrogen, n_{vis} and n_{uv} are refractive indices at 560 nm and 280 nm at STP, respectively, λ=560 nm, P_0 is the pressure of the standard atmosphere, and L is the path length of the cell, which is 13 cm long in our experiment. For pure nitrogen, $n_{uv} - n_{vis} = 1.617\times10^{-5}$. According to Eq. (6.8), a 2π phase shift requires a change of 101.2 Torr nitrogen pressure in the delay cell.

The cell is made of a stainless steel 4-way cross with ConFlat flanges and two pieces of fused silica windows. Before filling the Nitrogen gas, we pump the cell to ~3×10^{-2} Torr by a mechanical pump. Either the vacuum pressure or the nitrogen pressure in the cell is measured by a Terranova Convection Gauge Controller (Model 906) with a Granville-Phillips CONVECTRON gauge, whose measurement range is from 0.1 mTorr to 995 Torr for air and nitrogen.

6.3.3 Measurement of the phase difference between the UV and visible fields

In this section we describe the method we used to measure the relative phase between the UV and the visible beams, using a second BBO crystal inside the vacuum chamber.

Assuming that the frequencies of fundamental and second harmonic waves are ω_1 and ω_2 and the wave vectors are $\vec{k}_1, \vec{k}_2$, then the phase mismatch is

$$\Delta\vec{k} = 2\vec{k}_1 - \vec{k}_2 = \frac{4\pi}{\lambda_1}[n(\omega_1) - n(\omega_2)]. \qquad (6.9)$$

In the general case, the refractive index of a medium n is always a function of frequency (dispersion effect), i.e. $n(\omega_1) \neq n(\omega_2)$. In a special case, $\Delta\vec{k} = 2\vec{k}_1 - \vec{k}_2 = 0$, the phase matching condition between the fundamental and second harmonic waves in a non-linear crystal, we have $n(\omega_1) = n(\omega_2)$. Under this condition, the harmonic wave stays in phase with its driving wave. Once the relative phase between the two UV beams ϕ_{uv1}-ϕ_{uv2} ($\phi_{uv1}=\phi_{2\omega}$ and $\phi_{uv2}= 2\phi_{\omega}$) is measured, the phase difference between the first UV beam and the visible beam $\Delta\phi = \phi_{2\omega}$-$2\phi_{\omega}$ is obtained. We measure the relative intensity of the interference pattern between the two UV beams using a photodiode. The photodiode is located ~45 cm from the second BBO crystal. We use a digital real-time oscilloscope interfaced to a PC to record the photodiode signal. We record 14 sets of waveforms with 14 different pressures, corresponding to 14 image data, each set for one image data. The oscilloscope has a function to store multi-waveforms of signals on a single data waveform sheet. Two examples of the waveform signal are shown in Fig. 6.4a. Fig. 6.4b shows all the 14 data sheets. By using drag and drop mouse operations the data stored in the waveform sheet can be copied to a tabular sheet for processing. We record four signals on each waveform sheet and take the average value of the four amplitudes as the intensity at each pressure. The figures also show the width of the UV light pulse width, which is about 6 ns.

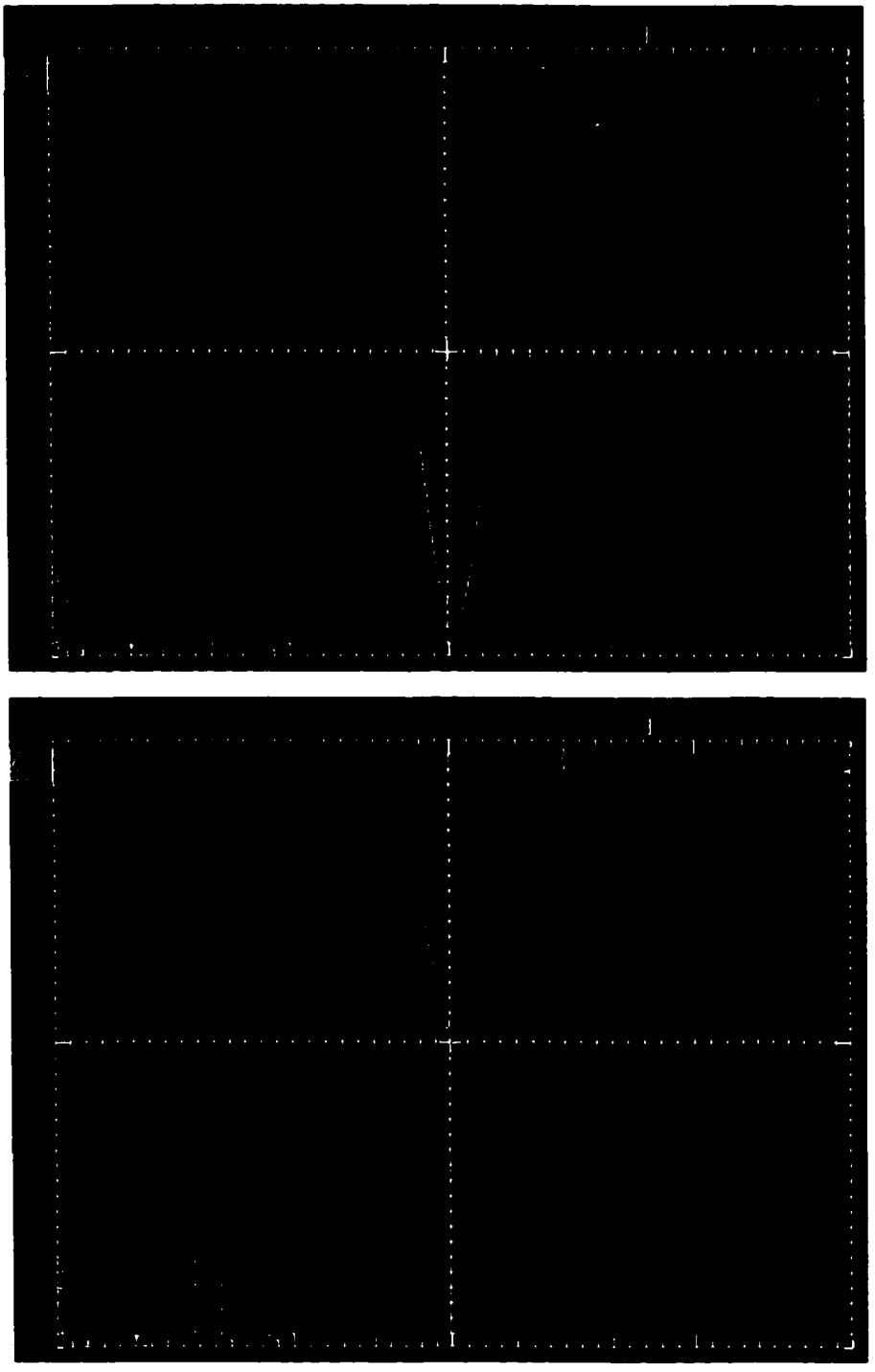

Figure 6.4a: Two examples of waveform sheets. Four signals are recorded in each waveform sheet during the 5 minute period of taking one image data. The amplitude of the interference signal between the two UV beams varies with varying the N_2 pressure or the relative optical phase.

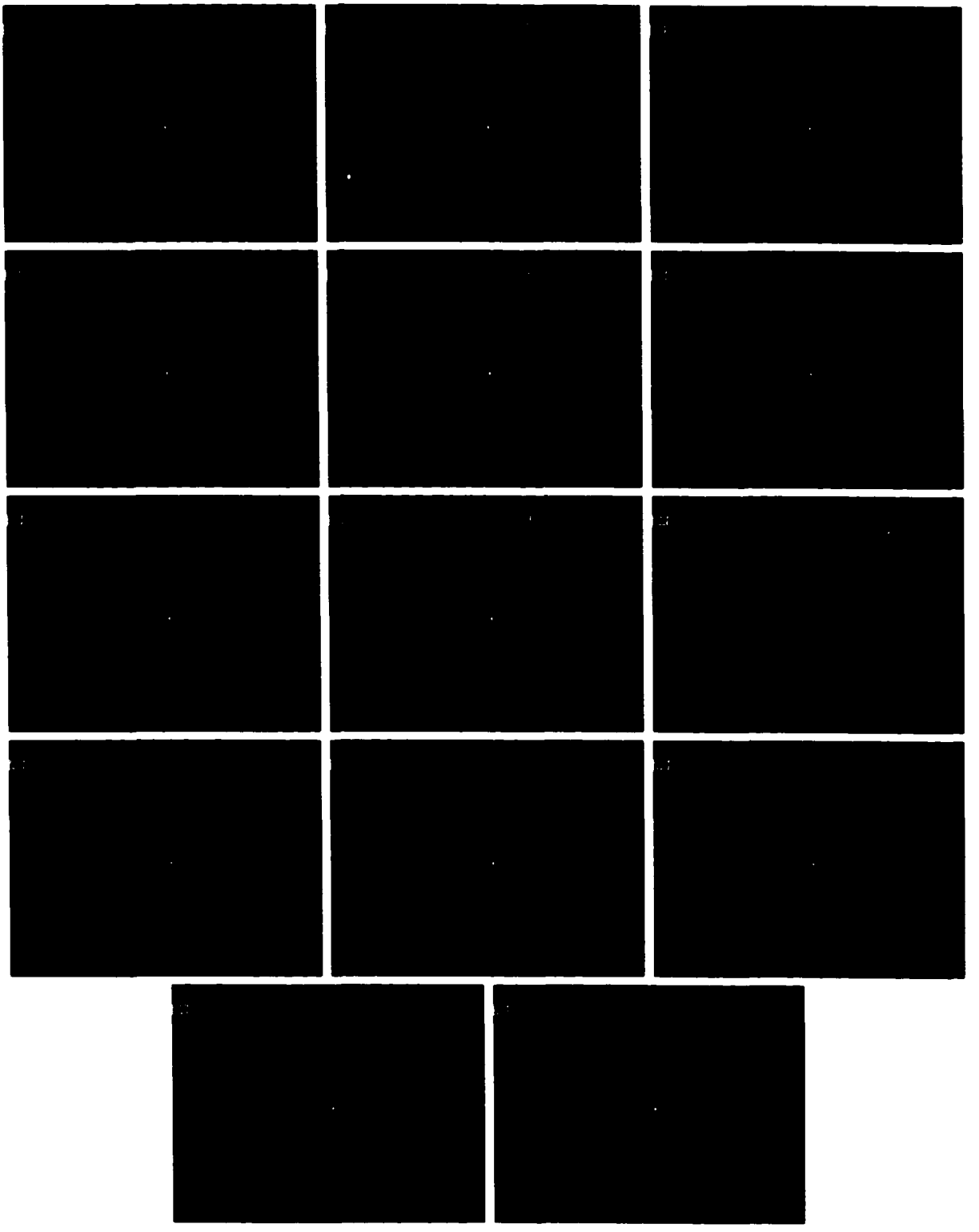

Figure 6.4b. The interference signal of the two UV beams varies with the N_2 pressure in the delay cell. Each wave sheet has 4 signals.

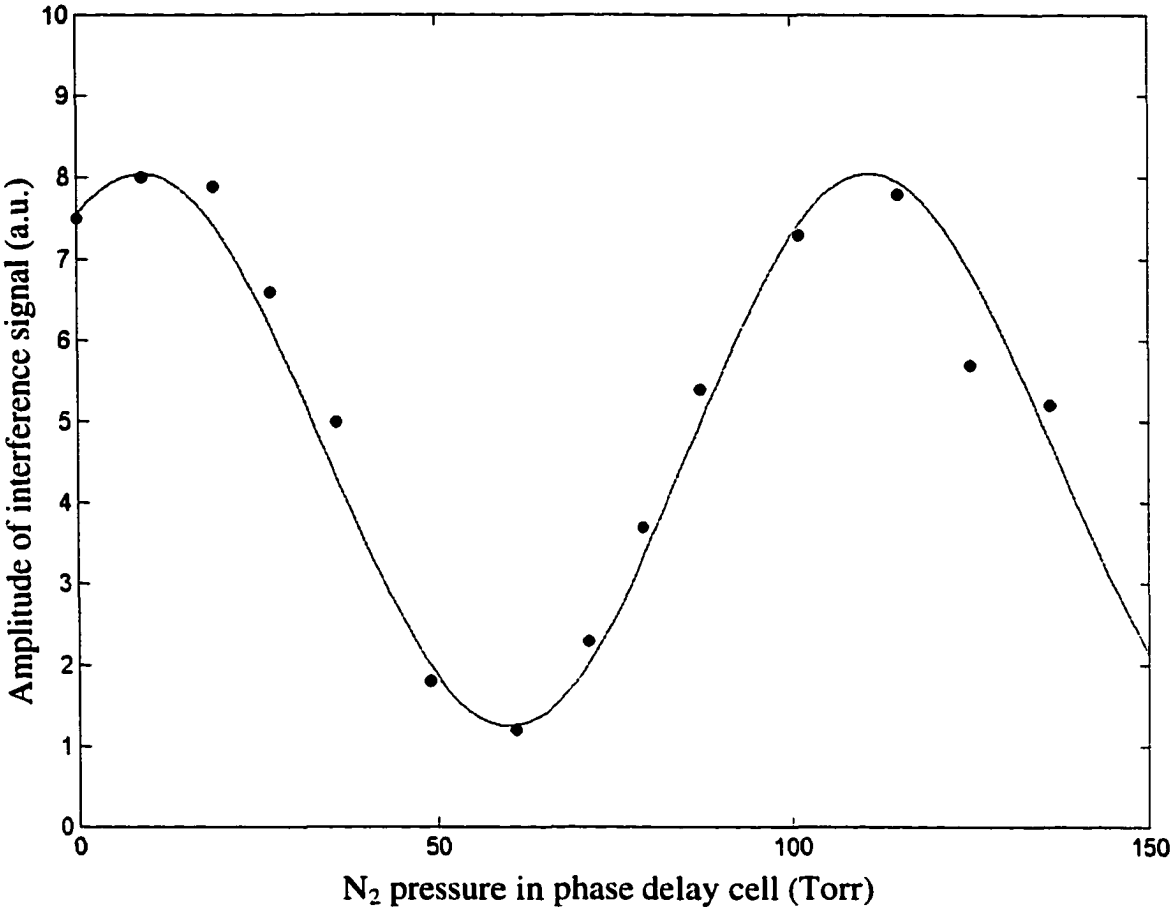

Figure 6.5: Amplitude of the interference signal between the two UV beams versus N_2 pressure in the phase delay cell. The solid line is the fit to the data points. The optical phase difference ϕ_{uv1}-ϕ_{uv2} (ϕ_{uv2}=$\phi_{2\omega}$), and hence $\phi_{2\omega}$-$2\phi_{\omega}$ for each N_2 pressure can be obtained from the fitting procedure.

The intensity of the interference signal between the two UV beams as a function of the pressure in the N_2 delay cell is plotted in Fig. 6.5. The solid curve is the best fit to the data points. We see from these figures that the intensity of the interference signal varies sinusoidally as the N_2 pressure is changed. We calculate the relative optical phases of the two UV beams, $\Delta\phi_{uv} = \phi_{uv1}-\phi_{uv2}$, ($\phi_{uv1}=\phi_{2\omega}$, $\phi_{uv2}=2\phi_{\omega}$) according to the best fit curve shown in Fig.6.5. We fit the cosine wave equation

$$A = B + C\cos(\frac{2\pi}{T_p}p + D) \tag{6.10}$$

to the data points in Fig. 6.5 to find the parameters B, C, T_p and D, where T_p is the N_2 pressure change corresponding to one cycle (2π radian) of this curve, p is the N_2 pressure in the delay cell and D is the initial phase when the pressure is zero torr. The best fitting values for these parameters are B = 4.65, C = 3.41, D = 0.175π and T_p = 102 Torr, which is in good agreement with the calculated value 101.2 Torr. The phase difference $\Delta\phi_{uv}$ is equal to the phase difference between the first UV beam and visible beam $\Delta\phi = \phi_{2\omega}-2\phi_{\omega}$.

The interference of the two UV beams can be expressed mathematically. Assuming that the electric fields of the two UV beams at that point are expressed as $E_1 = E_{10}e^{-i(\omega t-\phi_{uv1})}$ and $E_2 = E_{20}e^{-i(\omega t-\phi_{uv2})}$, respectively, the total intensity is the square of the resultant amplitude of the two fields,

$$\begin{aligned} I &= |E_1 + E_2|^2 \\ &= (E_{10}e^{-i(\omega t-\phi_{uv1})} + E_{20}e^{-i(\omega t-\phi_{uv2})})(E_{10}e^{+i(\omega t-\phi_{uv1})} + E_{20}e^{+i(\omega t-\phi_{uv2})}) \\ &= E_{10}^2 + E_{20}^2 + E_{10}E_{20}e^{-i\Delta\phi_{uv}} + E_{10}E_{20}e^{+i\Delta\phi_{uv}} \\ &= E_{10}^2 + E_{20}^2 + 2E_{10}E_{20}\cos(\Delta\phi_{uv}) \\ &= I_1 + I_2 + 2\sqrt{I_1 I_2}\cos(\Delta\phi_{uv}), \end{aligned} \tag{6.11}$$

6.3.4 Conditions and procedure of experiments

In this experiment, we pass the coaxial UV beam and visible beam into the vacuum chamber. The two-color beam crosses a beam of atomic rubidium to drive a one-photon and two-photon processes concurrently, resulting in the interference between the two channels. In order to match the ratio of the power of the UV beam and the visible beam we insert a stepped filter to adjust the power of the UV beam. The energies of the UV beam and the visible beam before entering the vacuum chamber were 12 μJ and 2 mJ, respectively, for this experiment.

We use our newly-developed photoelectron detector, which has been described in detail in Sec. 3.2 (refer to Fig. 3.1), to measure the angular distributions. Briefly, it is a dual-Micro-Channel Plate (MCP) with a phosphor screen sitting on the top of a pair of parallel field plates, which are made of fine mesh. The distance between the two meshes is 1.35 cm, and the interaction region is 0.55 cm from the upper mesh. For these experiments, the voltage between the two field meshes was set to be 1.4 Volts and the voltage on the MCP assembly was V_a=6000 Volts to the phosphor screen and V_o=2000 Volts to the MCP, respectively; the photoelectrons ejected from the atoms accelerate toward the upper mesh. After transmitting through the mesh, the electrons are further accelerated onto the MCP multiplier, which provides an electron gain of ~10^6. The burst of photoelectrons strikes the phosphor screen producing a bright spot. The image is recorded by a CCD camera and stored in a laboratory PC.

While taking data, we use the threshold detection scheme to decrease the influence of any gain non-uniformities of the MCP, the phosphor screen, or the CCD array in the camera. We adjust the laser power (both UV and visible) to limit the number of photoelectrons collected by the detector for each laser shot to avoid the overlap of the electrons on the phosphor screen on the MCP. As we mentioned in Sec. 3.4, the gain and offset of the video input amplifier can be adjusted by setting the lower and upper voltages of the video input, we set the

voltage levels as 23/40. Under the conditions of our experiment, approximately 30 electrons were recorded for each laser pulse, and each electron is recorded independently. We recorded composite images with an accumulation of 3000 laser shots for each. During the 5 minute period for taking each image at a specific N_2 pressure in the delay cell, we measured the intensity of the interference signal of the two UV beams as mentioned earlier.

6.3.5 Ratio of beam sizes and phase matching condition of UV and visible beams

In the case of the two-color ionization process, the ratio of the beam sizes between UV and visible beams and how well the two beams are overlapped play an important role in quantum interference. In this section we give quantitative analyses to these issues. We have given an expression for the total transition rate in Eq. (6.5). Here we are only concerned with how the two fields affect the transition rate. For this purpose we rewrite the equation (6.5) as the following simple form with two fields E^{uv} and E^{vis}

$$W_{1,2} \propto \left|\mu_1 E^{uv} + \mu_2 (E^{vis})^2\right|^2, \tag{6.14}$$

where μ_1, μ_2 are the transition moments for one- and two-photon processes, which are just $O_{ij}^{(1)}$ and $T_{ij}^{(33)}$ in Eq. (6.5), respectively. E^{uv} and E^{vis} are $E^{2\omega}$ and E^{ω} in Eq. (6.5), respectively, but including phase. We omit all the constants to simplify the expressions. For the lowest Gaussion mode propagating along the $\hat{y}$ axis, the fields can be written as

$$E^{uv} = E_0^{uv} e^{-\frac{r_t^2}{w_{uv}^2(y)}} e^{i\vec{k}_{uv}\cdot\vec{r}} e^{i\phi_{uv}}, \tag{6.15}$$

$$E^{vis} = E_0^{vis} e^{-\frac{r_t^2}{w_{vis}^2(y)}} e^{i\vec{k}_{vis}\cdot\vec{r}} e^{i\phi_{vis}}, \tag{6.16}$$

where ϕ_{uv}, ϕ_{vis} are the phases for each individual field, r_t is a transverse radial coordinate on the x-z plane, $\vec{r}$ is the position vector, $w_{uv}(y)$ and $w_{vis}(y)$ are the radii of the two beams, and $\vec{k}_{uv}, \vec{k}_{vis}$ are the wave vectors of the two fields, whose directions are close to $\hat{y}$.

Combining Eqs. (6.14), (6.15) and (6.16), and using w_{uv} and w_{vis} as the radii of the two beams at the interaction region, the total transition rate can be written as the following form

$$\begin{aligned} W_{1,2} &\propto \left| \mu_1 E_0^{uv} e^{-\frac{r_t^2}{w_{uv}^2}} e^{i\vec{k}_{uv}\cdot\vec{r}} e^{i\phi_{uv}} + \mu_2 (E_0^{vis} e^{-\frac{r_t^2}{w_{vis}^2}} e^{i\vec{k}_{vis}\cdot\vec{r}} e^{i\phi_{vis}})^2 \right|^2 \\ &= \left[\mu_1^2 (E_0^{uv})^2 e^{-\frac{2r_t^2}{w_{uv}^2}} + \mu_2^2 (E_0^{vis})^4 e^{-\frac{4r_t^2}{w_{vis}^2}} \right] \\ &\quad + \left[\mu_1 \mu_2 E_0^{uv} (E_0^{vis})^2 e^{-\left(\frac{1}{w_{uv}^2}+\frac{2}{w_{vis}^2}\right) r^2} e^{i(\vec{k}_{uv}-2\vec{k}_{vis})\cdot\vec{r}} e^{-i(2\phi_{vis}-\phi_{uv})} + c.c. \right] \\ &= A + 2B\cos\left[\left(\vec{k}_{uv} - 2\vec{k}_{vis}\right)\cdot\vec{r} + (2\phi_{vis} - \phi_{uv}) \right] \end{aligned} \tag{6.17}$$

where

$$A = \mu_1^2 (E_0^{uv})^2 e^{-\frac{2r_t^2}{w_{uv}^2}} + \mu_2^2 (E_0^{vis})^4 e^{-\frac{4r_t^2}{w_{vis}^2}} \tag{6.18}$$

$$B = \mu_1 \mu_2 E_0^{uv} (E_0^{vis})^2 e^{-\left(\frac{1}{w_{uv}^2}+\frac{2}{w_{vis}^2}\right) r_t^2} \tag{6.19}$$

From these equations we see that there are two important conditions to be satisfied for observing the interference between these two fields:

The first one concerns the ratio of the beam sizes of the UV and visible light. From these equations we see that in order for the UV and visible fields to maintain the same contribution to the ionization process at every point of a transverse plane we must have

$$w_{uv} = \frac{w_{vis}}{\sqrt{2}}. \tag{6.20}$$

Fortunately, the spot sizes of the second harmonic and fundamental waves at the first BBO crystal satisfy this relation. For the lowest Gaussian mode of the laser beam, the intensity of the two fields can be written as

$$I_{vis}(r) = I_0 e^{-\frac{2r_t^2}{w_{vis}^2}} \quad \text{and} \tag{6.21}$$

$$I_{uv}(r) = \beta I_{vis}^2(r) = \beta I_0^2 e^{-\frac{4r_t^2}{w_{vis}^2}} \tag{5.22}$$

where β is a coefficient, and w_{vis} is the radius of the fundamental visible beam. So the spot size of the second harmonic beam is $\frac{w_{vis}}{\sqrt{2}}$ as expressed.

The second condition concerns the directions of the $\vec{k}$ vectors of the two beams. The term $(\vec{k}_{uv} - 2\vec{k}_{vis}) \cdot \vec{r}$ will cause an additional phase shift in the relative phase. In order to obtain the maximum interference $\Delta\vec{k}$ should be equal to zero, i.e. $\Delta\vec{k} = (\vec{k}_{uv} - 2\vec{k}_{vis}) = 0$. In the following we evaluate the maximum Δk in this experiment.

We first qualitatively estimate the upper bound of the angle between the two beams. In Fig. 6.6, the radius of the beam size is w and s is the maximum distance

between the two wave fronts. The maximum phase shift due to the non-zero angle α is

$$\Delta\phi_{\vec{k}} = s \cdot \frac{2\pi}{\lambda_{vis}} \approx \alpha w \frac{2\pi}{\lambda_{vis}}. \tag{6.23}$$

If we let $\Delta\phi_{\vec{k}} = 0.1\pi$, $w = 0.5$ mm, and $\lambda_{vis} = 560$ nm, then the upper bound of the angle between the two laser beams is evaluated to be $\alpha \approx 5.6\times10^{-2}$ mrad.

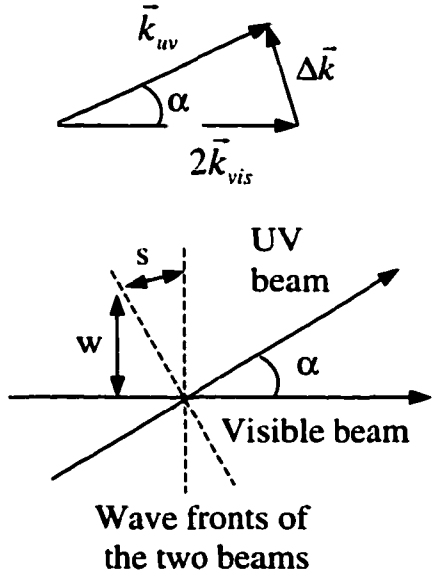

Figure 6.6: The relation of the wave vectors and wave fronts between the UV and visible beams

We can also determine the upper bound of the angle between the two beams in a more rigorous manner. Integrating Eq. (6.17) over the interaction region

$$I=\int\left(\mu_1^2(E_0^{uv})^2 e^{\frac{2r_t^2}{w_{uv}^2}}+\mu_2^2(E_0^{vis})^4 e^{\frac{4r_t^2}{w_{vis}^2}}\right)rdrd\varphi dy$$

$$+\int\left[\mu_1\mu_2 E_0^{uv}(E_0^{vis})^2 e^{-\left(\frac{1}{w_{uv}^2}+\frac{2}{w_{vis}^2}\right)r_t^2} e^{-i(\vec{k}_{uv}-2\vec{k}_{vis})\cdot\vec{r}} e^{-i(2\phi_{vis}-\phi_{uv})}+c.c.\right]dxdydz \qquad (6.24)$$

For the first integral, we have

$$I_1 = 2\pi l_y\left(\mu_1^2(E_0^{uv})^2\cdot\frac{w_{uv}^2}{4}+\mu_2^2(E_0^{vis})^4\cdot\frac{w_{vis}^2}{8}\right)$$

where l_y is the length of the interaction range along y axis.

If we set $\Delta\vec{k}=(\vec{k}_{uv}-2\vec{k}_{vis})$ in x direction as shown in Fig. 6.7, then for the second integral in Eq. 6.24, we have

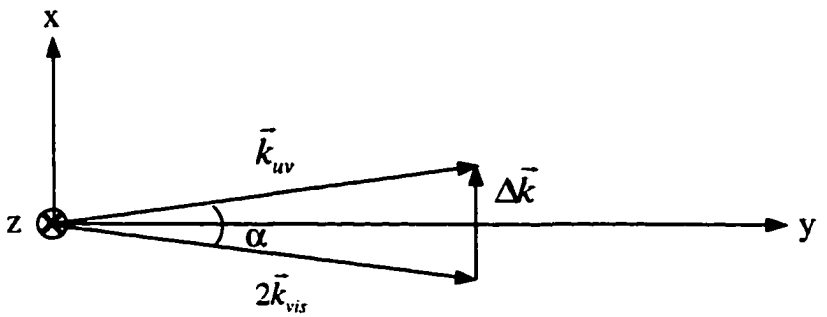

Figure 6.7: Wave vectors and coordinate system

$$I_2 = \int \left[\mu_1 \mu_2 E_0^{uv} (E_0^{vis})^2 e^{-\left(\frac{1}{w_{uv}^2}+\frac{2}{w_{vis}^2}\right)(x^2+z^2)} e^{i\Delta kx} e^{-i(2\phi_{vis}-\phi_{uv})} + c.c. \right] dxdydz$$

This integral is separable in x, y and z coordinates as the following three integrals:

$$I_{2x} = \int_{-\infty}^{+\infty} \left[e^{-\left(\frac{1}{w_{uv}^2}+\frac{2}{w_{vis}^2}\right)x^2} e^{i\Delta kx} e^{-i(2\phi_{vis}-\phi_{uv})} + c.c. \right] dx$$

$$= 2\int_{-\infty}^{+\infty} e^{-\left(\frac{1}{w_{uv}^2}+\frac{2}{w_{vis}^2}\right)x^2} \cos(\Delta kx + \Delta\phi) dx$$

$$= 2\sqrt{\pi}\left(\frac{1}{w_{uv}^2}+\frac{2}{w_{vis}^2}\right)^{-\frac{1}{2}} e^{-\frac{1}{4}\left(\frac{1}{w_{uv}^2}+\frac{2}{w_{vis}^2}\right)^{-1}(\Delta k)^2} \cos\Delta\phi$$

$$I_{2y} = \mu_1 \mu_2 E_0^{uv} (E_0^{vis})^2 \int dy$$

$$= l_y \mu_1 \mu_2 E_0^{uv} (E_0^{vis})^2$$

$$I_{2z} = \int_{-\infty}^{+\infty} e^{-\left(\frac{1}{w_{uv}^2}+\frac{2}{w_{vis}^2}\right)z^2} dz$$

$$= \sqrt{\pi}\left(\frac{1}{w_{uv}^2}+\frac{2}{w_{vis}^2}\right)^{-\frac{1}{2}}$$

Finally we obtain

$$I = 2\pi l_y \left(\mu_1^2 (E_0^{uv})^2 \frac{w_{uv}^2}{4} + \mu_2^2 (E_0^{vis})^4 \frac{w_{vis}^2}{8} \right)$$

$$+ 2\pi l_y \mu_1 \mu_2 E_0^{uv} (E_0^{vis})^2 \left(\frac{1}{w_{uv}^2}+\frac{2}{w_{vis}^2}\right)^{-1} e^{-\frac{1}{4}\left(\frac{1}{w_{uv}^2}+\frac{2}{w_{vis}^2}\right)^{-1}(\Delta k)^2} \cos(2\phi_{vis} - \phi_{uv}) \quad (6.25)$$

In order to observe the interference clearly we set the following condition

$$e^{-\frac{1}{4}\left(\frac{1}{w_{uv}^2}+\frac{2}{w_{vis}^2}\right)^{-1}(\Delta k)^2} \geq 90\%$$

or

$$-\frac{1}{4}\left(\frac{1}{w_{uv}^2}+\frac{2}{w_{vis}^2}\right)^{-1}(\Delta k)^2 \geq \ln(0.9)$$

The radius of the beam size at the interaction region is about $w_{uv}=\frac{w_{vis}}{\sqrt{2}}=0.5\,\text{mm}$. we have the condition $\Delta k \leq 1.84\times 10^3\ \text{m}^{-1}$. Referring to Fig. 6.7, $\alpha \approx \Delta k/k_{uv} \leq (1.84\times10^3)/(2\pi/280\times10^{-9}) = 8\times10^{-5}$ rad $= 8\times10^{-2}$ mrad. This estimation is consistent with what we just made above using the qualitative method and Fig. 6.6.

6.4 Results and analyses

6.4.1 Images obtained from perpendicularly-polarized two-color laser field

In this section we first show the images recorded by ionizing the rubidium atoms with only one frequency component of the laser field at a time. The five figures in the left column of Fig. 6.8 correspond to one-photon ionization with the horizontally–polarized UV light only; and the figures in the right column are produced from the two-photon ionization process by the vertically-polarized visible light alone. Fig. 6.8 (a1) and (a2) show the recorded images produced on the phosphor screen of the Micro-Channel Plate, Fig. 6.8 (b1) and (b2) are theoretically calculated images based on the experimental conditions for comparison with the recorded images. Fig. 6.8 (c1) and (c2) are mesh plots of the image data, which are smoothed somewhat by averaging each pixel value with its adjacent pixels. Fig. 6.8 (d1) and (d2) show the data fit with the calculated images from the central rows of images (a1) (b1) and (a2) (b2), respectively. We also plot the corresponding angular distributions of the photoelectrons on Fig. 6.8 (e1) and (e2).

From these figures we see that the images are symmetric in both the one and two-photon processes. When both the UV and visible light interact with the atoms, the images show asymmetry and vary with varying phase between the two fields. In order to see the changes clearly we show the mesh plots and the cross sections of these images in Fig. 6.9. The solid curve in each subplot of the right column is the cross sectional slice from the central row of each image. We obtained these image data by changing the N_2 pressure in the delay cell from 0 Torr to 136 Torr. We calculated the relative optical phase for each pressure based on the best fit of the amplitude of the two UV field interference signals versus the N_2 pressure as mentioned in Sec. 6.3.3. The phase and the pressure both are shown on each subplot. In Fig. 6.10 we plot three typical data images and the data from a single

Figure 6.8: Images recorded (a1) with the horizontally–polarized 280 nm UV light alone and (a2) with the vertically-polarized 560 nm visible light alone, (b1) and (b2) are the calculated images, (c1) and (c2) are mesh plots, (d1) and (d2) are the central row slice of the recorded data (dot) with the best fit curve of the calculated image (solid line) , (e1) and (e2) are the corresponding angular distributions which produce these images.

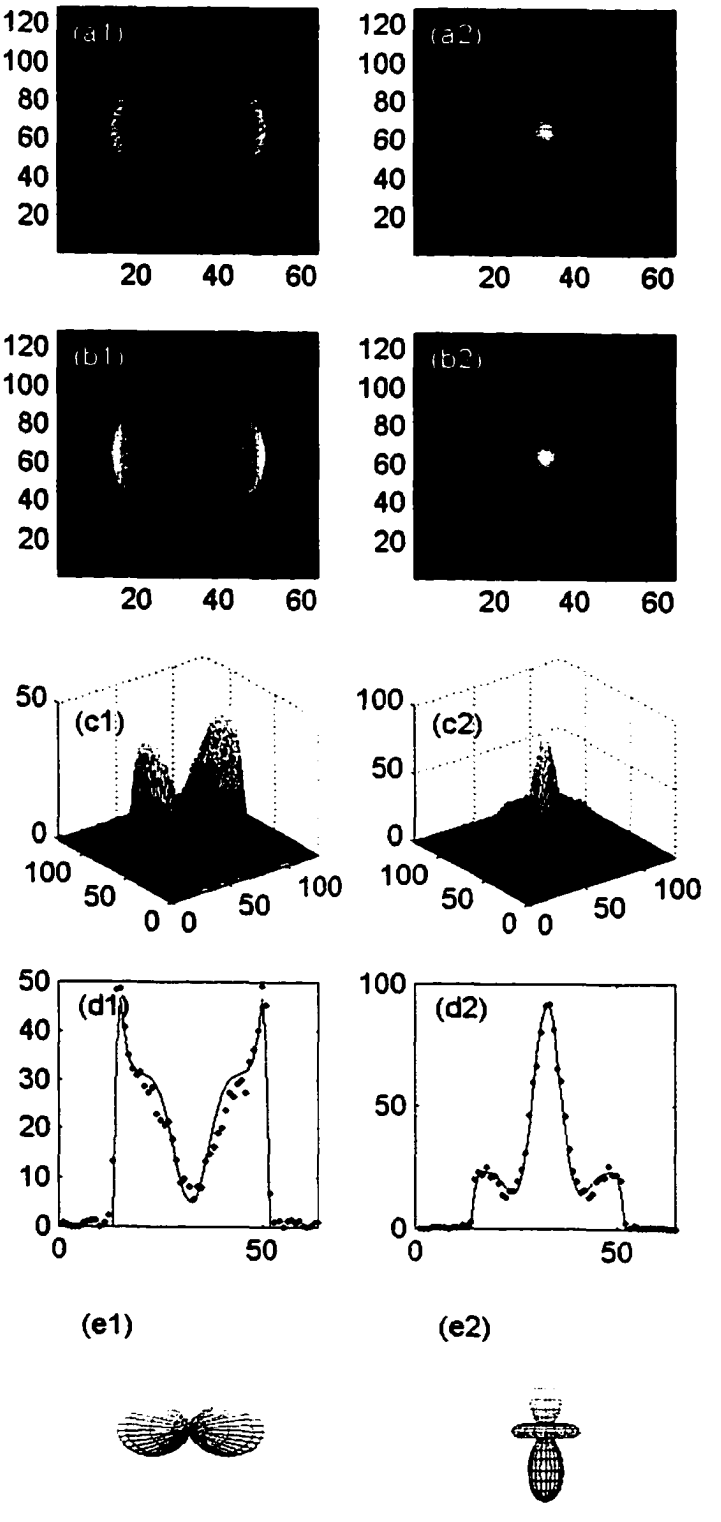

Figure 6.8

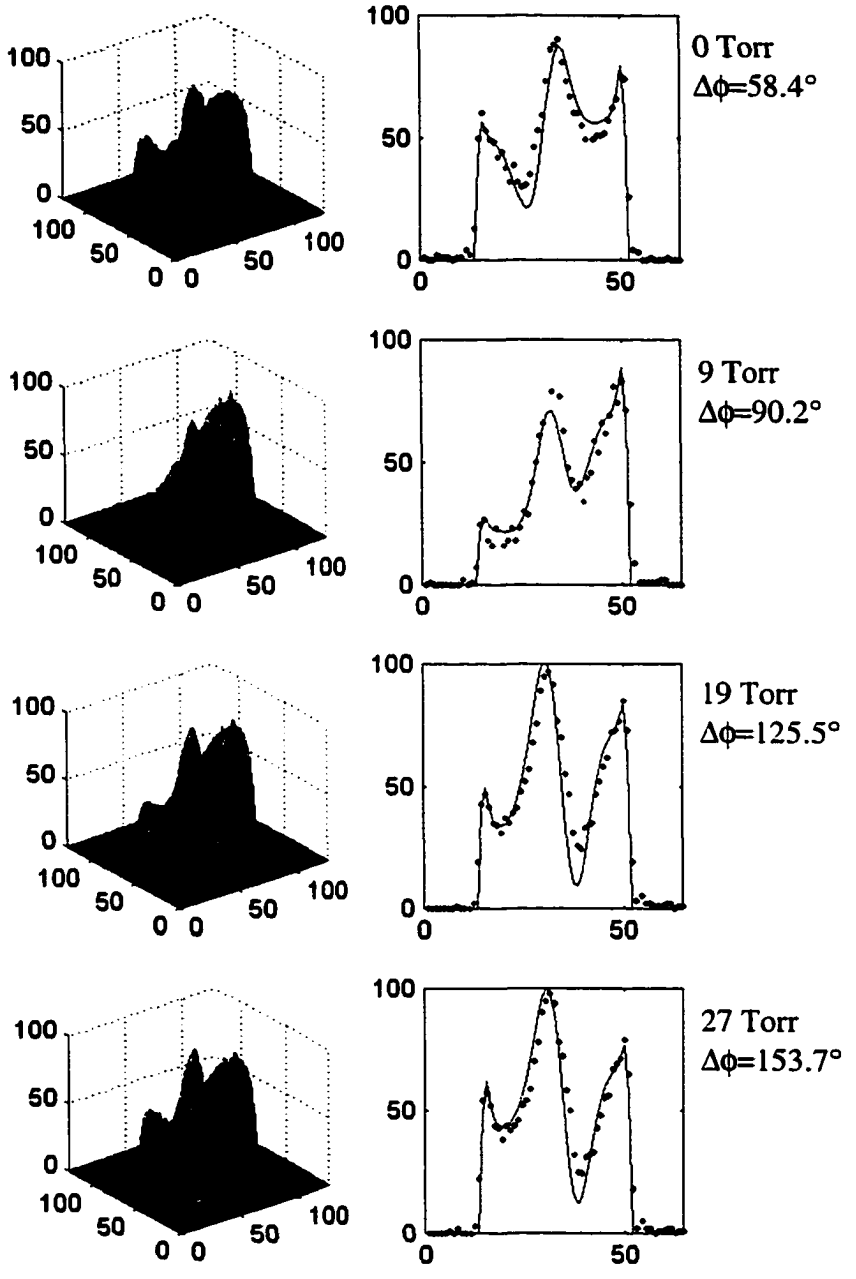

Figure 6.9: Mesh plots of the recorded images and the central row slices of the recorded data (dot) with the best fit curves of the calculated images (solid lines). Images are taken by perpendicularly-polarized two-color fields. The asymmetric electron angular distributions vary with varying the N_2 pressure. $\Delta\phi$ is the optical phase difference of the two laser fields.

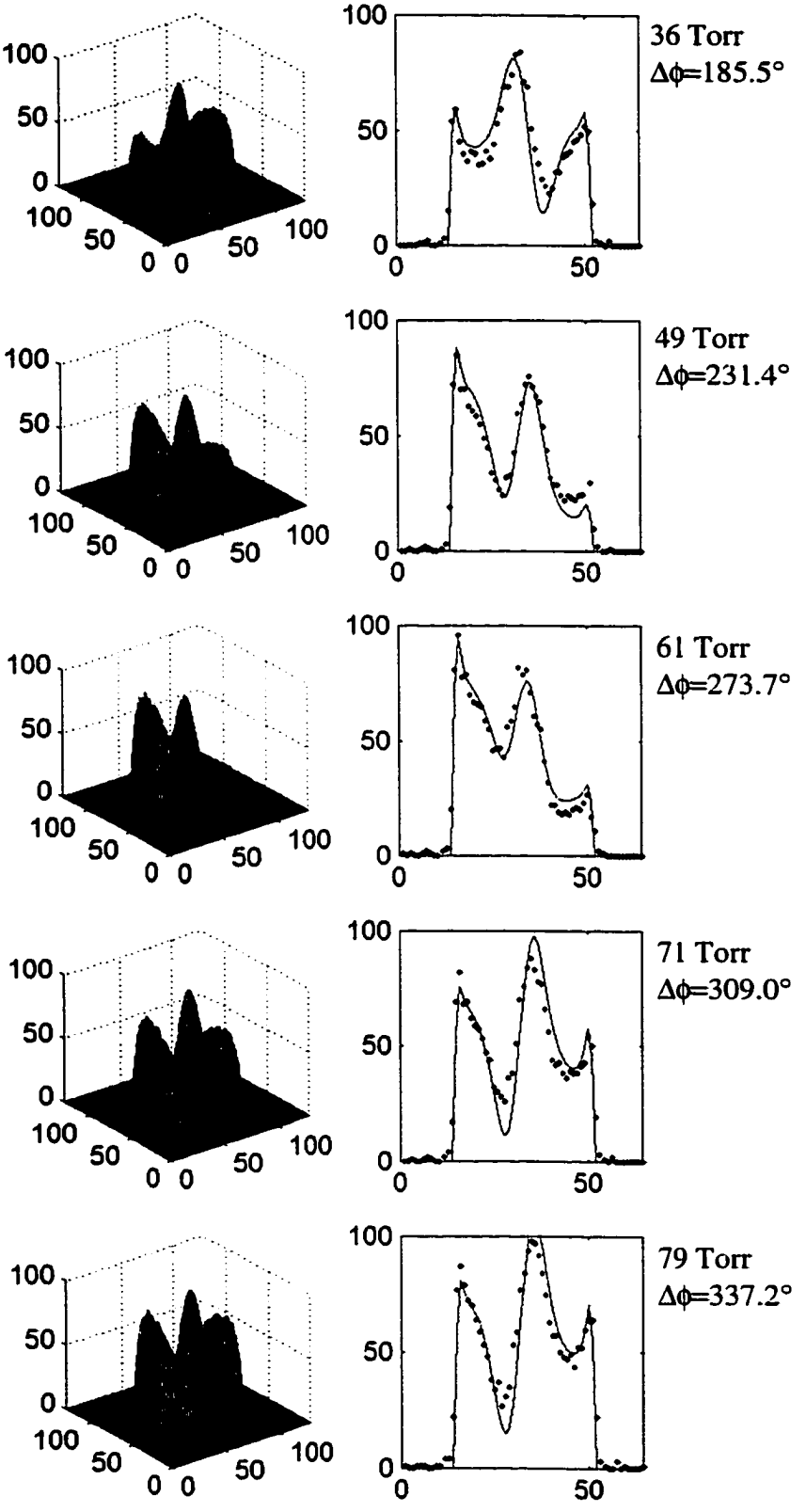

Figure 6.9: (continued)

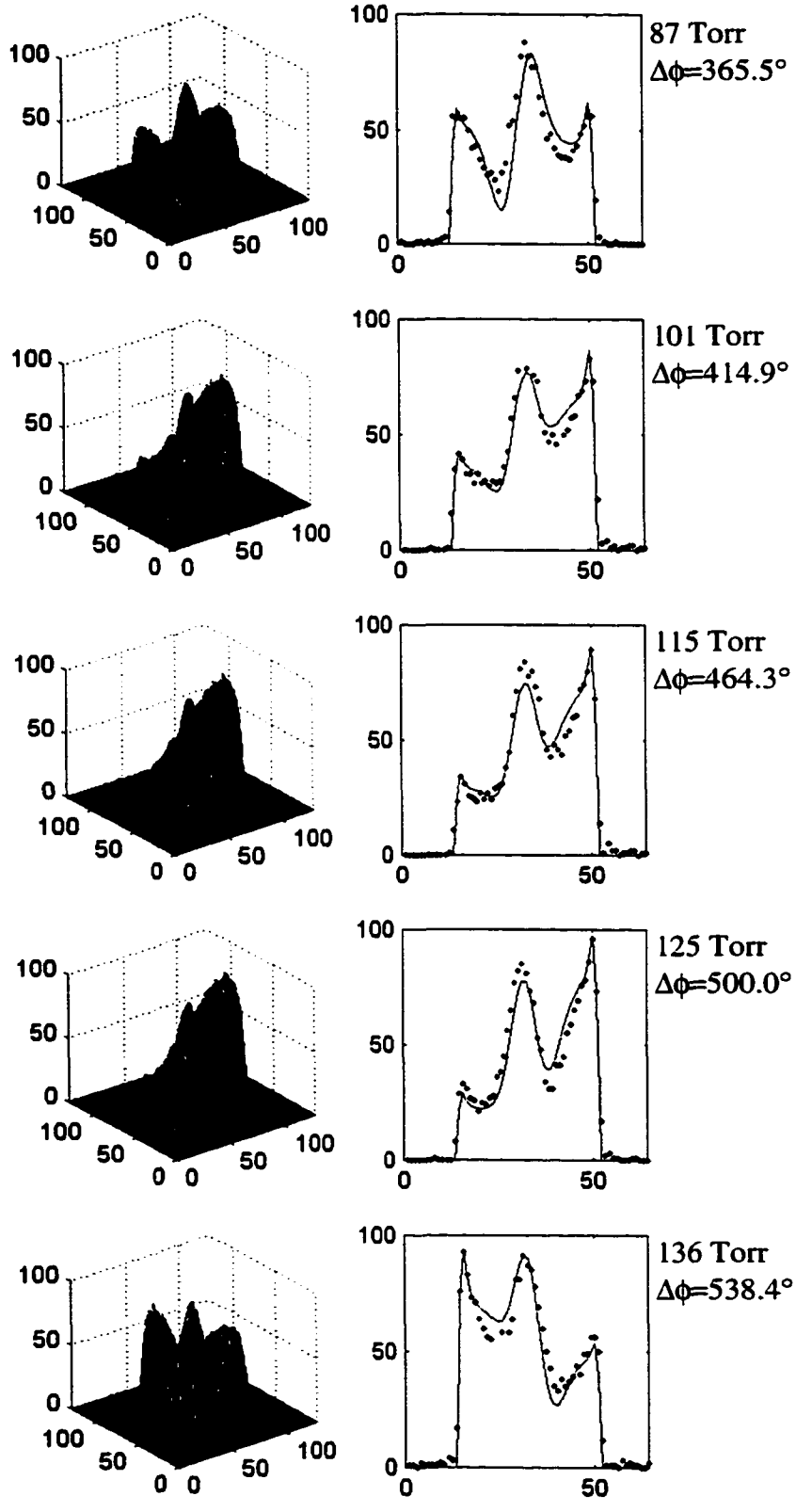

Figure 6.9: (continued)

Figure 6.10: Three recorded images (a1-a3) and theoretically calculated images (b1-b3) with three different pressures and phase differences showing on the top. The slices, from single rows 64 (c1-c3) and 81(d1-d3), show both the data points and the calculated image fit (solid lines). Images (a1) and (a3) were taken at an optical phase difference near π. They show the near maximum asymmetry in the opposite direction. Figs (e1) to (e3) are the corresponding angular distributions. Images taken by perpendicularly-polarized two-color fields (λ_1=560nm and λ_2=280nm)

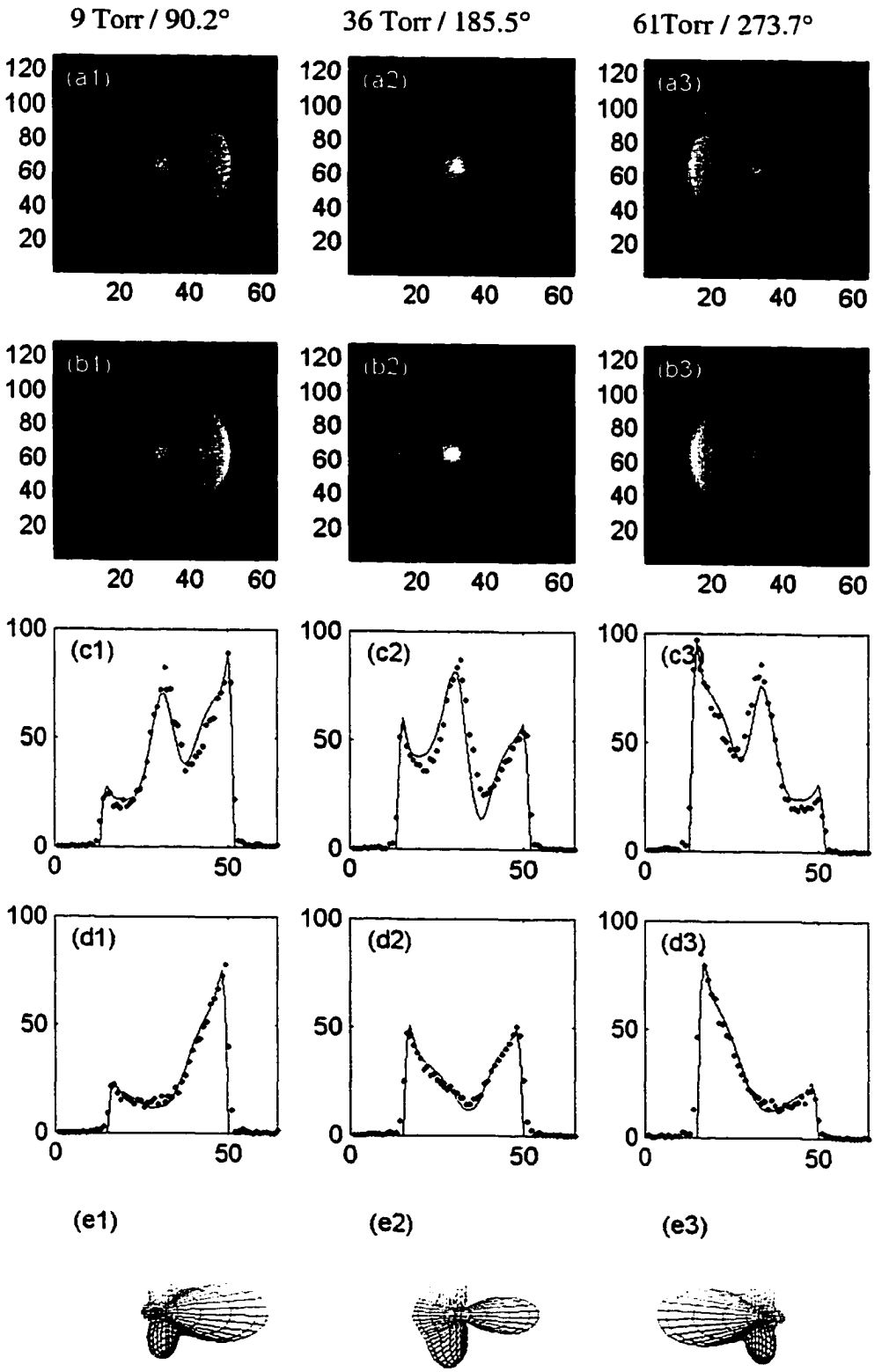

Figure 6.10

row, including both the experimental data points and the theoretical best fitting curves. Data in the first and third columns were collected at the optical phase difference that resulted in near maximally asymmetric distributions. The phase difference between these two data sets is nearly π, which results in opposite asymmetric distributions. The figures (c1) to (c3), are the cross section of the central row and the figures (d1) to (d3) are the slices at row 81. In each case the agreement between the experimental data (dots) and the best fit theoretical curve is very good.

6.4.2 Determination of the ratio of one-photon transition moments $R_{1/2}/R_{3/2}$

The angular distribution of photoelectrons induced by the one-photon ionization process with linearly-polarized light is described by [73]

$$\frac{d\sigma}{d\Omega} = \frac{\sigma_{tot}}{4\pi}[1 + \beta P_2(\cos\Theta)], \tag{6.25}$$

where β is the asymmetric parameter that characterizes the photoelectron angular distribution, Θ is the angle between the direction of light polarization and the direction of the photoelectron momentum, and $P_2(\cos\Theta)=(3\cos^2\Theta-1)/2$ is the second-order Legendre polynomial. The asymmetry parameter β can be written as [74]

$$\beta = 2\frac{R_{3/2}^2 + 2R_{1/2}R_{3/2}\cos(\delta_{3/2} - \delta_{1/2})}{2R_{3/2}^2 + R_{1/2}^2}, \tag{6.26}$$

where $R_{1/2,\ 3/2}$ are the one-photon transition moments for the transition $5s^2S_{1/2} \rightarrow \varepsilon^2P_{1/2,\ 3/2}$, and $\delta_{1/2,\ 3/2}$ are the phase shifts of the wave functions. The angular distribution for single photon ionization is determined only by the parameter β or by the ratio of $R_{1/2}/R_{3/2}$. The coefficient $\sigma_{tot}/4\pi$ only affects the overall amplitude of the signal. We adjusted the ratio $R_{1/2}/R_{3/2}$ to match the

calculated one-photon image with the measured image to yield the value, $R_{1/2}/R_{3/2}$ =1.96. This value is very close to the expected value based on a previous measurement with a different technique [75]. Since the spin orbit coupling has a small effect on δ, the $\delta_{3/2}$-$\delta_{1/2}$ is very small, based on the bound state experimental data [76], we estimated to be only 0.015π. We can set $\cos(\delta_{3/2}-\delta_{1/2})\approx 1$. According to Ref. [75], β=1.602 for the wavelength of 280.3 nm. From Eq. (6.26), this gives a value of $R_{1/2}/R_{3/2}$ to be 2.06.

6.4.3 Determination of phase difference between *p*- and *d*-continuum waves

In order to derive the phase difference between *p*- and *d*-continuum waves, we match the calculated two-color interference images with the measured images to yield the best fit by adjusting the relative phase $\Delta=\Delta\phi+\Delta\xi$, where $\Delta\phi=\phi_{2\omega}-2\phi_{\omega}$, the phase difference between the two optical fields and $\Delta\xi=\xi_p-\xi_d$, the atomic phase between the *p*- and *d*-continuum waves.

According to Eq. (6.5), the angular distribution is determined by the two-photon transition parameters, $S_{\bar{s}}/S_{\bar{d}}$, $S_{\Delta d}/S_{\bar{d}}$ and $\xi_s-\xi_d$, the ratio of one-photon transition moments, $R_{1/2}/R_{3/2}$ and the phase Δ. We use the two-photon parameters, $S_{\bar{s}}/S_{\bar{d}}=-0.42$, $S_{\Delta d}/S_{\bar{d}}=-0.36$ and $\xi_s-\xi_d=2.08$, obtained in our previous experiment (see Sec. 5.3) for the laser light at the wavelength of 560 nm, and the value 1.96 for the ratio $R_{1/2}/R_{3/2}$. We then adjust the phase Δ for the calculated images to determine the value that yields the best fit with experimentally-obtained images. We record fourteen images with fourteen different optical phases (i.e. fourteen different N_2 pressures). As we have described in Sec. 6.3.3, we first record the intensity of the interference signal between the two UV beams with 14 different N_2 pressures and we plot these data in Fig. 6.5. Then we calculate the relative optical phases $\phi=\phi_{2\omega}-2\phi_{\omega}$, based on the best fit curve shown in Fig. 6.5. In Fig. 6.11 we plot the total phase difference

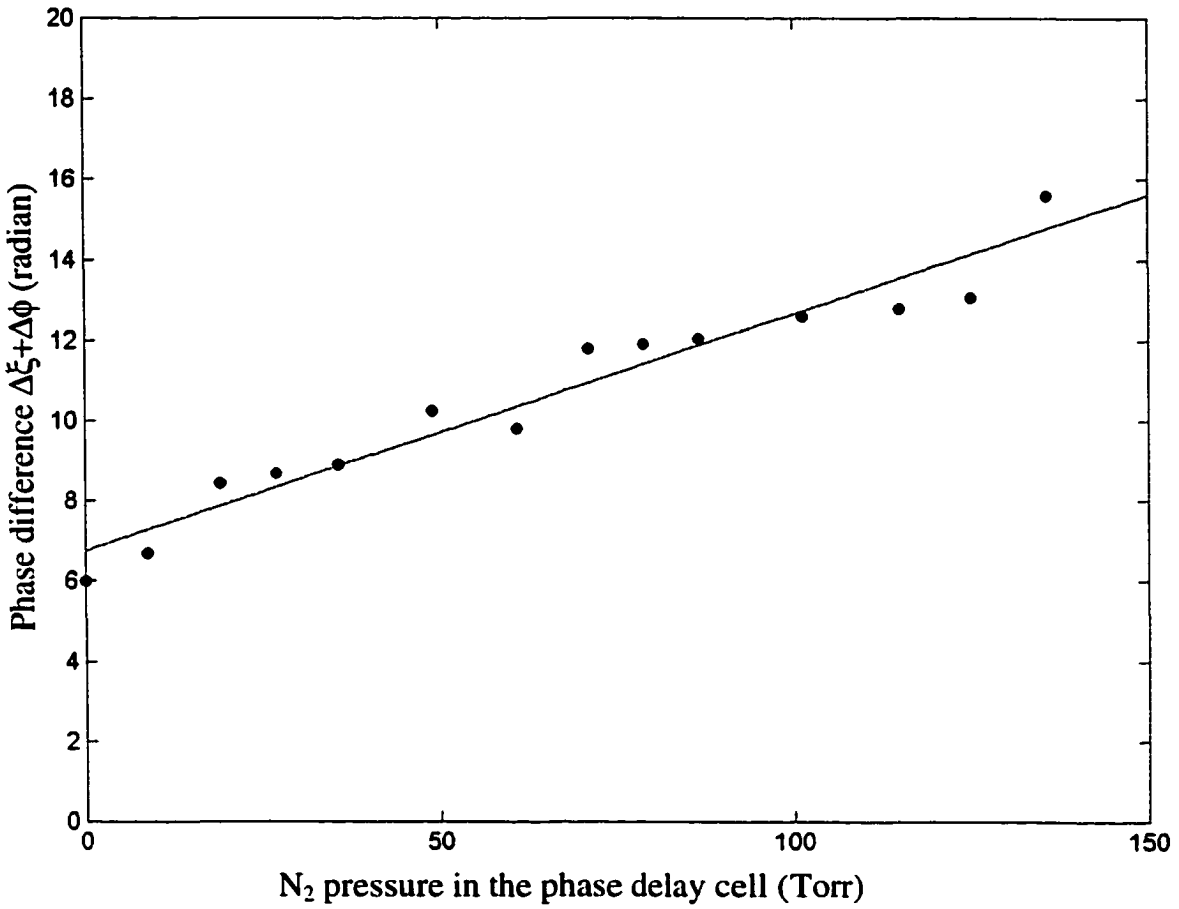

Figure 6.11: The phase difference between the partial waves, $\Delta\xi+\Delta\phi$, versus N_2 pressure in phase delay cell. The solid line is the best fit to the data points.

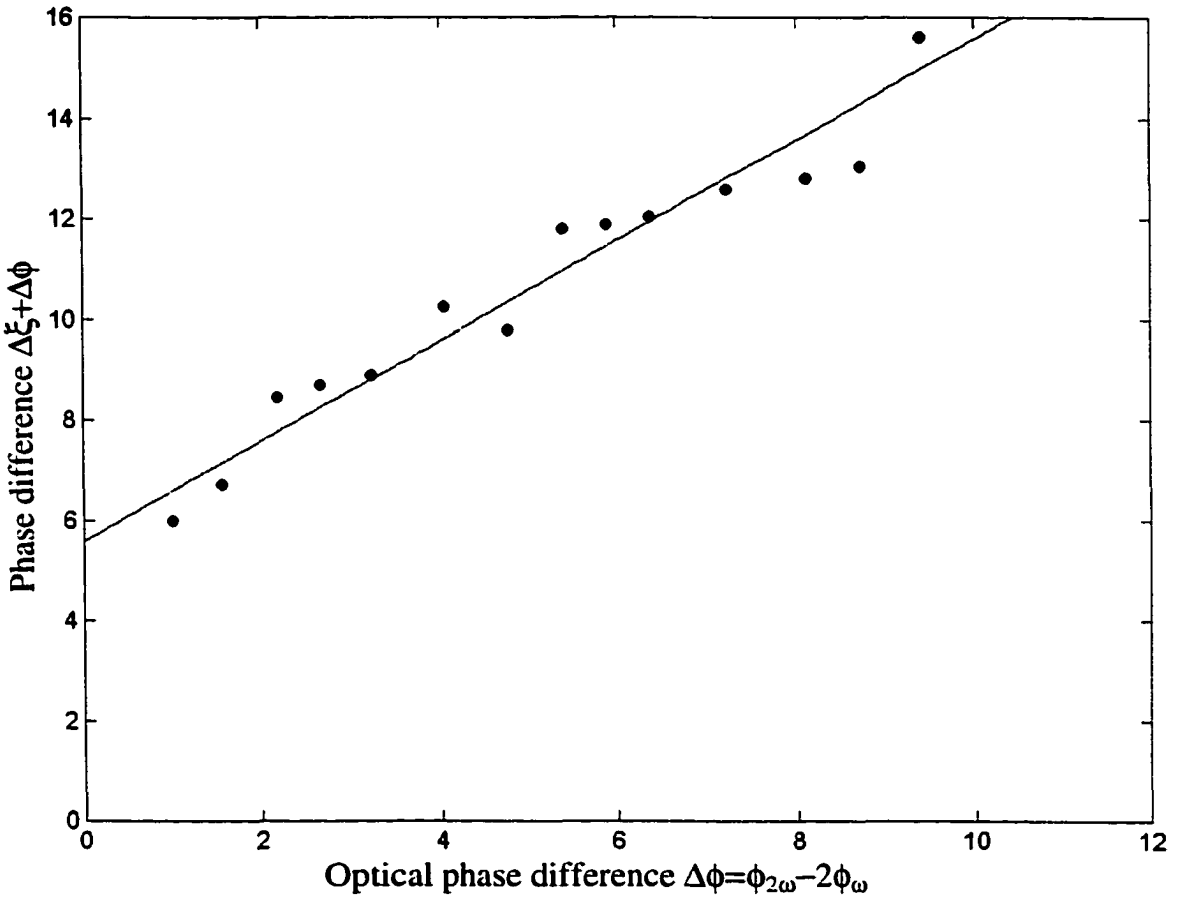

Figure 6.12: The phase difference between the partial waves, $\Delta\xi+\Delta\phi$, versus the optical phase difference $\Delta\phi$. The solid line is the best fit to the data points. The intercept yields the atomic phase difference between *p*- and *d*-waves.

$\Delta = \Delta\phi + \Delta\xi$ that produces the best fit to the experimental images versus N_2 pressure and in Fig. 6.12 we plot the phase difference Δ versus fourteen different values of the optical phase $\Delta\phi = \phi_{2\omega} - 2\phi_{\omega}$. The solid line is the best fitting line of these data with unit slope. The intercept gives our final result, the phase difference $\Delta\xi = \xi_p - \xi_d = 5.54$.

We can estimate the uncertainty of the phase difference $\Delta\xi = 5.54$ with the formula

$$\sigma_{pd}^2 = \frac{1}{N}\sum_i^N (\Delta_i - \Delta\xi - \Delta\phi_i)^2 \qquad (6.27)$$

where $\Delta\xi = \xi_p - \xi_d = 5.54$, Δ_i and $\Delta\phi_i$ are the 14 total phases and optical phases we measured, respectively, and N=14. According to these values, $\sigma_{pd} = 0.18$. Therefore our final result should be $\Delta\xi = 5.54 \pm 0.18$.

Theoretically, the phase difference is the sum of the quantum defect phase, which is determined from the bound state spectra, and the phase difference of Coulomb phase for the two continuum waves, i.e. $\xi_p - \xi_d = \delta_p - \delta_d + \eta_p - \eta_d$. The quantum defect phase is expressed as (see Appendix E)

$$\delta_p - \delta_d = (1.301 - 0.918\varepsilon - 3.05\varepsilon^2)\pi \qquad (6.28)$$

and the Coulomb phase between *p*- and *d*-waves is (see Appendix D)

$$\eta_p - \eta_d = \arctan\frac{1}{2\sqrt{\varepsilon}} \qquad (6.29)$$

where ε is the electron energy in Rydberg. At the wavelength of 560 nm (ε= 250.85 eV or 0.0184 Rydberg), this value (the phase difference $\xi_p - \xi_d$) is evaluated to be 5.33, which is in good agreement with our measured value.

6.5 Angular distributions by parallel-polarized two-color field

We also carried out the measurement with both UV and visible beams polarized horizontally. In this case, we insert a half-wave Fresnel rhomb between mirrors M_1 and M_3, with the axis 45° from vertical, to rotate the polarization direction of the visible light from vertical to horizontal. The two linearly-polarized beams then are further purified by a high quality Glan air prism polarizer, which is rotated by an angle accordingly to match the polarization of the light. Fig. 6.13 is the schematic diagram of the optical set-up. We record twelve images of the angular distributions of photoelectrons ejected from the ionization process in rubidium with parallel polarized two-color fields by varying the N_2 pressures over twelve different values from 0 Torr to 115 Torr. We have observed the asymmetry of the PAD with the change of N_2 pressure.

As in the preceding section, we first show the images recorded with only one frequency component of the laser field at a time. The five figures in the left column of Fig. 6.14 correspond to one-photon ionization with the 280 nm UV light alone; and the figures in the right column are produced from the two-photon ionization process by the 560 nm visible light alone. Both fields are horizontally polarized. Fig. 6.14 (a1) and (a2) show the recorded images produced on the phosphor screen of the MCP, and Fig. 6.14 (b1) and (b2) are theoretically calculated images based on the experimental conditions for comparison with the recorded images. Fig. 6.14 (c1) and (c2) are mesh plots of the image data, which are smoothed somewhat by averaging each pixel value with its adjacent pixels. Fig. 6.14 (d1) and (d2) are the slices of the images from the central row. The corresponding angular distributions of the photoelectrons that produce these images are shown in Fig. 6.14 (e1) and (e2).

As we have seen in the previous section, the images are symmetric in both one and two-photon processes. When both the UV and visible lights interact with the atoms, the images show an asymmetry and vary with varying the phase between

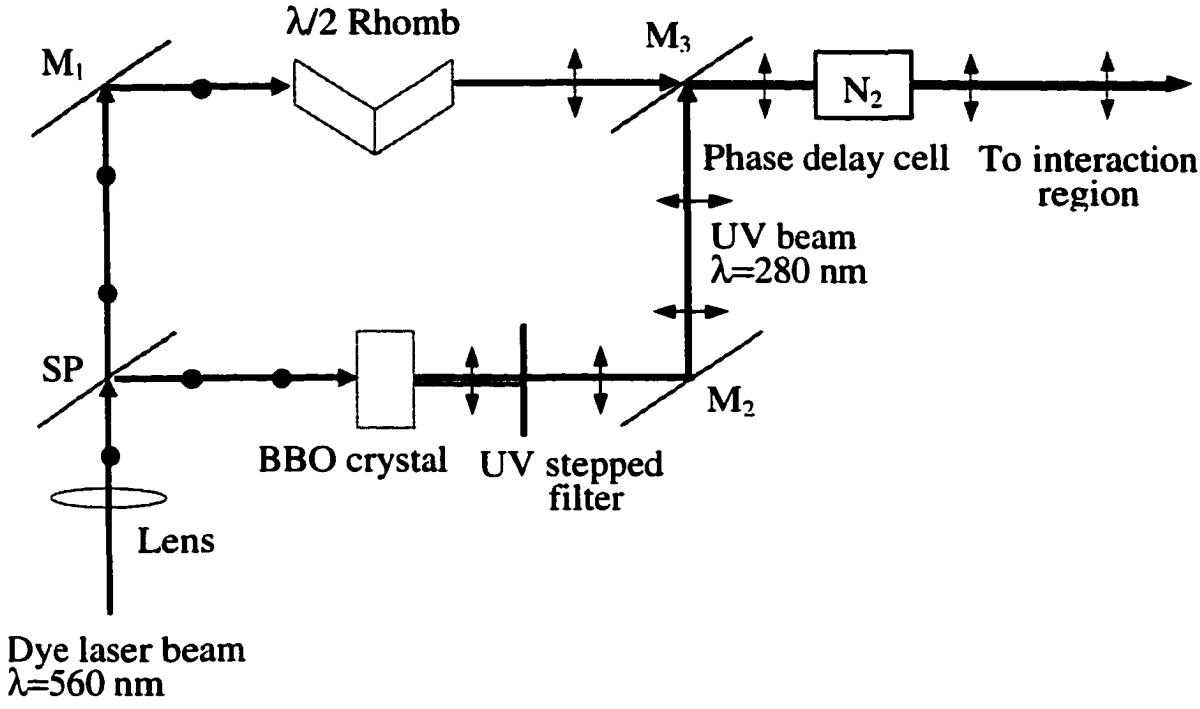

Figure 6.13: Schematic diagram of optical system for the experiment with parallel-polarized two-color field.

Figure 6.14: Images recorded (a1) with the horizontally–polarized 280 nm UV light alone and (a2) with the horizontally-polarized 560 nm visible light alone. (b1) and (b2) are the calculated images, (c1) and (c2) are mesh plots, (d1) and (d2) are the central row slice of the recorded data (dot) with the best fit curve of the calculated image (solid line), (e1) and (e2) are the corresponding angular distributions which produce these images.

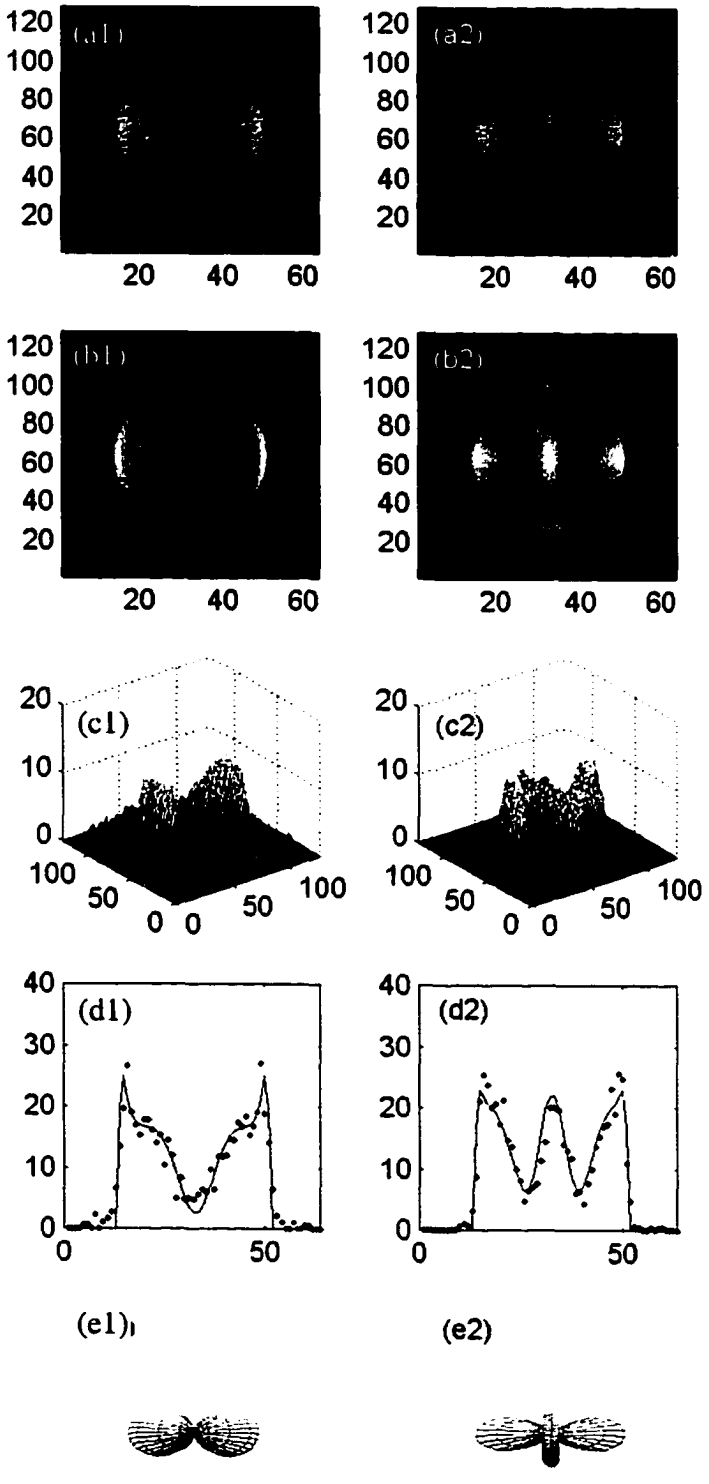

Figure 6.14

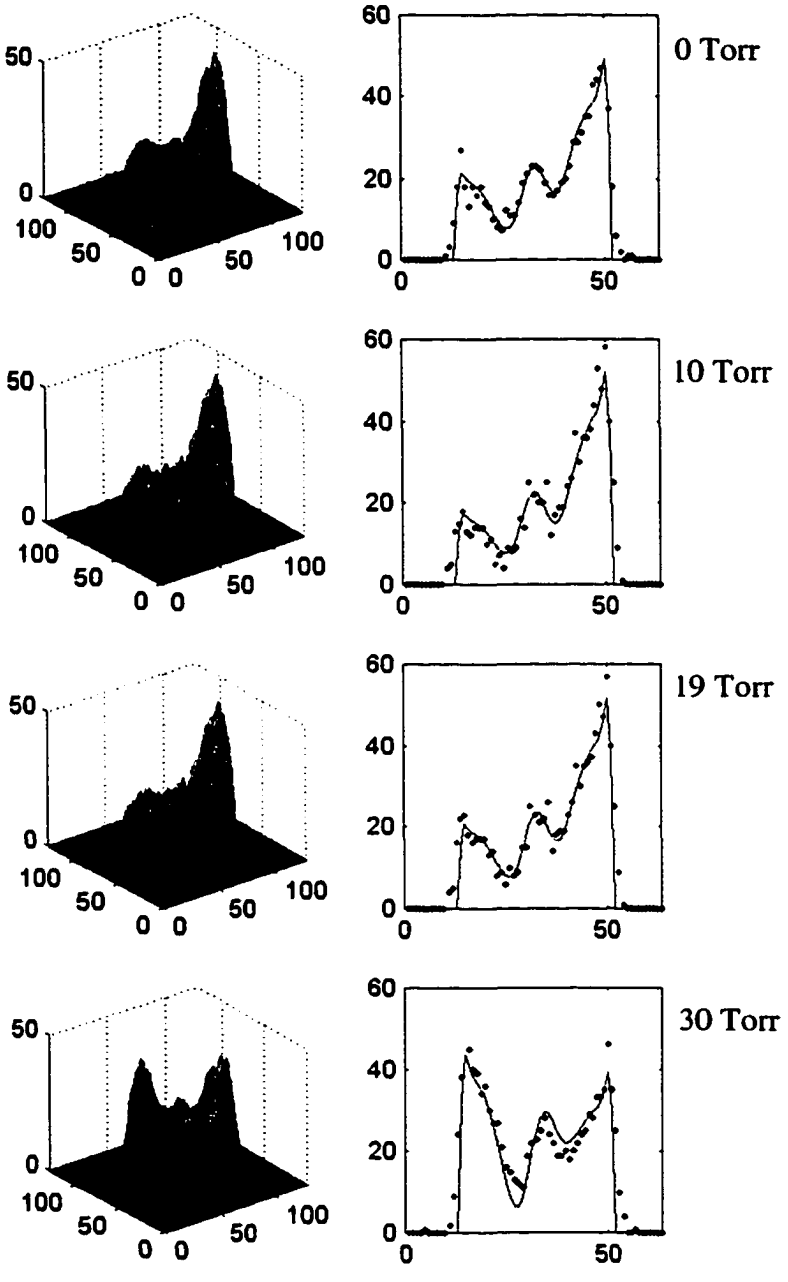

Figure 6.15: Mesh plots of the recorded images and the central row slices of the recorded data (dot) with the best fit curves of the calculated images (solid lines). Images are taken by horizontally-polarized two-color fields. The asymmetric electron angular distributions vary with varying the N_2 pressure.

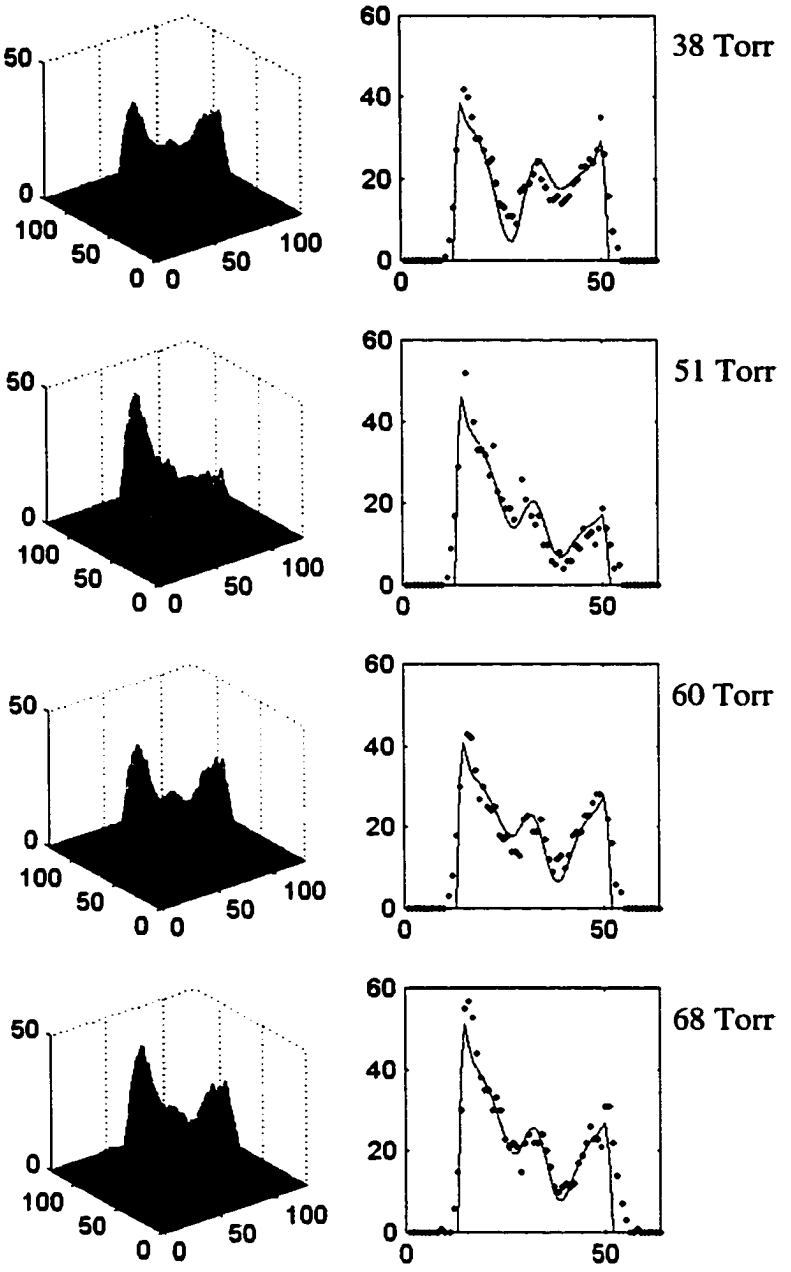

Figure 6.15 (continued)

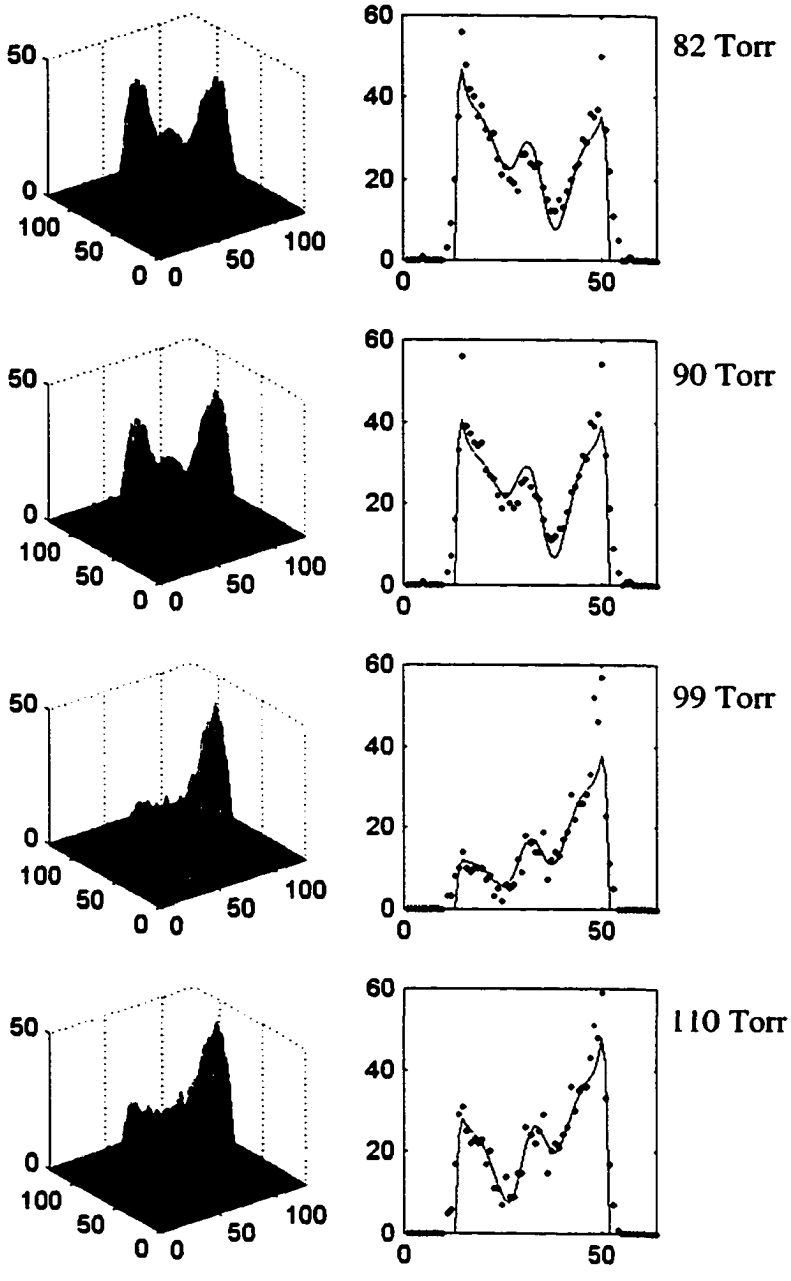

Figure 6.15 (continued)

the two fields. Fig. 6.15 shows the mesh plots and the cross sections of the twelve images. The solid line in each subplot of the right column is the best fit curve to the data points a cross the central row of each image. From these plots we see that the image asymmetry changes with changing the pressure.

In Fig. 6.16 we plot three typical images (a1) to (a3). Fig. 6.16(c1) to (c3) and (d1) to (d3) are slices from the central row (row 64) and row 81, respectively, including both the experimental data points and the theoretical best fitting curves. In each case the agreement between the experimental data (dots) and the best fit theoretical curve is very good. Data in the first and third columns were collected at the optical phase difference that resulted in near maximally asymmetric distributions. The phase difference between these two data sets is nearly π which results in opposite asymmetric distributions.

As we did in the case of the perpendicularly-polarized fields, we analyze our images using the two-photon parameters, $S_{\bar{s}}/S_{\bar{d}} = -0.42$, $S_{\Delta d}/S_{\bar{d}} = -0.36$, and $\xi_s - \xi_d = 2.08$ obtained in our previous experiment (see Chapter 5) for the laser light at the wavelength of 560 nm, and the value 1.96 for the ratio $R_{1/2}/R_{3/2}$. For each image data, we adjust the phase difference between the two partial waves $\Delta = \Delta\phi + \Delta\xi$ ($\Delta\phi = \phi_{2\omega} - 2\phi_{\omega}$ and $\Delta\xi = \xi_p - \xi_d$) for the calculated image to determine the value of Δ that yields the best fit with experimentally-obtained image. In Fig. 6.17 we plot the phase difference Δ versus N_2 pressure. The solid line is the best fitting line of these data. We also see that a 2π phase change corresponds to a pressure change of ~102 Torr in this case.

We did not measure the relative phase between the UV and the visible laser fields $\Delta\phi = \phi_{2\omega} - 2\phi_{\omega}$ for this experiment due to the experimental difficulties in the case of parallel polarization. Therefore we could not get the phase difference between *p*- and *d*-waves from this experiment.

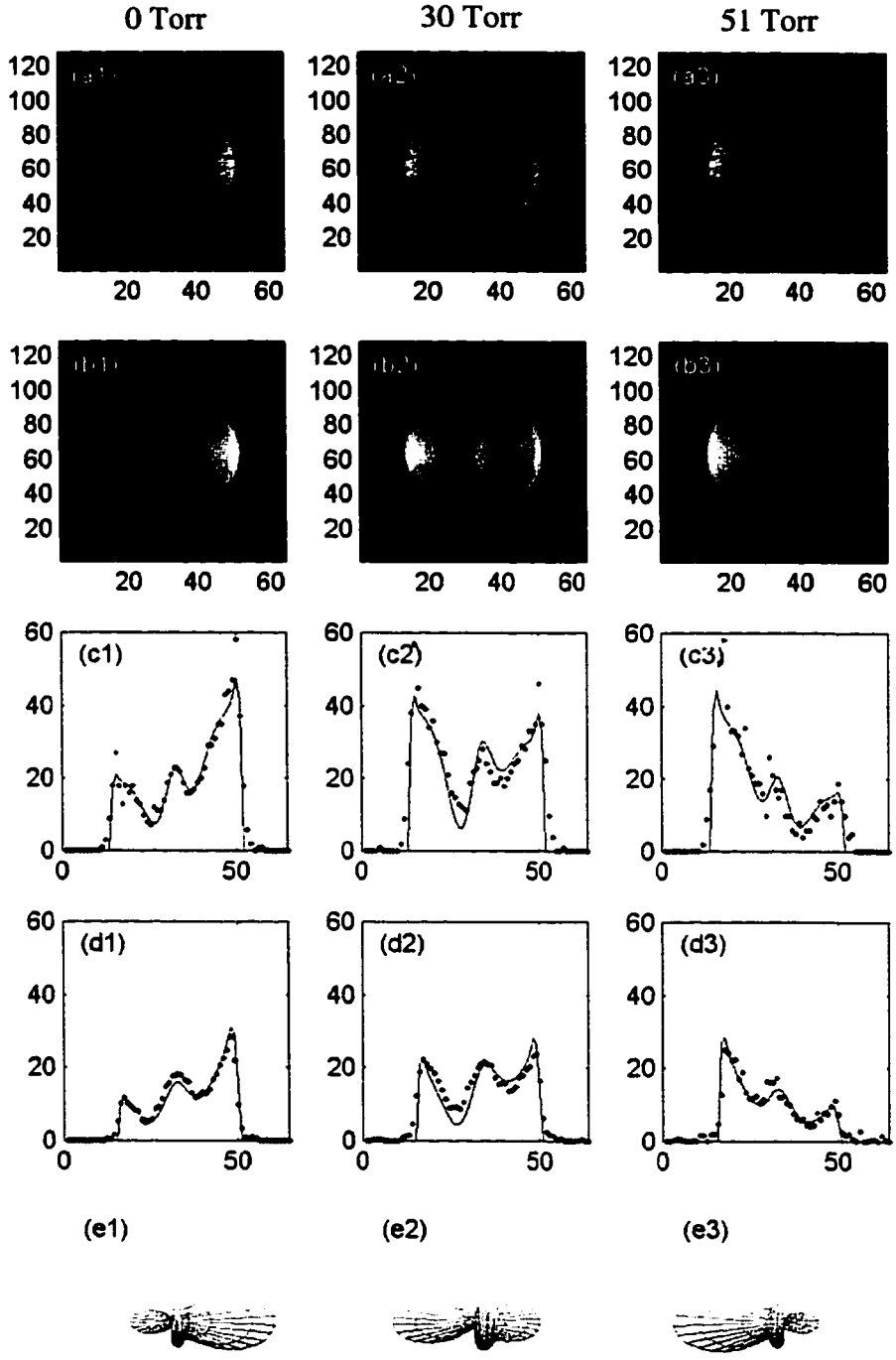

Figure 6.16: Three recorded images (a1-a3) and theoretically calculated images (b1-b3) with three different pressures showing on the top. The slices, from single rows 64 (c1-c3) and 81(d1-d3), show both the data points and the calculated image fit (solid lines). Images (a1) and (a3) were taken at an optical phase difference near π. They show the near maximum asymmetry in the opposite direction. Figs. (e1) to (e3) are the corresponding angular distributions. Images taken by horizontally-polarized two-color fields (λ_1=560 nm and λ_2=280 nm).

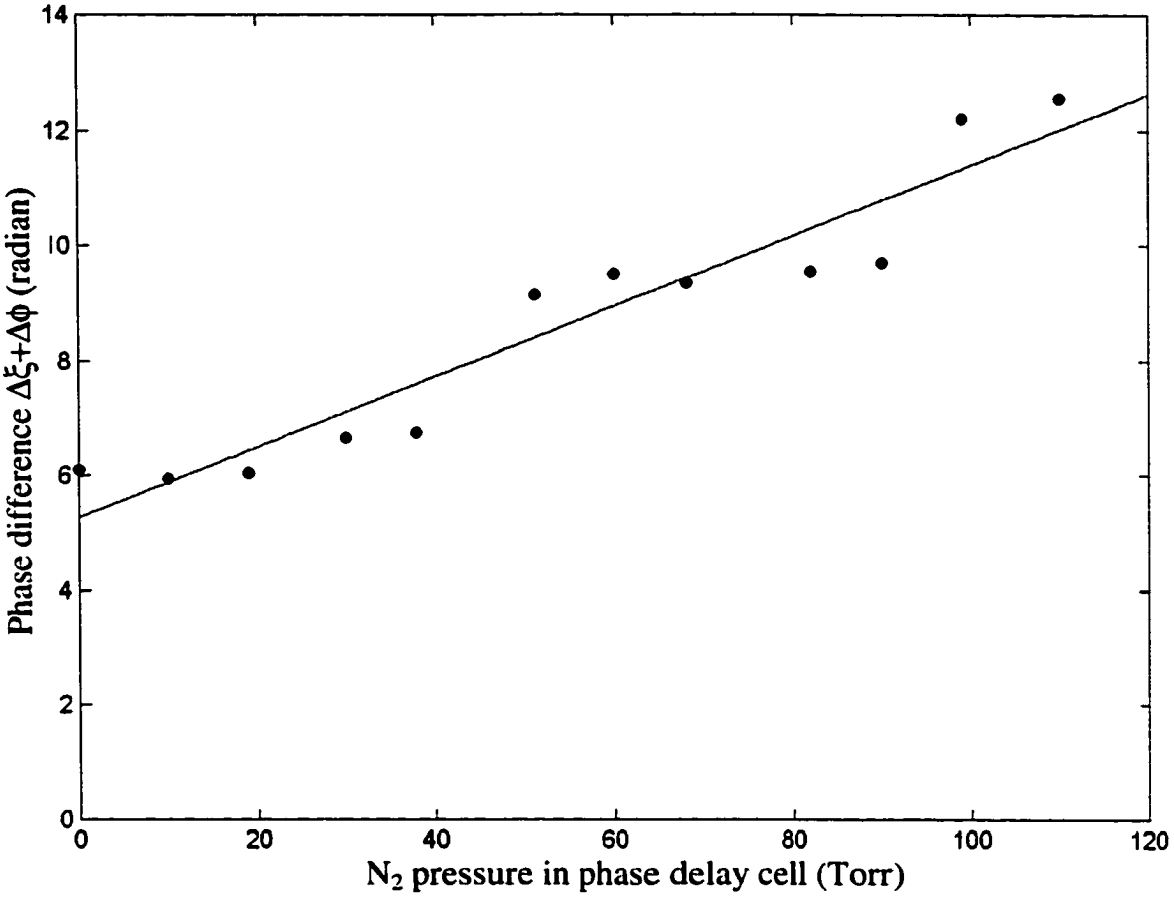

Figure 6.17: The phase difference between the partial waves, $\Delta\xi+\Delta\phi$, versus N_2 pressure in the phase delay cell. The solid line is the best fit to the data points.

6.6 Summary

In this Chapter we have described the details of the measurements of the asymmetric photoelectron angular distribution with two-color laser fields using our newly-developed photoelectron detection technique. We observed the quantum mechanical interference with both perpendicularly and parallel polarized two-color laser fields. It is worthy to point out that the quantum interference observed with perpendicularly polarized two-color fields is unique. The mesh plots clearly show the asymmetric photoelectron angular distributions and the changes with changing the relative optical phase. These plots give us a direct view of the quantum interference. These asymmetric distributions indicate that the atomic wavefunction of the continuum state formed by the two-color field can be described as the coherent superposition of the individual continuum states. Based on the analysis of the measured angular distributions with perpendicularly polarized two-color laser fields we derived the phase difference between even and odd continuum waves for the first time. We conclude that this study has successfully accomplished our goals we stated earlier in this chapter.

CHAPTER 7
CONCLUSIONS

In this thesis we have presented the details of our complete measurements of two-photon ionization in the rubidium atom. For this study we developed an effective technique to measure the angular distributions of photoelectrons using elliptically-polarized light. In these measurements, all electrons emitted from the interaction region are collected to form an image on the phosphor screen of a micro channel plate assembly. We measured the images at nine different laser wavelengths. Through careful analysis of the image data we successfully determined the three microscopic atomic parameters--the phase difference between the *s*- and *d*-partial waves, $\Delta\xi = \xi_s - \xi_d$, the relative cross section of the *S* and *D* ionization channels, σ_s/σ_d, and the relative cross section for photo-ionizing the atom into two fine structure states $\varepsilon d\,^2D_{3/2}$ and $\varepsilon d\,^2D_{5/2}$, $\sigma_{5/2}/\sigma_{3/2}$. The measured phase differences are in excellent agreement with expected values over the entire range of the laser wavelengths from 532 nm to 590 nm, (the corresponding electron energy is from 483.9 meV to 25.7 meV) showing a varying function of photo-electron energy. The measured relative cross sections for ionization into *S* and *D* channels are in good agreement with one set of theoretical data and previous experimental results obtained using conventional technique for the measurements of PAD. The relative contribution of the *s*-wave to the photo-ionization process is much less than the contribution of d-wave. Our present data show these values varying from 15% to 30% with decreasing the

photoelectron energy from 483.9 meV to 25.7 meV. The ratios of cross sections of the two *D* channels, however, show a large discrepancy with expected values. These results suggest that the fine structure effect cannot be ignored.

We also used the same technique to study quantum mechanical interference with both perpendicularly and parallel polarized two-color laser fields, which consists of the fundamental output (560 nm) of a laser and its second harmonic (280 nm). These two-color fields are used to drive both two-photon and one-photon ionization processes. When both fields are applied concurrently, the continuum wave excited by the two interactions simultaneously is a linear combination of even- and odd-wave functions since the *S* and *D* states have even parity, and the *P* state has odd parity. We were able to change the angular distribution of photoelectrons by varying the relative phase between the laser field components, which excite these partial waves. We observed the extremely asymmetric angular distribution produced by interfering even- and odd-order photo-ionization processes of Rb atom. To our knowledge, the quantum interference observed with perpendicularly-polarized two-color fields is unique. By fitting the calculated images to the measured images we obtained the corresponding total phase difference (atomic phase plus optical phase) between the continuum partial waves precisely, and hence we successfully determined the phase differences between *p*- and *d*-continuum waves. The values of the relative phase are in excellent agreement with the calculated values from quantum defect theory. The measured value matches to within 4% of the calculated value. It is worth to point out that the method we used for the measurement of the relative phase between the two perpendicularly-polarized laser fields is successful. It is impossible to determine the phase difference between even- and odd-continuum waves without measuring the optical phase in this experiment.

REFERENCES

REFERENCES

1. W. Bothe Z. Phys. **26**, 59 (1924).
2. Milton A. Chaffee, Phys. Rev. **37**, 1233 (1931).
3. C. N. Yang, Phys. Rev. **74**, 764 (1948).
4. W. Zernik, Phys. Rev. **A 135**, 51 (1964).
5. J. Cooper and R. N. Zare, J. Chem. Phys. **48**, 942 (1968).
6. J. Cooper and R. N. Zare, In "Atomic Collision Processes, Lectures in Theoretical Physics XI-C " (S. Geltman, K. T. Mahanthappa, and W. E. Brittin, eds), pp 317-337. Gordon and Breach, New York.
7. J. C. Tully, R. S. Berry, and B. J. Dalton, Phys. Rev. **176**, 95 (1968).
8. D. Dill, S. J. Manson, and A. F. Starace, Phys. Rev. Lett. **32**, 971 (1974).
9. P. Lambropoulos, Adv. At. Mol. Phys. **12**, 87 (1976).
10. P. Lambropoulos, Phys. Rev. Lett. 28, 585 (1972); P. Lambropoulos, *ibid.* **29**, 453 (1972).
11. P. Lambropoulos and M. R. Teague, J. Phys. **B 9**, 587 (1976).
12. T. Olsen, P. Lambropoulos, S. E. Wheatley and S. P. Rountree, J. Phys. B: At. Mol. Phys. **11**, 4167 (1978).
13. N. Aymar, M. Crance, J. Phys. B: At. Mol. Phys. **12**, L 667 (1979).
14. S. N. Dixit, J. Phys. B 16, 1205 (1983).

30. P. Kruit, J. Kimman, A. G. Muller, M. J. van der Wiel, Phys. Rev. **A 28**, 248 (1983).

31. K. Rzazewski, R. Grobe, Phys. Rev. **A 33**, 1855 (1986).

32. D. Feldmann, D. Petring, G. Otto, and K. H. Welge, Z. Phys. **D 6**, 35 (1987).

33. D. Feldmann, B. Wolff, M. Wemhoner, and K. H. Welge, Z. Phys. **D 6**, 293 (1987).

34. D. W. Schumacher, F. Weihe, H. G. Muller, and P. H. Bucksbaum, Phys. Rev. Lett. **73**, 1344 (1994).

35. W. Ohnesorge, F. Diedrich, G. Leuchs, D. S. Elliott, and H. Walther, Phys. Rev. **A 29**, 1181 (1984).

36. S. N. Dixit and P. Lambropoulos, Phys. Rev. Lett. **41**, 1278 (1981).

37. S. N. Dixit and P. Lambropoulos, Phys. Rev. **A 27**, 861 (1983).

38. Ce Chen, Yi-Yian Yin, and D. S. Elliott, Phys. Rev. Lett. **64**, 507 (1990).

39. Ce Chen and D. S. Elliott, Phys. Rev. Lett. **65**, 1737 (1990).

40. Seung Min Park, Shao-Ping Lu, and Robert J. Gordon, J. Chem. Phys., **94**(12), 8622 (1991).

41. Guoqiang Xing, Xuebin Wang, Xin Huang, and Richard Bersohn, J. Chem. Phys. **104** (3), 826 (1996).

42. D. W. Schumacher, F. Weihe, H. G. Muller, and P. H. Bucksbaum, Phys. Rev. Lett. **73**, 1344 (1994).

43. D. W. Schumacher and P. H. Bucksbaum, Phys. Rev. **A 54**, 4271 (1996).

44. Kenneth J. Schafer and Kenneth C. Kulander, Phys. Rev. **A 45**, 8026 (1992).

45. A. Szoke, K. C. Kulander, and J. N. Bardsley, J. Phys. **B 24**, 3165 (1991).

46. R. M. Potvliege and Philip H. G. Smith, J. Phys. **B 25**, 2501 (1992).

47. Moshe Shapiro, John Hepburn, and Paul Brumer, Chem. Phys. Lett. **149**, 451 (1988).

48. C. Charron, A. Giusti-Suzor, and F. H. Mies, Phys. Rev. Lett. **71**, 692 (1993).

49. Y.-Y. Yin, C. Chen and D. S. Elliott, Phys Rev. Lett. **69**, 2353 (1992).

50. Y.-Y. Yin and D. S. Elliott, Phys. Rev. **A 47**, 2881 (1993).

51. Michael G. Littman, Applied Optics, **23**, 4465 (1984).

52. H. Helm, N. Bjerre, M.J. Dyer, D. L. Huestis, and M. Saeed, Phys Rev. Lett. **70**, 3221 (1993).

53. Z.-M. Wang and D.S. Elliott, Phys. Rev. Lett. **84**,3795(2000); Phys. Rev. A, **62**, 053404 (2000).

54. B. P. Stoicheff and E. Weinberger, Can. J. Phys. **57**, 2143 (1979).

55. S. A. Lee, J. Helmcke, J. L. Hall, and B. P. Stoicheff, Opt. Lett. **3**, 141 (1978).

56. C. J. Sansonetti and K. –H. Weber, J. Opt. Soc. Am. **B 2**, 1385 (1985).

57. H. A. Bethe and E. E. Salpeter, *Quantum Mechanics of One- and Two- Electron Atoms* (Plenum, New York, 1977).

58. Joachim Kessler, *Polarized Electrons* (New York,1985).

59. K.L. Reid, D.J. Leahy, and R.N. Zare, Phys. Rev. Lett. **68**, 3527 (1992).

60. C.S. Feigerle, R.N. Comptom, L.E. Cuéllar, N.A. Cherepkov, and L.V. Chernysheva, Phys. Rev. A **53**, 4183 (1996).

61. M. Born and E. Wolf, *Principles of Optics*, 6th ed. (Permagon Press, Oxford, 1980).

62. X. Tang and P. Lambropoulos, as reported by A. Dodhy, R.N. Compton, and J.A.D. Stockdale, Phys. Rev. Lett. **54**, 422 (1985).

63. M.S. Pindzola, as reported by A. Dodhy, R.N. Compton, and J.A.D. Stockdale, Phys. Rev. Lett. **54**, 422 (1985).

64. S.J. Smith and G. Leuchs, *Advances in Atomic and Molecular Physics*, **24**, 157(1987).

65. Brumer and M. Shapiro, Chem. Phys. Lett. **126**, 541(1986);
J. Chem. Phys., **84**, 4013(1986);
Accounts Chem. Res. **22**, 407(1989).

66. L. Zhu, V. Kleiman, X. Li, S.P. Lu, K. Trentelman, R.J. Gordon, Science, **270**, 77(1995); L. Zhu, K. Suto, J.A. Fiss, R. Wada, T. Sceideman and R.J. Gordon, Phys. Rev. Lett. **79**, 4108(1997).

67. A. Shnitman, I. Sofer, I. Golub, A. Yogev, M. Shapiro, Z. Chen, and P. Brumer, Phys. Rev. Lett. **76**, 2886(1996).

68. Z. Chen, M. Shapiro, and P. Brumer, J. Chem. Phys. **98**, 8647 (1993); **98**, 6843 (1993).

69. S.T. Pratt, J. Chem. Phys. **104**, 5778 (1996).

70. F. Wang, C. Chen, and D.S. Elliott, Phys. Rev. Lett. **77**, 2416 (1996); F. Wang, D.S. Elliott, Phys. Rev. A, **56**, 3065 (1997).

71. Y.-Y. Yin, D.S. Elliott, R. Shehadeh, E.R. Grant, Chem. Phys. Lett. **241**, 591 (1995).

72. Z.-M. Wang and D.S. Elliott, Phys. Rev. Lett. **87**, 173001 (2001).

73. G. Wentzel, Z. Phys. **41**, 828 (1927).

74. R.M. Potvliege and P.H.G. Smith, J. Phys. B **24**, L641 (1991).

75. Y.-Y. Yin and D.S. Elliott, Phys. Rev. A, **45**, 281 (1992).

76. C.J. Lorenzen and K. Niemax, Phisica Scripta, **27**, 300 (1983).

77. Takashi Nakajima, Phys. Rev. A, **61**, 041403(R) (2000).

78. J. Colgan and M.S. Pindzola, Phys. Rev. Lett. **86**, 1998 (2001).

79. F. Arqueros, P.E. LaRocque, M.S. O'Sullivan, and B.P. Stoicheff, Opt. Lett. **9**, 82 (1984).

80. A. Burgess and M.J. Seaton, Mon. Not. R.Astron. Soc. **120**, 121 (1960); G. Peach, Mem. R. Astron. Soc. **71**, 13 (1967).

APPENDICES

Appendix A

Example of measurement of photoelectron angular distribution using conventional technique and determination of atomic parameters

The purpose of this appendix is to present the principle for obtaining the atomic parameters through the measurement of the angular distributions of photoelectrons using the conventional technique described in Sec. 2.4.

We consider two-photon ionization of alkali metals from the initial *s*-state using linearly polarized laser light. In this case the general angular distribution equation for multiphoton ionization (Eq. (2.6) in Chapter 2)

$$\frac{d\sigma^{(N)}}{d\Omega} = \frac{\sigma_T^{(N)}}{4\pi} \sum_{j=0}^{N} \beta_{2j} P_{2j}(\cos\Theta),$$

can be expressed as a power series in cosΘ

$$\frac{d\sigma}{d\Omega} = \alpha_o (1 + \alpha_2 \cos^2\Theta + \alpha_4 \cos^4\Theta) \qquad \text{(A1a)}$$

or in a harmonic series

$$\frac{d\sigma}{d\Omega} = a_o (1 + a_2 \cos 2\Theta + a_4 \cos 4\Theta). \qquad \text{(A1b)}$$

In these equations Θ is defined as the angle between the directions of the laser field polarization and the velocity of electrons. The coefficients α_2 and α_4 or a_2 and a_4 can be obtained by fitting data to equation (A1) (see Fig. 2.3). These coefficients are functions of three parameters: the phase difference between the *s*- and *d*-partial waves, $\Delta\xi = \xi_s - \xi_d$, the relative cross section of the *s*- and *d*-partial waves, σ_s/σ_d, and the relative cross section of two fine structure states of the *d*-wave, $\sigma_{5/2}/\sigma_{3/2}$.

We now address the question of how to relate the coefficients a_2 and a_4 in Eq. (A1b) to the atomic parameters using linearly-polarized light. Yin and Elliott [50] carried out the measurements of the photoelectron angular distribution and derived the atomic parameters using this method. From the following brief review of their work, we can understand the conventional technique.

According to Lambropoulos and Teague [11] the angular distribution can be written as

$$\frac{d\sigma}{d\Omega} = \frac{1}{2}\left\{\left|T^q_{++}\right|^2 + \left|T^q_{--}\right|^2 + \left|T^q_{+-}\right|^2 + \left|T^q_{-+}\right|^2\right\}, \tag{A2}$$

where q=0, +1, -1 (corresponding to Δm_j= 0, +1, -1) is the light polarization index which represents linearly, right circularly and left circularly-polarized light, respectively. For linearly-polarized light, the transition amplitudes T_{fi}^q are expressed as the following forms:

$$\begin{aligned}
T^0_{++} &= T^0_{--} = Y_{00}(\Theta,\Phi)e^{i\xi_s}\left(\frac{1}{9}\right)(S_1 + 2S_2) \\
&\quad + Y_{20}(\Theta,\Phi)e^{i\xi_d}\left(\frac{-2}{45\sqrt{5}}\right)(5S_3 + S_4 + 9S_5), \\
T^0_{-+} &= Y_{21}(\Theta,\Phi)e^{i\xi_d}\left(\frac{2}{15\sqrt{30}}\right)(5S_3 + S_4 - 6S_5), \\
T^0_{+-} &= T^0_{-+} \qquad \text{if } Y_{21} \text{ is replaced by } Y_{2-1}
\end{aligned} \tag{A3}$$

where S_1-S_5 are two-photon radial matrix elements, f, i = + or - represent the sign of the electron spin in the final and initial state. We can clearly verify these results qualitatively from the ionization channels of rubidium in Fig. 2.3 and Fig. 2.4 in Sec. 2.3. Let's look at Eq. (A3) and Fig. 2.3. We see that the factor (S_1+2S_2) is associated with the partial *s*-wave, (5S_3+S_4+9S_5) is associated with the partial *d*-

wave, and the factor ($5S_3$+S_4-$6S_5$) comes from the fine structure of the continuum *d*- state.

If we use $S_{\bar{s}}/S_{\bar{d}}$ and $S_{\Delta d}/S_{\bar{d}}$ to express the following forms

$$\frac{S_{\bar{s}}}{S_{\bar{d}}}=\frac{S_1+2S_2}{5S_3+S_4+9S_5} \quad \text{and} \quad \frac{S_{\Delta d}}{S_{\bar{d}}}=\frac{1}{3}\left(\frac{5S_3+S_4-6S_5}{5S_3+S_4+9S_5}\right), \tag{A4}$$

then $S_{\bar{s}}/S_{\bar{d}}$ indicates the relative contribution of the *s*-wave to the photo-ionization process, while $S_{\Delta d}/S_{\bar{d}}$ reflects the influence of fine structure effect on the relative strengths of the j=3/2 and j=5/2 components of the *d*-wave.

For linearly-polarized light, the cross sections for ionization into any of these three channels can be found by integrating Eq. (A2) over angle (Θ,Φ) with consideration of Eq. (A3), resulting in

$$\begin{aligned}
\sigma_s &= \frac{1}{9}\left[\frac{S_1+2S_2}{3}\right]^2 && \text{for } 5s\ {}^2S_{1/2} \rightarrow \varepsilon\,{}^2S_{1/2} \\
\sigma_{3/2} &= \frac{8}{225}\left[\frac{5S_3+S_4}{6}\right]^2 && \text{for } 5s\ {}^2S_{1/2} \rightarrow \varepsilon\,{}^2D_{2/3} \\
\sigma_{5/2} &= \frac{12}{225}S_5^2 && \text{for } 5s\ {}^2S_{1/2} \rightarrow \varepsilon\,{}^2D_{2/5} \\
\sigma_d &= \sigma_{3/2}+\sigma_{5/2}
\end{aligned} \tag{A5}$$

Introducing Eqs. (A2) into (A3) and collecting terms in cos2Θ and cos4Θ, one can show that

$$a_2=\frac{12[1-2(S_{\bar{s}}/S_{\bar{d}})\cos\Delta\xi]}{11+8(S_{\bar{s}}/S_{\bar{d}})^2-8(S_{\bar{s}}/S_{\bar{d}})\cos\Delta\xi+9(S_{\Delta\bar{d}}/S_{\bar{d}})^2} \tag{A6a}$$

and

$$a_4=\frac{9[1-(S_{\Delta\bar{d}}/S_{\bar{d}})^2]}{11+8(S_{\bar{s}}/S_{\bar{d}})^2-8(S_{\bar{s}}/S_{\bar{d}})\cos\Delta\xi+9(S_{\Delta\bar{d}}/S_{\bar{d}})^2} \tag{A6b}$$

where $\Delta\xi = \xi_s - \xi_d$ is the phase difference between the continuum s- and d-waves.

Comparing Eq. (A4) with Eq. (A5), the parameters $\frac{S_{\bar{s}}}{S_{\bar{d}}}$ and $\frac{S_{\perp d}}{S_{\bar{d}}}$ can be further expressed as functions of the cross sections

$$\frac{S_{\bar{s}}}{S_{\bar{d}}} = \frac{1}{5}\left[\frac{4\sigma_s}{5\sigma_d}\left[1+\frac{1}{6}\left(\frac{S_{\perp d}}{S_{\bar{d}}}\right)^2\right]\right]^2 \tag{A7a}$$

and

$$\frac{S_{\perp d}}{S_{\bar{d}}} = \frac{1-[2\sigma_{5/2}/3\sigma_{3/2}]^{1/2}}{1+[3\sigma_{5/2}/2\sigma_{3/2}]^{1/2}}. \tag{A7b}$$

The coefficients a_2 and a_4, which determine the angular distribution, can be obtained by fitting Eq. (A1b) to the experimental data (see Fig. 2.6). We see that Eqs. (A6a) and (A6b) contain three atomic parameters. Since the measured angular distribution can be completely defined by two fitting parameters. Therefore, in order to determine the three parameters from a_2 and a_4, additional measurements or theoretical results are required. Yin and Elliott determined the atomic parameters based on two assumptions:

1) They made the assumption that spin-orbital coupling has a negligible effect on the $\sigma_{5/2}/\sigma_{3/2}$ ratio. This assumption was justified on the basis of the two-photon bound-state intensity ratios. For example, Kato and Stoicheff [A1] reported measurements of fine-structure intervals in the $n\ ^2D$ series in rubidium for n = 4 −16. Stoicheff and Weinberger [A2] reported measurements of the $n\ ^2S$ and $n\ ^2D$ series energy values for n ranging to over 100. Based on these results they estimated the intensity ratio $\sigma_{5/2}/\sigma_{3/2} \approx$

1.5, and hence $S_{\Delta d} / S_{\bar{d}} = 0$ from Eq. (A7b). In this case, they could use the angular distribution data a_2 and a_4 and Eqs. (A6a), (A6b) and (A7a) to determine $\cos\Delta\xi$ and σ_s/σ_d. These results are shown in columns 3 and 4 in Table A.

2) The continuum phases of the *S* and *D* channels are given accurately by the semiemperical quantum defect theory. Once $\cos\Delta\xi$ is given by the calculation, the other two parameters σ_s/σ_d and $\sigma_{5/2}/\sigma_{3/2}$ can be determined from Eqs. (A6) and (A7) with experimentally determined angular distribution data a_2 and a_4. The data Yin and Elliott obtained by this method are listed in columns 5-6 in Table A.

Table A.1: Atomic parameters determined from experimental data [Y.-Y. Yin and D.S. Elliott, PRA, 47, 2881 (1993)].
$\cos\phi$ (i.e. $\cos\Delta\xi$ in this text) and σ_s/σ_d in columns 3 and 4 were obtained by assumption 1). σ_s/σ_d and $\sigma_{5/2}/\sigma_{3/2}$ in columns 5-6 were derived using calculated values of the continuum-wave-function phases. The two possible values for the d-wave fine structure ratio both are listed in column 6.

λ (nm)	ε (eV)	$\cos\phi$	σ_s/σ_d	σ_s/σ_d	$\sigma_{s5/2}/\sigma_{3/2}$	
591.0	0.0196	0.45(3)	1.15(12)	0.39(3)	23(7)	0.19(3)
588.2	0.0396	0.28(3)	0.86(10)	0.18(2)	25(7)	0.18(3)
585.2	0.0612	0.42(5)	0.44(7)	0.20(2)	7(2)	0.41(8)
580.3	0.0970	0.40(5)	0.38(5)	0.19(1)	6(1)	0.46(9)
571.0	0.167	0.34(9)	0.29(9)	0.15(3)	5(2)	0.5(2)
560.0	0.251	0.36(6)	0.26(5)	0.19(2)	3(1)	0.7(2)
550.5	0.328	0.27(7)	0.25(6)	0.15(4)	4(2)	0.6(2)
532.0	0.485	0.25(10)	0.14(6)	0.14(5)	2(5)	1(3)

A1. Y. Kato and B.P. Stoichff, J. Opt. Soc. Am. 66, 490 (1976).

A2. B. P. Stoicheff and E. Weinberger, Can. J. Phys. **57**, 2143 (1979).

Appendix B

Derivation of the expression for the intensity of elliptically-polarized light passing through a polarizer $P_t=P_0(|\epsilon_1|^2\sin^2\vartheta'+|\epsilon_3|^2\cos^2\vartheta')$

In this appendix we derive an expression for the intensity of elliptically-polarized light passing through a polarizer. We can write a matrix that represents an optical element on how that element transfers field components from the input to the output. For example, a vertical polarizer transfers the vertical field component unchanged, but block the horizontal component, i.e.

$$E_x' = 0$$
$$E_z' = E_z.$$

In general case, these relations can be expressed as

$$E_x' = p_x E_x \qquad 0 \le p_{x,z} \le 1$$
$$E_z' = p_z E_z$$

where E_x' and E_z' are the components of emerging beam and E_x, E_z are the components of incident beam, which can be written as

$$\begin{pmatrix} E_x' \\ E_z' \end{pmatrix} = \begin{pmatrix} p_x & 0 \\ 0 & p_z \end{pmatrix} \begin{pmatrix} E_x \\ E_z \end{pmatrix}.$$

So the Jones matrix for a vertical polarizer will be

$$J_{pv} = \begin{pmatrix} 0 & 0 \\ 0 & 1 \end{pmatrix}.$$

Applying the rotation matrix

$$J(\theta) = \begin{pmatrix} \cos\theta & \sin\theta \\ -\sin\theta & \cos\theta \end{pmatrix}$$

to the Jones matrix for the vertical polarizer, we set the following matrix for a polarizer rotated at an angle θ from vertical,
we get

$$J_{p\_rot} = \begin{pmatrix} \cos\theta & -\sin\theta \\ \sin\theta & \cos\theta \end{pmatrix} \begin{pmatrix} 0 & 0 \\ 0 & 1 \end{pmatrix} \begin{pmatrix} \cos\theta & \sin\theta \\ -\sin\theta & \cos\theta \end{pmatrix}$$
$$= \begin{pmatrix} \cos\theta & -\sin\theta \\ \sin\theta & \cos\theta \end{pmatrix} \begin{pmatrix} 0 & 0 \\ -\sin\theta & \cos\theta \end{pmatrix}$$
$$= \begin{pmatrix} \sin^2\theta & -\sin\theta\cos\theta \\ -\sin\theta\cos\theta & \cos^2\theta \end{pmatrix}.$$

For elliptically-polarized light with axes in x and z directions, the Jones vector is

$$J_{ellip} = \begin{pmatrix} E_1 \\ iE_3 \end{pmatrix}$$

After transmitting through the polarizer rotated an angle θ from vertical, the polarization of the light can be expressed as

$$J_{tras} = J_{p\_rot} \cdot J_{ellip} = \begin{pmatrix} \sin^2\theta & -\sin\theta\cos\theta \\ -\sin\theta\cos\theta & \cos^2\theta \end{pmatrix} \begin{pmatrix} E_1 \\ iE_3 \end{pmatrix}$$

$$= \begin{pmatrix} E_1\sin^2\theta - iE_3\sin\theta\cos\theta \\ -E_1\sin\theta\cos\theta + iE_3\cos^2\theta \end{pmatrix}.$$

Therefore the power of the optical field of the elliptically-polarized light through the polarizer is given by

$$P = J_{trans}^{+} \cdot J_{trans}$$
$$= E_1^2\sin^2\theta + E_3^2\cos^2\theta$$

where the J_{trans}^{+} is the complex conjugate transpose matrix, which is a row matrix. Replacing the notations we have been using in this thesis, i.e. $E_1=|\epsilon_1|$, $E_2=|\epsilon_3|$, $\theta=\vartheta'$ and $P = \frac{P_t}{P_0}$ we can write the transmission power in the form

$$P_t=P_0(|\epsilon_1|^2\sin^2\vartheta'+|\epsilon_3|^2\cos^2\vartheta')$$

which is Eq. (3.1).

Appendix C

Determination of the polarization parameters $|\epsilon_1|$ and $|\epsilon_3|$ of ellipticity for elliptically-polarized light

To find the ellipticity of elliptically-polarized light, we fit the measured data of power transmitted through a polarizer at different angles to the polarization equation we have described in Sec. 5.2.2.

$$P_t=P_0(|\epsilon_1|^2\sin^2\vartheta'+|\epsilon_3|^2\cos^2\vartheta') \qquad (C1)$$

where P_0 is the power of the incident linear light, ϑ' is the polarizer orientation from z axis. ϵ_1 and ϵ_3 are two components of the unit polarization vector $\hat{\epsilon}=\epsilon_1\hat{x}+\epsilon_3\hat{z}$. Now we solve the polarization parameters $|\epsilon_1|$ and $|\epsilon_3|$ based on the best fit of the equation (C1) to measured data.

For convenience, we use $a=|\epsilon_1|$, $b=|\epsilon_3|$, $y=\frac{P_t}{P_0}$

Then Eq. (C1) becomes

$$y=a^2\cos^2x+b^2\sin^2x \qquad (C2)$$

We denote the measured data of the power transmitted through the polarizer as y_1^*, y_2^*, ... y_n^*, which correspond to the angles of the polarizer x_1, x_2, ...x_n. Letting the calculated y values in Eq. (C2) be y_1, y_2, ... y_n, we have the sum of the square of the difference between y_i and y_i^* (i=1,2,...n)

$$\begin{aligned} S &= (y_1-y_1^*)^2+(y_2-y_2^*)^2 \ldots +(y_n-y_n^*)^2 \\ &= (a^2\cos^2x_1+b^2\sin^2x_1-y_1^*)^2+(a^2\cos^2x_2+b^2\sin^2x_2-y_2^*)^2+\ldots \\ &= \sum_{i=1}^{n}(a^2\cos^2x_i+b^2\sin^2x_i-y_i^*)^2 . \end{aligned}$$

To minimize $S(a, b)$, set $\frac{\partial S}{\partial b}=0$, i.e.

$$\frac{\partial S}{\partial b} = \sum_{i=1}^{n} 4b \sin^2 x_i (a^2 \cos^2 x_i + b^2 \sin^2 x_i - y_i^*) = 0,$$

or if we eliminate the trivial value b = 0

$$\sum_{i=1}^{n} \sin^2 x_i (a^2 \cos^2 x_i + b^2 \sin^2 x_i - y_i^*) = 0. \tag{C3}$$

Similarly, setting $\frac{\partial S}{\partial a} = 0$, we get

$$\sum_{i=1}^{n} \cos^2 x_i (a^2 \cos^2 x_i + b^2 \sin^2 x_i - y_i^*) = 0. \tag{C4}$$

Eq. (C3) can be written as :

$$a^2 \sum_{i=1}^{n} \sin^2 x_i \cos^2 x_i + b^2 \sum_{i=1}^{n} \sin^4 x_i - \sum_{i=1}^{n} y_i^* \sin^2 x_i = 0, \tag{C5}$$

or equivalently

$$\begin{aligned} & a^2 \sum_{i=1}^{n} (1 - \cos^2 x_i) \cos^2 x_i + b^2 \sum_{i=1}^{n} \sin^4 x_i - \sum_{i=1}^{n} y_i^* \sin^2 x_i \\ &= a^2 \sum_{i=1}^{n} \cos^2 x_i - a^2 \sum_{i=1}^{n} \cos^4 x_i + b^2 \sum_{i=1}^{n} \sin^4 x_i - \sum_{i=1}^{n} y_i^* \sin^2 x_i \qquad \text{(C6)} \\ &= 0. \end{aligned}$$

Similarly, Eq. (C4) can be written as:

$$a^2 \sum_{i=1}^{n} \cos^4 x_i + b^2 \sum_{i=1}^{n} \sin^2 x_i \cos^2 x_i - \sum_{i=1}^{n} y_i^* \cos^2 x_i = 0 \tag{C7}$$

Add Eqs. (C6) and (C7), yielding

$$a^2\sum_{i=1}^{n}\cos^2 x_i + b^2\sum_{i=1}^{n}\sin^4 x_i + b^2\sum_{i=1}^{n}\cos^2 x_i \sin^2 x_i - \sum_{i=1}^{n} y_i^*(\cos^2 x_i + \sin^2 x_i) = 0$$

or

$$a^2\sum_{i=1}^{n}\cos^2 x_i + b^2\sum_{i=1}^{n}\sin^2 x_i - \sum_{i=1}^{n} y_i^* = 0$$

Then we obtain

$$b^2 = \frac{\sum_{i=1}^{n} y_i^* - a^2\sum_{i=1}^{n}\cos^2 x_i}{\sum_{i=1}^{n}\sin^2 x_i} \tag{C8}$$

Combine (C5) and (C8), yielding

$$a^2\sum_{i=1}^{n}\sin^2 x_i \cos^2 x_i + \left(\frac{\sum_{i=1}^{n} y_i^* - a^2\sum_{i=1}^{n}\cos^2 x_i}{\sum_{i=1}^{n}\sin^2 x_i}\right)\sum_{i=1}^{n}\sin^4 x_i - \sum_{i=1}^{n} y_i^* \sin^2 x_i = 0 \tag{C9}$$

Solving this equation, finally, we get

$$a^2 = \frac{\sum_{i=1}^{n} y_i^* \sin^2 x_i \sum_{i=1}^{n}\sin^2 x_i - \sum_{i=1}^{n} y_i^* \sum_{i=1}^{n}\sin^4 x_i}{n\sum_{i=1}^{n}\cos^2 x_i \sin^2 x_i - \sum_{i=1}^{n}\cos^2 x_i \sum_{i=1}^{n}\sin^2 x_i} \tag{C10}$$

a^2 can be obtained by another way.

Combine Eqs. (C7) and (C8), yielding

$$a^2\sum_{i=1}^{n}\cos^4 x_i+\left(\frac{\sum_{i=1}^{n}y_i^*-a^2\sum_{i=1}^{n}\cos^2 x_i}{\sum_{i=1}^{n}\sin^2 x_i}\right)\sum_{i=1}^{n}\sin^2 x_i\cos^2 x_i-\sum_{i=1}^{n}y_i^*\sin^2 x_i=0$$

or equivalently

$$a^2\sum_{i=1}^{n}\cos^4 x_i\sum_{i=1}^{n}\cos^2 x_i+\sum_{i=1}^{n}y_i^*\sum_{i=1}^{n}\sin^2 x_i\cos^2 x_i$$
$$-a^2\sum_{i=1}^{n}\cos^2 x_i\sum_{i=1}^{n}\sin^2 x_i\cos^2 x_i-\sum_{i=1}^{n}y_i^*\cos^2 x_i\sum_{i=1}^{n}\sin^2 x_i=0$$

We then get a^2 with different form

$$a^2=\frac{\sum_{i=1}^{n}y_i^*\sin^2 x_i\sum_{i=1}^{n}\sin^2 x_i-\sum_{i=1}^{n}y_i^*\sum_{i=1}^{n}\sin^2 x_i\cos^2 x_i}{\sum_{i=1}^{n}\cos^4 x_i\sum_{i=1}^{n}\sin^2 x_i-\sum_{i=1}^{n}\cos^2 x_i\sum_{i=1}^{n}\sin^2 x_i\cos^2 x_i} \qquad \text{(C11)}$$

Eqs. (C10) and (C11) are identical. Based on Eqs. (C8) and (C10) or (C11), we can use the two sets of measured data, the angles of polarizer (x_i) and the corresponding transmitted power (y_i^*), to calculate the polarization parameters $|\epsilon_1|$ and $|\epsilon_3|$ (i.e. a and b in the above derivation).

Appendix D

Derivation of Coulomb phase differences between *s*-, *p*- and *d*- partial waves

The Coulomb phase of l' the partial wave is expressed as [80]

$$\eta_{l'} = \arg[\Gamma(l' + (1 - \frac{i}{\sqrt{\varepsilon}}))], \tag{D1}$$

where Γ is the complex gamma function, ε is the electron energy in Rydbergs. From the recurrence relation of gamma function

$$\Gamma(z+2)=(z+1)\Gamma(z+1),$$

we have

$$\arg\Gamma(z+2)=\arg(z+1)+\arg(z+1),$$

or

$$\arg\Gamma(z+2)-\arg\Gamma(z+1)=\arg(z+1). \tag{D2}$$

According to Eq. (D1), the Coulomb phases for *s*-, *p*- and *d*-waves are expressed as

$$\eta_s = \arg[\Gamma(1 - \frac{i}{\sqrt{\varepsilon}})], \tag{D3a}$$

$$\eta_p = \arg[\Gamma(1 + (1 - \frac{i}{\sqrt{\varepsilon}}))], \tag{D3b}$$

$$\eta_d = \arg[\Gamma(2 + (1 - \frac{i}{\sqrt{\varepsilon}}))], \tag{D3c}$$

respectively.

With $z = (1 - \frac{i}{\sqrt{\varepsilon}})$ and referring to Eqs. (D2) and (D3), we get the Coulomb phase difference between *p*- and *d*-waves

$$\begin{aligned}\eta_p - \eta_d &= -\arg(z+1) \\ &= -\arg(2 - \frac{i}{\sqrt{\varepsilon}}) \\ &= \arctan\left(\frac{1}{2\sqrt{\varepsilon}}\right)\end{aligned} \tag{D4}$$

Similarly, from

$$\Gamma(z+1)=z\Gamma(z),$$

we have the relation

$$\arg\Gamma(z+1)=\arg(z)+\arg\Gamma(z),$$

or equivalently

$$\arg\Gamma(z+1)-\arg\Gamma(z)=\arg(z). \tag{D5}$$

Adding Eq. (D5) to Eq. (D3) and Eq. (D4), we have

$$\arg\Gamma(z+2)- \arg\Gamma(z)=\arg(z+1)+\arg(z), \tag{D6}$$

With $z = (1 - \frac{i}{\sqrt{\varepsilon}})$ and referring to Eq. (D6), we get the Coulomb phase difference between *s*- and *d*-waves

$$\eta_s - \eta_d = \arctan\left(\frac{1}{2\sqrt{\varepsilon}}\right) + \arctan\left(\frac{1}{\sqrt{\varepsilon}}\right) \tag{D7}$$

Appendix E

Derivation of quantum defect phase differences between s-, p- and d- partial waves

The experimental Rb levels can be represented precisely by a modified Ritz formula, which can be written as

$$E_n = E_\infty - \frac{R}{(n^*)^2} \tag{E1}$$

where R is the Rydberg constant (R=109736.6062 for ^{85}Rb), and n^* is the effective quantum number. The quantum defect δ can be expressed as

$$\delta = n - n^* = a + \frac{b}{(n-a)^2} + \frac{c}{(n-a)^4} + \ldots \tag{E2}$$

Note that a is the asymptotic quantum defect as n goes to infinity.

Eq. (E1) can be rewritten as

$$\frac{1}{(n^*)^2} = -\frac{E_n - E_\infty}{R} = -\varepsilon \tag{E3}$$

where ε is the energy of the electrons in Rydbergs. In the bound state levels, $\varepsilon < 0$; in the continuum states, $\varepsilon > 0$.

For large n, in Eq. (E2), $n - n^* = a$ or $n^* = n - a$, then using Eq. (E3) we have

$$\delta = a - b\varepsilon + c\varepsilon^2$$

The phase shift $\phi = \delta\pi$ [1], we finally obtain

$$\phi = (a - b\varepsilon + c\varepsilon^2)\pi \tag{E4}$$

We list some values of a, b and c in Table B. We choose the data with the smallest uncertainties, which are shaded. With using these data, the quantum defect phase shifts for *s*-, *p*- and *d*-wave can be expressed as follows:

$$\phi_s = (3.131\text{-}0.175\varepsilon\text{+}0.359\varepsilon^2)\pi \quad \text{(E5a)}$$

$$\phi_p = (2.648\text{–}0.359\varepsilon\text{–}4.44\varepsilon^2)\pi \quad \text{(E5b)}$$

and

$$\phi_d = (1.347\text{+}0.599\varepsilon\text{–}1.39\varepsilon^2)\pi \quad \text{(E5c)}$$

Table E.1: Quantum defect parameters a, b and c

n	$n^2S_{1/2}$			n	$n^2D_{3/2,\,5/2}$			References
	a	b	c		a	b	c	
	3.131	0.175	0.359					(2)
9~116	3.131	0.189	-0.578	7~124	1.347	-0.599	-1.39	(3)
15~116	3.131	0.174	-----	15~124	1.347	-0.626	-----	,,
5~116	3.131	0.177	0.175	4~124	1.347	-0.598	-1.410	,,
	3.131	0.204	-1.8					(4)
	$n^2P_{1/2}$				$n^2P_{3/2}$			
	a	b	c		a	b	c	
	2.655	0.388	-7.904		2.641	0.329	-0.975	(5)

References:

1. A. Burgess and M. J. Seaton, Royal Astronomical Society, **120**, 121(1960).
2. Craig J. Sansonetti and K.-H. Weber, J. Opt. Soc. Am. **B 2**, 1385(1985).
3. B. P. Stoicheff and E. Weinberger, Can. J. Phys. **57**, 2143(1979).
4. S. A. Lee, J. Helmcke, J. L. Hall, and B. P. Stoichff, Optics Lett. **3**, 142(1978).
5. C.J. Lorenzen and K. Niemax, Phisica Scripta **27**, 300(1983).

VITA

VITA

Zheng-Min Wang (汪正民) received his undergraduate education at Nanjing University (南京大学), China, in the 1960s. After graduation, he was assigned by the Ministry of Education to join the faculty of the University of Science and Technology of China (USTC--中国科学技术大学), where he served for three years as an assistant instructor and set up a semiconductor materials teaching lab. In those years there was no opportunity to do research at USTC. He started his research career in 1971 at the Anhui Institute of Optics and Fine Mechanics, the Chinese Academy of Sciences (中国科学院安徽光机所). His research activities were related to lasers and applications in various areas, including laser range finders, laser holography, laser spectroscopy and multiphoton dissociation of molecules. In 1988, he came to the USA as a visiting scientist at Ames Laboratory, Ames, Iowa, where he did research for three years on the application of high-resolution optical spectroscopy to the study of high temperature metallic vapors.

After the founding of P.R. China in 1949, there was no degree system established until 1979. He and all the other scientists who received a higher education during that period do not have graduate degrees or even bachelor's degrees unless they earned degrees in later years. He was so happy when he got an opportunity to pursue his advanced study in the United States. He received his M.S. degree in physics at New Mexico State University in the spring of 1994. Now he is working toward his Ph.D. degree in physics at Purdue University. He expresses his deepest appreciation to the Admissions Committee of the Physics

Department for accepting him as a Ph.D. graduate student without age discrimination. He did not let the committee members down: he did well in all aspects of the graduate program. If he had not, he would have owed an apology to the Committee. At the first gate of his years at the Purdue Graduate School -- the Qualifying Exam -- at the beginning of his first semester, he was lucky to receive the highest score among thirty graduate students. There were two reasons for him to return to school after having left school for many years. First, he is passionately interested in science, and enjoys study and doing research. "Never too old to learn" is his motto. The second reason is that he wanted equally passionately to have a Ph.D. degree from a US university. The recent several years have been the most exciting of his career. He has learned a great deal from course work, Ph.D. thesis research, and conferences. He also learned that at US research universities, significant results are expected from graduate research.